DEVELOPMENT OF FINITE ELEMENT MODELING FRAMEWORK TO INVESTIGATE CARDIAC HYPERTROPHY IN HEART DISEASES

By

Joy Mojumder

A DISSERTATION

Submitted to
Michigan State University
in partial fulfillment of the requirements
for the degree of

Mechanical Engineering – Doctor of Philosophy

ABSTRACT

Heart is a prime organ in the human body, and continuously adapting and evolving through growth and remodeling processes to maintain a balance between the demand and supply of blood and oxygen during physiological/developmental (i.e., from birth to adult) and pathological (i.e., various heart diseases) conditions. The exact mechanism of the progression of disease and the growth and remodeling processes are, however, unclear. While numerous experimental studies have been performed on animal models to investigate the mechanism of heart diseases, they are associated with some limitations. To address these limitations, computational frameworks based on idealized, and patient specific heart have been developed. Considering the short history of computational cardiac mechanics compared to experimental studies, many improvements are necessary to advance computational cardiac models. Here we developed both patient and animal specific computational models to investigate the mechanics found in 3 different heart diseases.

First, we developed a computational growth framework based on human biventricular geometry to investigate the growth and remodeling processes associated with mechanical dyssynchrony, a disease caused by the asynchronous contraction of the left ventricle (LV). Cardiac mechanics was described using an active stress formulation and growth model was formulated based on volumetric growth framework. Through prescribing myofiber stretch as growth stimulus, our model can quantitatively reproduce the thickening and thinning of ventricular wall at the late and early activated regions, respectively, for two activation sites, namely, interventricular septum and LV free wall. The model is also able to reproduce global LV dilation found in mechanical dyssynchrony, which is consistent with reported experimental studies.

Second, we developed a computational-experimental approach based on swine model of pressure overload to investigate the correlation between local growth as indexed by changes in

regional thickness and local mechanical quantities. The LV pressure and volume data were acquired from 4 aortic constriction swine models to calibrate the model. From the analysis using the Pearson correlation coefficient, we found a strong correlation between local growth and local myofiber stress induced by an instant rise in peak systolic pressure due to aortic constriction.

Third, we developed a computational framework based on idealized LV model to investigate how pathological features, such as a reduction in global longitudinal strain (GLS), myofiber disarray and hypertrophy, affects LV mechanics in hypertrophic cardiomyopathy (HCM), a genetic heart disease. In this modeling framework, LV mechanics was described using an active stress formulation and myofiber disarray was described using a structural tensor in the constitutive models. Both the LV function indexed by ejection fraction and stroke volume and mechanics indexed by circumferential and longitudinal strain were reduced with increasing myofiber disarray.

Last, we developed patient specific computational models of LV using clinical measurements of 2 female HCM patients based on two different phenotypes (obstructive and non-obstructive) and a control subject. After calibrating our models with clinical data, the results showed that without consideration of myofiber disarray, peak myofiber tension was lowest in the obstructive HCM subject (60kPa), followed by the non-obstructive subject (242kPa) and the control subject (375kPa). With increasing myofiber disarray, peak tension has to increase in the HCM models to match with the clinical measurements. The computational modeling workflow proposed here can be used in future studies with more clinical and experimental data.

Copyright by JOY MOJUMDER 2022 This dissertation is dedicated to my parents and my friend, Dr. Robert N. Coffey Jr. Thank you for always motivating me.

V

TABLE OF CONTENTS

LIST OF ABBREVIATIONS	viii
CHAPTER 1 GENERAL BACKGROUND	1
1.1 Anatomy of heart	2
1.2 Growth and remodeling of heart	
1.3 Review on computational modeling of cardiac hypertrophy	
1.4 Background of this dissertation	
1.5 Objectives of this dissertation.	17
CHAPTER 2 BIVENTRICULAR MODEL ON LEFT BUNDLE BRUNCH BLOCK	19
2.1 Introduction	
2.2 Methods	
2.3 Results & Discussion	
2.4 Conclusion	
CHAPTER 3 ANIMAL SPECIFIC LEFT VENTRICULAR MODEL ON PRESS	
OVERLOAD	
3.1 Introduction	
3.2 Methods	
3.3 Results & Discussion	
5.4 Conclusion	4/
CHAPTER 4 IDEALIZED LEFT VENTRICULAR MODEL ON HYPERTRO	
CARDIOMYOPATHY	
4.1 Introduction	
4.2 Methods	
4.3 Results	
4.4 Discussion	
4.5 Conclusion	68
CHAPTER 5 PATIENT SPECIFIC LEFT VENTRICULAR MODEL	
HYPERTROPHIC CARDIOMYOPATHY	
5.1 Introduction	
5.2 Methods	
5.3 Results	
5.4 Discussion	
5.5 Conclusion	91
CHAPTER 6 LIMITAIONS AND FUTURE SCOPE	
6.1 Biventricular model on Left Bundle Brunch Block	
6.2 Animal specific LV model on pressure overload	
6.3 Idealized LV model on Hypertrophic Cardiomyopathy	
6.4 Patient specific LV model on Hypertrophic Cardiomyopathy	
6.5 Conclusion	95

BIBLIOGRAPHY	96
APPENDIX A: MODEL PARAMETERS WITHOUT DISARRAY	113
APPENDIX B: MODEL PARAMETERS WITH DISARRAY	115

LIST OF ABBREVIATIONS

Cardiac magnetic resonance imaging, CMR

Cardiac resynchronization therapy, CRT

Ejection fraction, EF

End-diastolic volume, EDV

Endothelin-1, ET-1

End-systolic volume, ESV

Extracellular volume, ECV

Finite element, FE

Fractional anisotropy, FA

Global longitudinal strain, GLS

Growth and remodeling, G&R

Hypertrophic cardiomyopathy, HCM

Induced pluripotent stem cells, iPSC

Late gadolinium enhancement, LGE

Left atrium, LA

Left bundle brunch block, LBBB

Left ventricle, LV

Left ventricular assist device, LVAD

Left ventricular free wall, LVFW

Left ventricular outflow tract, LVOT

Magnetic resonance imaging, MR

Mechanical dyssynchrony, MD

Non-sustained ventricular tachycardia, NSVT

Right atrium, RA

Right ventricle, RV

Right ventricular free wall, RVFW

Root mean square error, RMSE

Sudden cardiac death, SCD

Three dimensional, 3D

CHAPTER 1 GENERAL BACKGROUND

1.1 Anatomy of heart

The heart is a critical component of the cardiovascular system, which ensures that adequate blood flow is delivered to the body organs to facilitate the exchange of gases, fluid, electrolytes, large molecules and heat between the cells and outside environment [1]. The heart consists of four chambers, namely, the left atrium (LA), left ventricle (LV), right atrium (RA) and right ventricle (RV) (**Fig 1.1**). At the tissue level, the heart wall consists of myofibers that are oriented helically

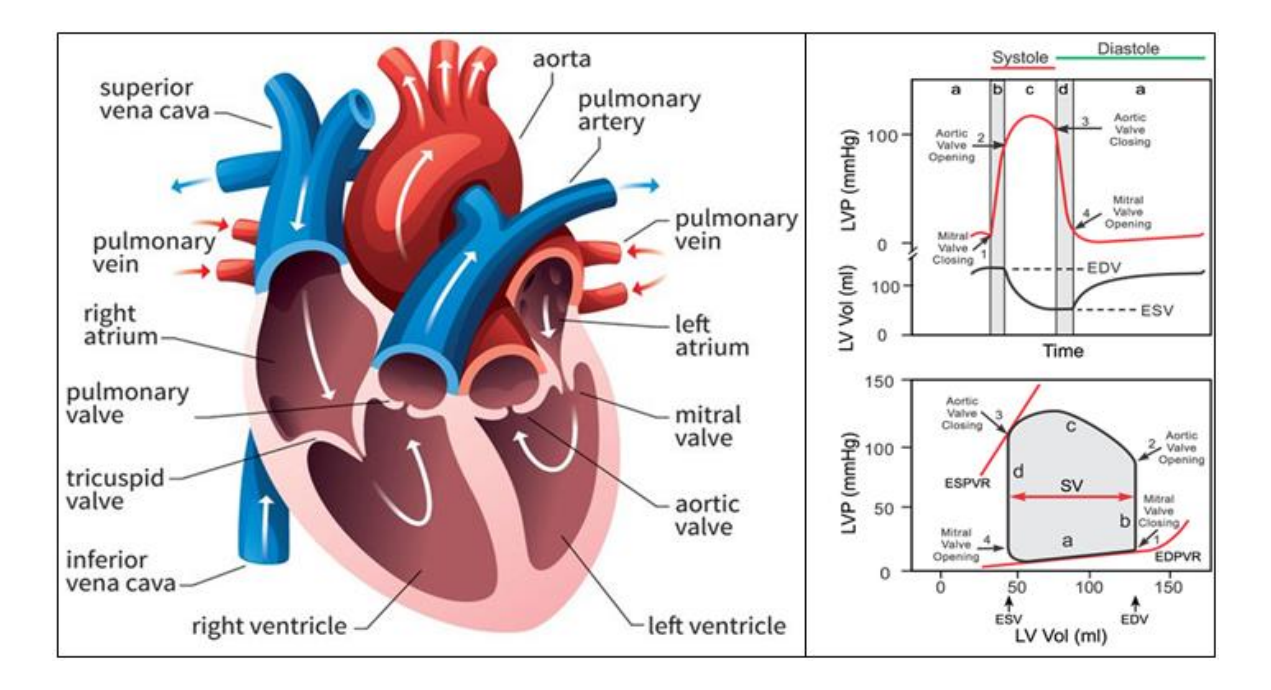


Figure 1.1: Basic anatomy of heart (left). Pressure-volume relationship in LV during a cardiac cycle (right). During systole, isovolumic contraction (b) and ejection (c) occurs, while during diastole, isovolumic relaxation (d) and ventricular filling (a) occurs. The figures are adapted from internet.

with their orientation varying transmurally from the endocardium (inner periphery of the heart) to the epicardium (outer periphery of the heart). When operating *in vivo*, the heart undergoes a sequence of mechanical events that are associated with different phases in the cardiac cycle. Specifically, the cardiac cycle is divided into 2 general phases, namely systole and diastole. The systole phase refers to events associated with ventricular contraction and ejection, whereas the diastole phase refers to the rest of cycle that includes ventricular relaxation and filling (**Figure**)

1.1). The heart cyclically contracts over a cardiac cycle to generate a pressure gradient to perfuse all body organs including itself. At a smaller tissue scale on the other hand, the myocardium in the heart wall operates as a system where its function depends on the highly complex and tightly orchestrated collective interactions between cells and sub-constituents [2].

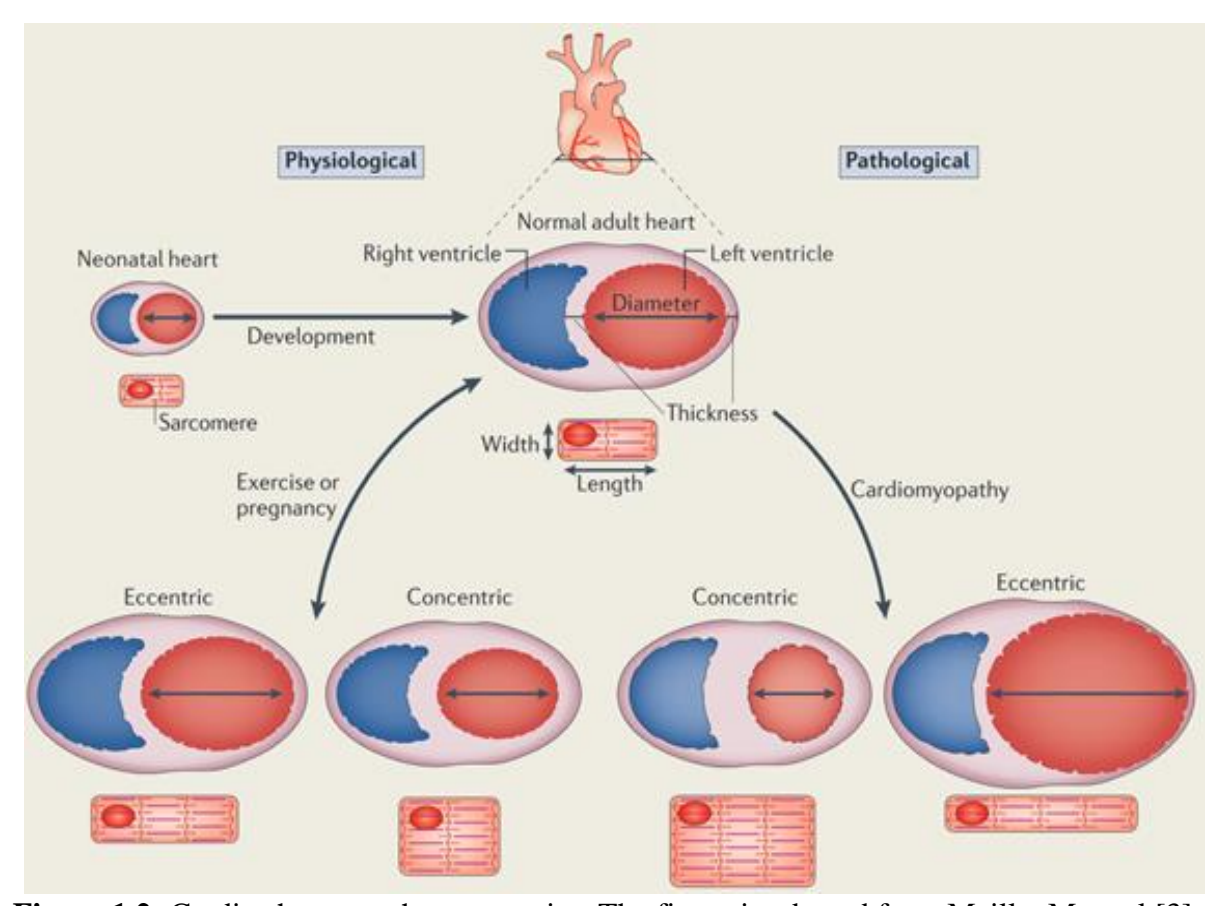


Figure 1.2: Cardiac hypertrophy geometries. The figure is adapted from Maillet M. et al [3].

1.2 Growth and remodeling of heart

In response to electrical, mechanical, chemical and neurohormonal cues, the myocardium can also undergo long term adaptive (i.e., favoring myocyte survival) or maladaptive (i.e., promoting apoptosis) processes that are commonly referred to as "growth and remodeling" (G&R). These processes can lead to geometrical and functional changes of the heart. As shown in **Figure**1.2, the nature of G&R can be pathological (e.g., in heart diseases) or physiological (e.g., during

growth and development, exercise, pregnancy, aging) [3]. Growth and remodeling of the heart can be broadly classified into two types, namely, eccentric hypertrophy and concentric hypertrophy.

In eccentric hypertrophy, the LV wall becomes thinner via serial sarcomerogenesis (i.e., addition of sarcomere) with significant increase in the chamber volume. In concentric hypertrophy, the LV wall thickens via parallel sarcomerogenesis with little or no change in the cavity volume [4–6]. Pathological conditions such as hypertension, aortic stenosis and mitral regurgitation are associated with concentric, eccentric or a mixture of both types of hypertrophy. Besides geometrical changes, hypertrophy also produce changes to the local mechanical quantities of the LV, specifically, myocardial wall stresses and stretches [7]. It is believed that a change in tissue mechanics is one of the major driving forces of growth at both the cellular and organ levels [8]. Based on in vivo studies at the organ level, volume overload increases the passive stretches or stresses of the muscle cells during ventricular filling in diastole that is associated with the chronic dilation of the heart chamber [9], whereas, an increase in afterload in pressure overload not only produces an increase in stresses of the muscle cells during systole [10–12], but it may also affect the stretches of the cells that are associated with chronic ventricular wall thickening. According to the systolic stress-correction hypothesis proposed by Grossman et al. [13], the increase in wall thickness in concentric hypertrophy helps normalize wall stress to the baseline homeostatic levels.

Besides sarcomerogenesis, ventricular remodeling are also associated with cardiac fibrosis, which is characterized by the net accumulation of extracellular matrix in the myocardium [6, 14–16]. Remodeling associated with progressive fibrosis can lead to the development of diastolic heart failure in elderly patients. On the other hand, during pressure overload, extensive cardiac fibrosis is associated with ventricular dilation and combined diastolic and systolic heart failure. Cardiac fibrosis, during volume overload, characterized by disproportionately large

amounts of non-collagenous matrix, may lead to chamber dilation and the development of systolic dysfunction.

In addition to sarcomerogenesis and fibrosis, myofiber disarray (e.g., in hypertrophic cardiomyopathy, (HCM) [17]), loss of myocyte function (e.g., contractile dysfunction in pressure overload and HCM [18, 19]), alteration of molecular pathways and genetic mutations [20] are also observed during cardiac remodeling. A reversal of remodeling may also occur in some heart failure treatments (e.g., left ventricular assist device (LVAD), cardiac resynchronization therapy (CRT) [21]), which is widely considered to be a sign of recovery for the patient. Overall, cardiac G&R has very significant clinical implications and is widely considered to be an important determinant of the clinical course of heart failure.

1.3 Review on computational modeling of cardiac hypertrophy

Despite the clinical significance of cardiac G&R, the exact mechanisms of myocardial G&R are, however, not known [22]. For example, the type of mechanical cues that myocytes sense and the way they respond to those mechanical cues have not been fully elucidated. An in-depth understanding of the various mechanisms of G&R can provide key insights to develop effective heart failure therapies. Given the complexity of the multitude of G&R pathways and their interactions, computational modeling integrated with experiments have been extensively used to predict and understand pathological and physiological behaviors of the heart across multiple scales [22–26]. Several computational modeling frameworks have been developed to predict long-term changes associated with cardiac G&R [25]. Specifically, cardiac growth constitutive models have been formulated based on the volumetric growth framework in which the deformation gradient tensor is multiplicatively decomposed into an elastic and a growth component to describe local changes in shape and size of the myocytes in response to local alterations of cardiac mechanics

(i.e., stresses) and/or kinematics (i.e., strains) [27, 28]. These constitutive models are usually coupled with a computational cardiac mechanics model to simulate how geometrical changes of the myocytes collectively affect ventricular geometry when the loading conditions are altered [22, 29–31]. For example, Goktepe et al. [30, 32] and Rausch et al. [33] both proposed a stress-driven growth constitutive model to describe ventricular wall thickening associated with pressure overload in the heart. On the other hand, Kerckhoffs et al. proposed a unified strain-driven growth law that is able to reproduce features found in concentric hypertrophy associated with aortic stenosis and eccentric hypertrophy associated with mitral valve regurgitation [31]. Based on this unified strain driven growth law but with different homeostatic set points for growth, Yoshida et al. showed that the model is able to predict forward growth with pressure overload, but is unable to predict reverse growth with the removal of pressure overload [34]. While these phenomenological G&R models can capture the global features and/or some features of either pressure overload or volume overloaded heart [23], there are still questions to be answered and issues to be tackled with computational modeling of cardiac growth. Also, since most of these models are based on idealized LV ellipsoidal geometry, they cannot be applied directly to individual patients because the outcome is a rough estimate and based on averages [35]. Hence, it is necessary to develop a patient-specific modeling framework to tailor treatment and optimize an individual's therapy.

1.4 Background of this dissertation

1.4.1 Mechanical dyssynchrony

Left ventricular mechanical dyssynchrony (MD) is a disease associated with mechanical contraction or relaxation occurring asynchronously between different segments of the LV. During a cardiac cycle, MD can affect the systolic phase by decreasing the efficiency of contraction and

the diastolic phase by decreasing the efficiency of LV filling. It can also affect both systolic and diastolic phases. Besides being associated with alteration of the acute electro-mechanical behaviors such as a prolonged QRS duration, a reduction in wall motion and changes in blood flow etc. [36], MD can also lead to long-term ventricular remodeling [37]. Sometimes MD and electrical dyssynchrony (defined by the inhomogenous LV activation of activation delay between ventricles [38]) are both found in patients with left bundle branch block (LBBB). Patients with LBBB have showed an increased risk of developing cardiac diseases such as hypertension, congestive heart failure [39]. The mortality rate is also higher in these patients with MD if not treated [39–41].

Several experimental studies have been performed on animal models to investigate the effects of asynchronous electrical activation and contraction pattern in the ventricles induced by ventricular pacing at different sites of the LV. The activation timing and pacing locations in these animal models altered the ventricular mechanics and pump function of the heart. More specifically, ventricular pacing at different locations of the canine heart (i.e., the RA, the LV free wall, the LV apex or the RV outflow tract) resulted in a reduction of myofiber shortening, contractile work, myocardial blood flow, and oxygen consumption in early activated region. These quantities, however, are increased in the late activated region [36, 42]. Besides these acute changes, ventricular enlargement (represented by increased LV cavity volume), increased wall mass and asymmetrical LV wall hypertrophy were found with long term asynchronous electrical activation [43, 44]. The asymmetrical LV wall hypertrophy is associated with the thickening and thinning of the late- and early- activated regions, respectively.

While all these experimental studies have contributed to our understanding on the alteration of LV mechanics with MD, it is difficult to determine the possible mechanism(s) of hypertrophy associated with mechanical cues solely from these experiments. Hence, it is necessary to develop

a mathematical framework describing the G&R associated with MD to increase our understanding of its mechanism. To address this limitation, we developed a finite element framework seeking the stimuli associated with chronic G&R in MD, as described in **Chapter 2**.

1.4.2 Pressure overload

Ventricular afterload is an important determinant of cardiac function and chronic G&R under physiological and pathological conditions. Afterload is often indexed by the pressure of the LV during ejection e.g. peak LV pressure or end systolic pressure. Based on Laplace's law,

$$\sigma = \frac{PR}{2t} \tag{1.1}$$

an increase in afterload contributes to an increase in total wall stress [45]. In the above equation, σ , P, R and t denote the ventricular wall stress, end systolic pressure, end-systolic radius and wall thickness, respectively. An increase in afterload is associated with an increase in left ventricular output impedance and consequently, is associated with an increase in ventricular pressure during systole as seen in various pathological conditions such as aortic stenosis, hypertension, increased total peripheral resistance, HCM etc. [45, 46]. An increase in LV systolic pressure develops higher wall stress, which leads to ventricular remodeling where wall thickness is increased (initially) as a compensatory mechanism. Pressure overload hypertrophy occurs as a result. Additionally, coronary blood blow may be affected when a new balance between oxygen supply and the increased demand is reached with the increase in wall tension [45].

An increase in afterload can lead to the development of heart failure [47] (see a brief review on G&R induced by pressure overload in **section 1.2**). The progression of hypertrophy in heart diseases associated with pressure overload is still under investigation. Several surgical techniques performed on animal models have been developed to mimic the nature of mechanical cues related to pressure overload and investigate how the cells and heart response to these cues over a long

period time [48]. For example, animal models of ascending or transverse aortic constriction mimic aortic stenosis while abdominal aortic constriction or renal warping mimic cues related to hypertension [47]. One of the most frequently used surgical technique to induce pressure overload is ascending aortic constriction (AAC), where a stricture is placed around ascending aorta. Another common model is transverse aortic constriction (TAC) associated with constricting the aorta between the brachiocephalic trunk and the left common carotid artery. These surgical models have both advantages and disadvantages. For example, while the quantification of pressure gradient across the aortic stenosis and stratification of LV hypertrophy are easier with TAC, the higher mortality rate in rats at early state of TAC due to acute cardiac insufficiency makes the application of this technique limited to certain types of animals [49]. On the other hand, AAC is less complicated and time-consuming. It also has high intra- and inter-surgeon reproducibility, low postoperative mortality and reproducible HF phenotypes [50]. The progression and frequency of development of HF induced by these surgical models depend on various factors including banding severity, location, rodent strain, animal type and time course etc. Overall, the consideration of advantages and disadvantages of an animal model along with the purpose and method of experiment will play vital role on the success of these surgical experiments.

While animal models are widely being used to recreate the features associated with pressure overload, the intrinsic mechanism of the disease progression associated with pressure overloaded can be investigated by computational modeling. Computational models have been widely used to investigate change in those mechanical properties such as stress or perfusion, which are not easy to measure experimentally or clinically in the deep layer of the myocardium. Also, several computational models have been developed to investigate G&R due to pressure overload. A brief review of existing models is given in section 1.3 and 3.1. However, to our best knowledge,

the change in LV mechanics due to the change in instant pressure induced by experimental condition have not been investigated yet. To address this limitation, we develop animal specific model to investigate the mechanics and how its changes is correlated to growth during pressure overload in **Chapter 3**.

1.4.3 Hypertrophic cardiomyopathy

HCM is a genetic heart disease resulting from sarcomeric protein mutations in 60% of patients [51–57]. It has a prevalence of 1 per 500 and a mortality rate that is 4-fold higher in young adults than the general US population [58–63]. This disease is associated with sudden cardiac death (SCD). The annual incidence due to SCD is approximately 1% and far higher in asymptomatic young adults and pediatric patients, respectively [64–66]. Clinical risk factors of SCD include a family history of SCD, unexplained syncope, non-sustained ventricular tachycardia (NSVT), maximum left ventricular wall thickness, and an abnormal blood pressure response during exercise [67]. In symptomatic HCM patients, typical symptoms include dyspnea, chest pain, exercise intolerance, palpitations, and syncope [57]. Treatments widely vary in HCM patients depending on the severity of symptoms and risk factors. Most treatments (e.g., septal myectomy and pharmacological treatments) of HCM are designed to alleviate symptoms and decrease the risk of SCD [68]. Recently, the drug Mavacamtem has showed promising results as a treatment for HCM patients [69–71], especially in obstructive HCM patients where it showed an attenuation in cardiac remodeling [70]. The scope of Mavacamtem on non-obstructive hypertrophy, however, is still under investigation [72].

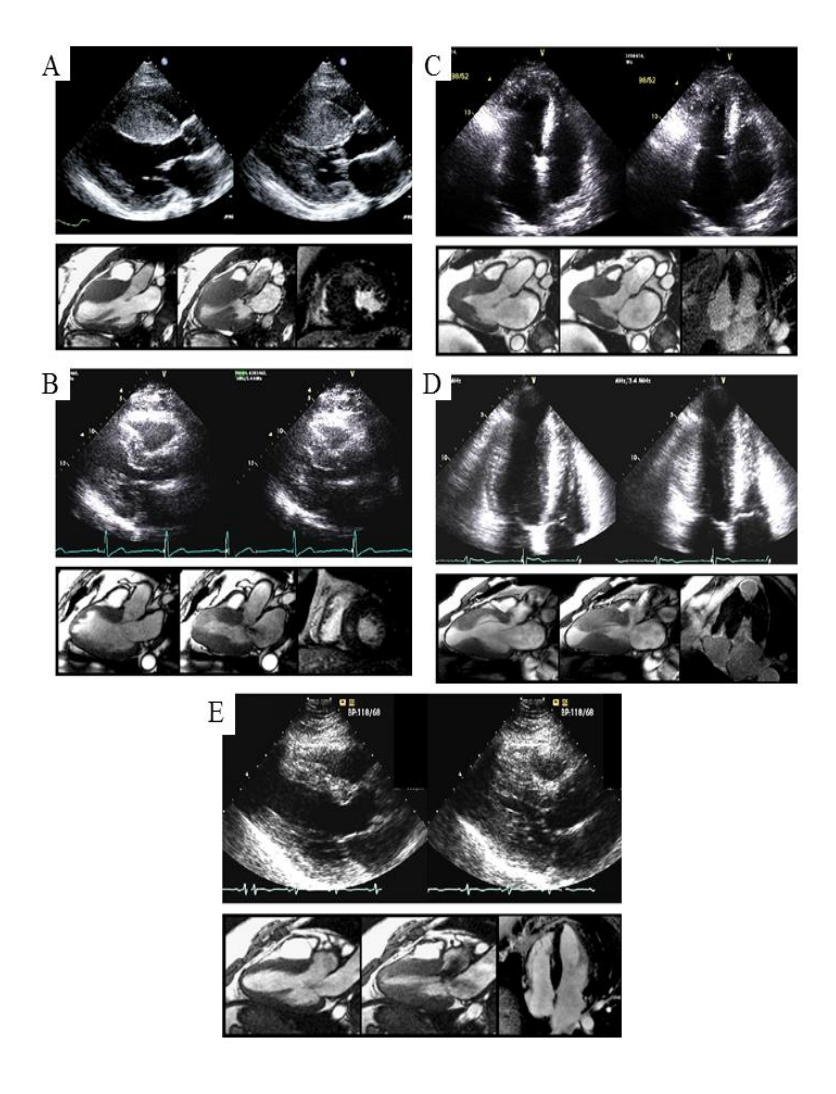


Figure 1.3: Morphologic subtypes of HCM demonstrated by echocardiography and magnetic resonance imaging. A)Reverse curvature, B)Sigmoid septum, C)Apical HCM, D)Midventricular septum and E)Neutral septum. In each subtype, end diastolic (left) and end-systolic (right) echocardiography images of heart are shown at upper images. In lower images of each subtype, left and middle columns show heart in a 3-chamber orientation in end-diastole and end-systole, respectively, whereas, right column shows myocardial delayed enhancement (MDE) images. This image is adapted from Syed et al. [73].

There are several phenotypes of HCM with different features. Two of the most widely considered phenotypes of this disease are, namely, non-obstructive HCM (30 %) and obstructive HCM (70 %). These 2 phenotypes of HCM are distinguished based on whether left ventricular outflow tract (LVOT) obstruction, as defined by a maximal left ventricular gradient greater than or equal to 30 mm Hg at rest or with provocation, is present [74–76]. In addition, HCM can also

be classified based on the variation of hypertrophy distribution that can be generalized into four types. Type I HCM is associated with hypertrophy at the basal septum, type II HCM is associated with hypertrophy involving the whole septum, type III HCM is associated with hypertrophy involving the septum, anterior, and anterolateral walls and type IV HCM is associated with LV apical hypertrophy [77]. In addition to these 4 types of HCM, five major anatomic subsets have been suggested based on the extent of hypertrophy and septal contour, namely, reverse septum curvature, sigmoidal septum, apical form, mid-ventricular form, and neutral contour (**Figure 1.3**) [73]. Three functional phenotypes of HCM, namely sub-aortic obstruction, mid-ventricular obstruction and cavity obliteration, were also suggested [78].

Several techniques have been developed to diagnose HCM. Among these techniques, echocardiography has played a vital role in the diagnosis and monitoring of HCM patients. In echocardiography, it is recommended to measure the thickness of LV segments from base to apex for all patients. Additional assessment of the apical segments are required to measure the hypertrophy at the LV apex in patients with apical hypertrophy [79]. The use of contrast agents for optimal LV opacification or better imaging techniques such as cardiac magnetic resonance imaging (CMR) is also preferred to adequately visualize the LV segment.

At the tissue and organ level, HCM is characterized by myofiber disarray [17, 80–83], disorganized myocardial architecture [84–89], abnormal septal hypertrophy compared to the left ventricular free wall (LVFW), changes in the myocardial contractility, and interstitial and replacement fibrosis [81–89]. These features have been associated with changes in the LV function seen in HCM patients, such as a reduction in (global and segmental) longitudinal and circumferential strains [63, 90–92], an increase in relative ATP consumption during tension generation [93], and a reduction in myocardial work [94]. Additionally, microvascular

dysfunction, diffused myocardial ischemia and myocardial cell death are also reported in HCM patients [95].

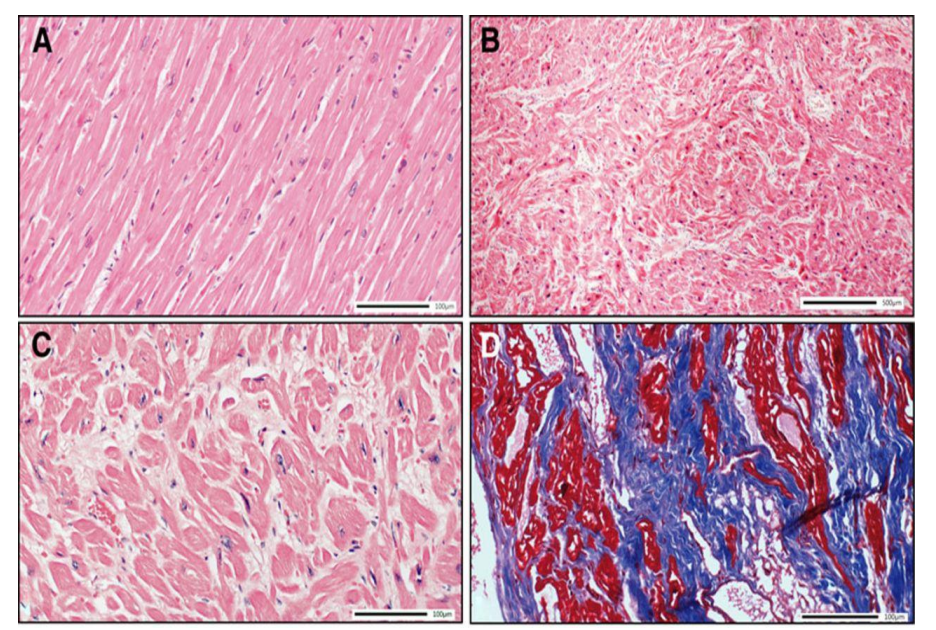


Figure 1.4: Histological phenotypes of HCM. A thin myocardial section showing **A**. organized myocardial architecture in normal patient. **B**. disorganized myocardial architecture in HCM patient. **C**. myocyte disarray at higher magnification in HCM patient. **D**. interstitial fibrosis at blue region in a thin myocardial section stained with Masson trichrome. Figure is adapted from Marian et al [96].

Myocardial disarray (**Figure 1.4**) is an archetypal feature of HCM. This pathological feature is independent of LV wall thickness and may be present in both normal and hypertrophied regions [97]. Although it does not exhibit significant variations between the various regions in the heart of HCM patients, myofiber disarray appears slightly more frequently in the interventricular septum [96]. The exact stimuli inducing myofiber disarray in HCM heart is still unknown. In an *in vitro* study, using induced pluripotent stem cells (iPSCs)-derived cardiomyocytes, a group of researchers found that Endothelin (ET)-1 peptide enhanced the incidence of myofibrillar disarray in the HCM iPSC-derived cardiomyocytes. Using mouse HCM model, they also confirmed that myofibrillar disarray was induced by ET-1 [98]. However, due to the differences in nature between adult cardiomyocytes and iPSC-derived cardiomyocytes, the underlying mechanism causing

myofiber disarray is still under investigation. While the genetic backgrounds causing myofiber disarray in HCM heart is still under investigation, with the advancement of imaging techniques such as Diffusion Tensor – CMR, *in vivo* visualization of normal and HCM myocardial structure have provided substantial insights on myofiber disarray (shown in **Figure 1.5**) in HCM patients. Along with these techniques is the introduction of a new marker, fractional anisotropy, to describe the degree of myofiber disarray in the cardiac wall quantitatively [17].

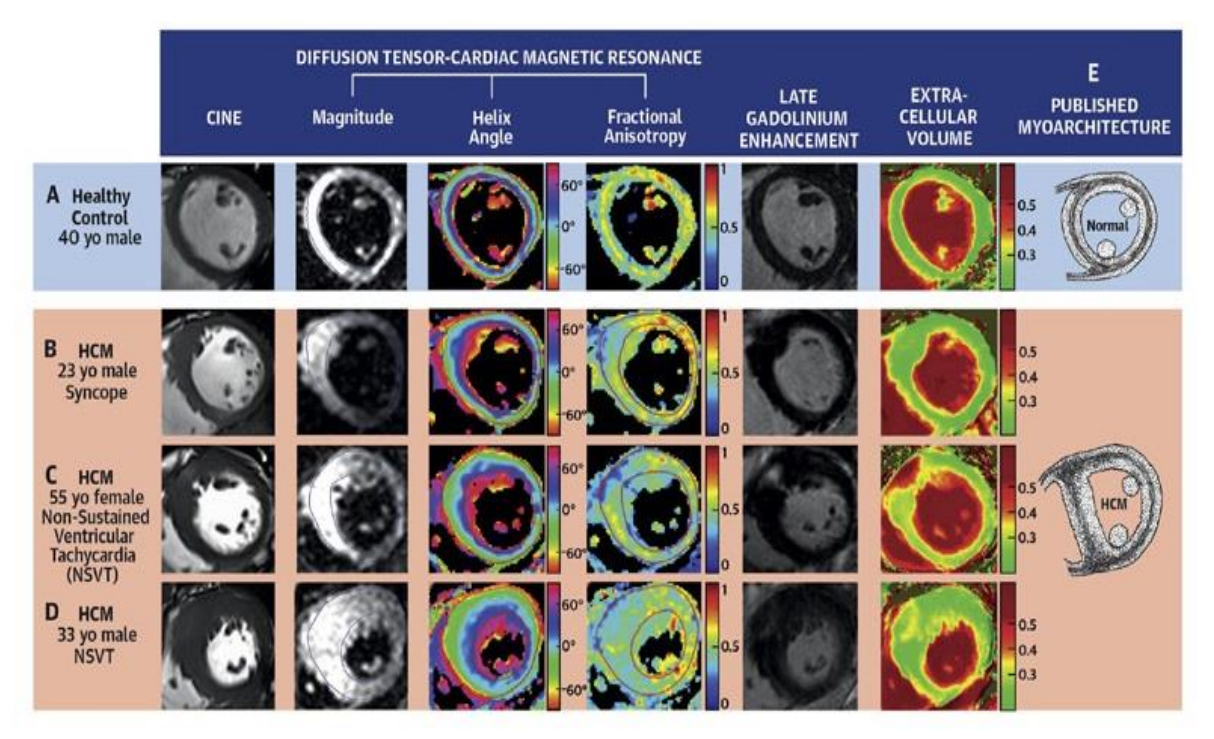


Figure 1.5: Disarray and fibrosis depicted by Fractional anisotropy and late gadolinium enhancement, respectively, using diffusion tensor-CMR in HCM and control patients. This figure is adapted from Ariga et al [99].

Table 1.1: Clinical data of circumferential strain (%)

LV Segment	Young et al 1993[100]		Sun et al 2009[91]		Piella et al 2010[92]	
	Normal	HCM	Normal	HCM	Normal	HCM
Septal	19.67±2.67	15±5.67	23.97±5.47	16.17±7.17	14.28±1.58	9.38±3.24
Lateral	21.3±2.33	19.67±4	16.87±5.89	15.77±6.63	13.4±1.54	9.86±3.32
Inferior	-	-	20.67±6.5	17.5±5.57	13.73±2.07	8.6±2.63

Table 1.1 (cont'd)

Anterior	21.67±2.33	18.67±6	20.23±5.2	15.47±7.6	12.5±1	8.63±3.32
Posterior	19.67±3	17.3±4.67	17.1±6.2	17.7±6.43	-	-
Anterior septal	-	-	23.7±5.03	15.9±8.2	-	-

Table 1.2: Clinical data of longitudinal strain (%)

LV Segment	Young et al 1993[100]			
	Normal	HCM		
Septal	16±2.33	9.67±6.3		
Lateral	17.67±3.33	12.3±5		
Inferior	-	-		
Anterior	16.67±2.33	10.67±5		
Posterior	17.67±3.33	10.3±5.67		
Anterior septal	-	-		

Reduction in global longitudinal strain (GLS) is a feature of HCM at early stages and before the development of hypertrophy in relatives of HCM patients [101, 102]. GLS is not only a sensitive indicator of global left ventricular function, but is also a prognostic marker to predict mortality and cardiac events in other cardiac diseases [103–106]. A significant association between worse LV-GLS and increased composite cardiac outcomes has been showed in a systematic review over the prognostic value of GLS in HCM. Based on a 3-year follow-up period, patients with GLS > -16% had a significantly high risk for sustained ventricular tachycardia/fibrillation, heart failure, cardiac transplantation, and all-cause death compared to patients with GLS < -16% [90, 107]. Patients with GLS > -10% had four times higher risk of events compared to patients with GLS value $\le -16\%$ [107]. Besides global reduction of strain, regional variation of strain has also been found in this disease. Specifically, circumferential strain was reduced significantly (\sim 5%

minimum[92], 7.8% maximum [91]) at septal regions in HCM patients compared to healthy normal humans (**Table-1.1**, **Table-1.2**). Compared to the septal region, the reduction in circumferential strain in the lateral regions (LVFW) was lower (~1% minimum [91], 3.5% maximum [92]). In the study by Sun et al [91], however, they reported a 0.6% increase in circumferential strain at the LV posterior region. On the other hand, the decrease in longitudinal strain was larger in the septum than lateral regions (6.3% vs 5.4% decrease) in HCM patients compared to healthy humans. This heterogeneity in strain distribution could be due to the regional distribution of myocardial disarray and fibrosis. The exact mechanism of how strain is affected by this disease and how it predicts outcome, however, remains unclear.

Hypertrophy of the LV is a key feature of HCM. Specific to this disease, hypertrophy is largely asymmetric with heterogeneous wall thickening [108]. Left ventricular wall thickness is typically analyzed in HCM patients with echocardiography based mostly on the short-axis view images acquired at multiple levels at end diastole [109], [79]. A well-known cut-off value of LV wall thickness for defining hypertrophy in adults, relatives and pediatric patients are \geq 15 mm, >12–15 mm and \geq 2 Standard Deviation greater than the Body-Surface-related normal values, respectively [110, 111]. The presence of asymmetric septal hypertrophy in HCM patients is defined by a septal-to-posterior diastolic wall thickness ratio \geq 1.3 (or \geq 1.5 in hypertensive patients), with or without subaortic obstruction [109].

Myocardial fibrosis is a key feature and a marker to predict mortality rate, SCD and progression toward heart failure in HCM patients [112, 113], [114]. This feature can be evaluated using magnetic resonance imaging with late gadolinium enhancement (LGE). The distribution of fibrosis vary greatly between various regions of the LV wall, including septum, LV free wall, lateral wall, apex, and RV insertion point in HCM patients [115, 116]. Extracellular volume (ECV)

estimated from CMR imaging with LGE has also been found to correlate with the hypertrophied region in HCM patients [117].

About one third of HCM patients with LVOT obstruction have systolic anterior motion of the mitral valve due to severe interventricular septum hypertrophy, mitral leaflet abnormalities, papillary muscle hypertrophy, and displacement. In about one third of these patients, latent LVOT obstruction is provoked due to changes in preload and/or afterload, or altered LV contractility [76].

Motivated by the diverse nature of HCM and lack of computational models on the mechanics of HCM, we have developed two finite element frameworks based on an idealized LV geometry and patient specific geometries to investigate the effects of remodeling features on the altered mechanics of HCM. These models are briefly explained at **Chapter 4 & 5**.

1.5 Objectives of this dissertation

The overall objectives of this dissertation are to develop computational framework to evaluate and describe 1) volumetric changes in the heart wall (hypertrophy/atrophy) in heart diseases and 2) tissue microstructure (myofiber disarray) changes in heart diseases. More specifically, the objectives explained in following chapters are as follows.

Chapter 2: A coupled electromechanics-growth model was developed to simulate the long-term effects during MD. Using myofiber stretch as stimulus, this model can quantitatively reproduce asymmetrical hypertrophy by wall thinning of early activated region and wall thickening of late activated region.

Chapter 3: A computational-experimental approach was developed to identify the mechanical stimuli during pressure overload. The computational framework was calibrated against experimental measurements from 4 aortic constriction porcine models, and the results showed a strong correlation between myofiber stress and growth.

Chapter 4: A computational framework describing the effects of myofiber disarray in the LV of HCM patients was formulated and developed. The computational framework was developed based on an idealized LV geometry and calibrated using published data associated with healthy humans and HCM patients. The effects of geometry and myofiber disarray globally was investigated using the model. The simulated results showed that the mechanics of left ventricle got impaired by varying myofiber disarray.

Chapter 5: A patient specific computational model was developed to investigate the ventricular mechanics associated with obstructive and non-obstructive HCM patients. The model was validated using patient-specific clinical measurements of the HCM patients. The effects of varying degree of myofiber disarray was investigated using the model. Using this model we found that the contractile force generated by the cell to reproduce clinical measurements is increased with an increase in global myofiber disarray.

CHAPTER 2 BIVENTRICULAR MODEL ON LEFT BUNDLE BRUNCH BLOCK

2.1 Introduction

Mechanical dyssynchrony [36, 39–41] is a disease associated with asynchronous contraction or relaxation of the RV and LV[118]. Experimental studies using animal models have shown that ventricular pacing produces ventricular dilation and asymmetrical hypertrophy [43, 44]. While existing computational cardiac growth models mentioned earlier (in **Section 1.3**) have largely focused on describing pathologies associated with the global alterations in loading conditions, such as pressure and volume overload that produce concentric and eccentric hypertrophy, respectively [30, 31, 119, 120], little work has been done to simulate long-term changes associated with alterations of the electrical conduction pattern in the heart except for study [121].

In order to simulate chronic changes associated with MD, it is necessary to prescribe the appropriate stimulus driving G&R. While the exact stimulus driving growth is still unknown, insights provided by an experimental study on cardiomyocyte growth suggest that longitudinal stretch can produce both longitudinal and transverse growth by series and parallel addition of sarcomeres, respectively [122]. Motivated by these experimental observations, we seek here to investigate,

- i) if prescribing myofiber stretch as a single stimulus that controls growth in the myofiber and transverse directions (with different sensitivity) can quantitatively reproduce long term changes in ventricular geometry associated with MD
- ii) if it is possible to find different forward and reverse growth rates in the longitudinal and transverse directions that can simultaneously and quantitatively reproduce global and local asymmetrical changes in biventricular geometry.

2.2 Methods

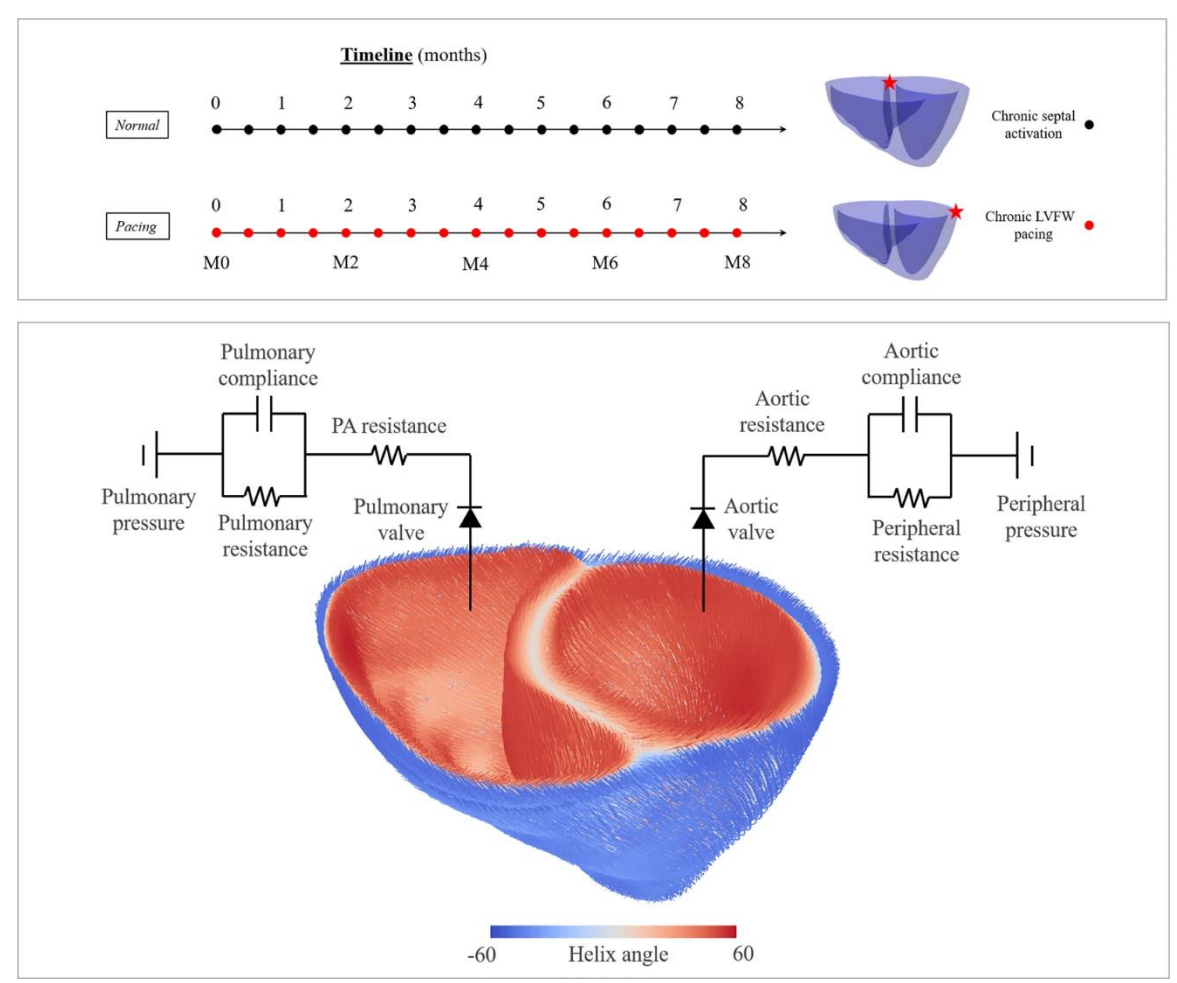


Figure 2.1: Top: Simulated chronic pacing timelines are shown. Pacing locations are indicated in the geometry using a red star. Bottom: Myofiber architecture and lumped circulation model.

On the basis of single-cell experiments [122] and an existing computational modeling framework [29, 123], we developed an anisotropic G&R constitutive model in which the changes in lengths of the tissue in 3 orthogonal material directions are driven locally by the deviation of maximum elastic myofiber stretch (over a cardiac cycle) from its corresponding homeostatic set point value. This model was coupled to an electromechanics modeling framework [21, 124–127] to simulate the long-term effects of asynchronous activation associated with LVFW pacing (**Figure 2.1**). After appropriate calibration of parameters, the model predictions were compared with local

and global measurements in canine experiments with similar chronic LVFW pacing protocol, as shown in **Table 2.1**.

Table 2.1: Comparison with experimental data (adapted from [128])

Parameter	Month	LVFW pacing simulation	LVFW Pacing Experiment [129]	LBBB Experiment	LVFW Pacing Experiment [44]
LVEDV (%	0	100	100 ± 27.8	100 ± 29.8	100
of Normal)	2	102.3		117.5 ± 12.8	_
	4	104.6	_	129.8 ± 50.9^{R}	_
	6	109	107.4 ± 29.9^{M}	<u> </u>	_
	8	113.7		_	_
LVEF (%)	0	48.7	35.3 ± 7.0	43 ± 4.0	100
2,51 (,0)	2	48.3			_
	4	48.6	_	33 ± 6^{R}	_
	6	47.8	39.6 ± 8.9^{M}	_	_
	8	48.3	_	_	_
LVESV (%	0	100	100	_	100
Change)	2	104.9	_	_	_
	4	108.7	_	_	_
	6	118.5	_	_	_
	8	126.4	_	_	_
Early	0	100^L	100^L	100 ^C	100^L
activated	2	90.3 ^L	90.7 ± 8.7^{L}	_	$88.9 \pm 6.8^{L,R}$
region	4	83.9 ^L	87.0 ± 7.2^{L}	_	$79.7 \pm 8.0^{L,R,*}$
thickness	6	81.3 ^L	$86.5 \pm 16.7^{L,R}$	_	_
(% change)	8	79.6 ^L	_	_	_
Late	0	100^{C}	100^{C}	100^L	100 ^c
activated	2	105.2 ^c	108.4 ± 11.3^{C}	_	96.8 ^{C,M}
region	4	113.7 ^c	110.5 ± 16.8^{C}	_	$103.0 \pm 7.5^{C,M,*}$
thickness	6	119.6 ^c	$122.5 \pm 11.3^{C,R}$	_	_
(% change)	8	127.5 ^{<i>c</i>}	_	_	_
RV	0	100	100	100	100
thickness	2	91.4			
(%	4	91.1	_	_	_
Change)	6	88.6	_	_	_
M 1	8	88.7			_

 $^{^{}M}$ denotes no significant change over time; R denotes significant change over time (p<0.05)

^L denotes LVFW thickness; ^C denotes septum thickness

^{*} denotes 3 months; — denotes not reported or measured

2.2.1 Growth constitutive model

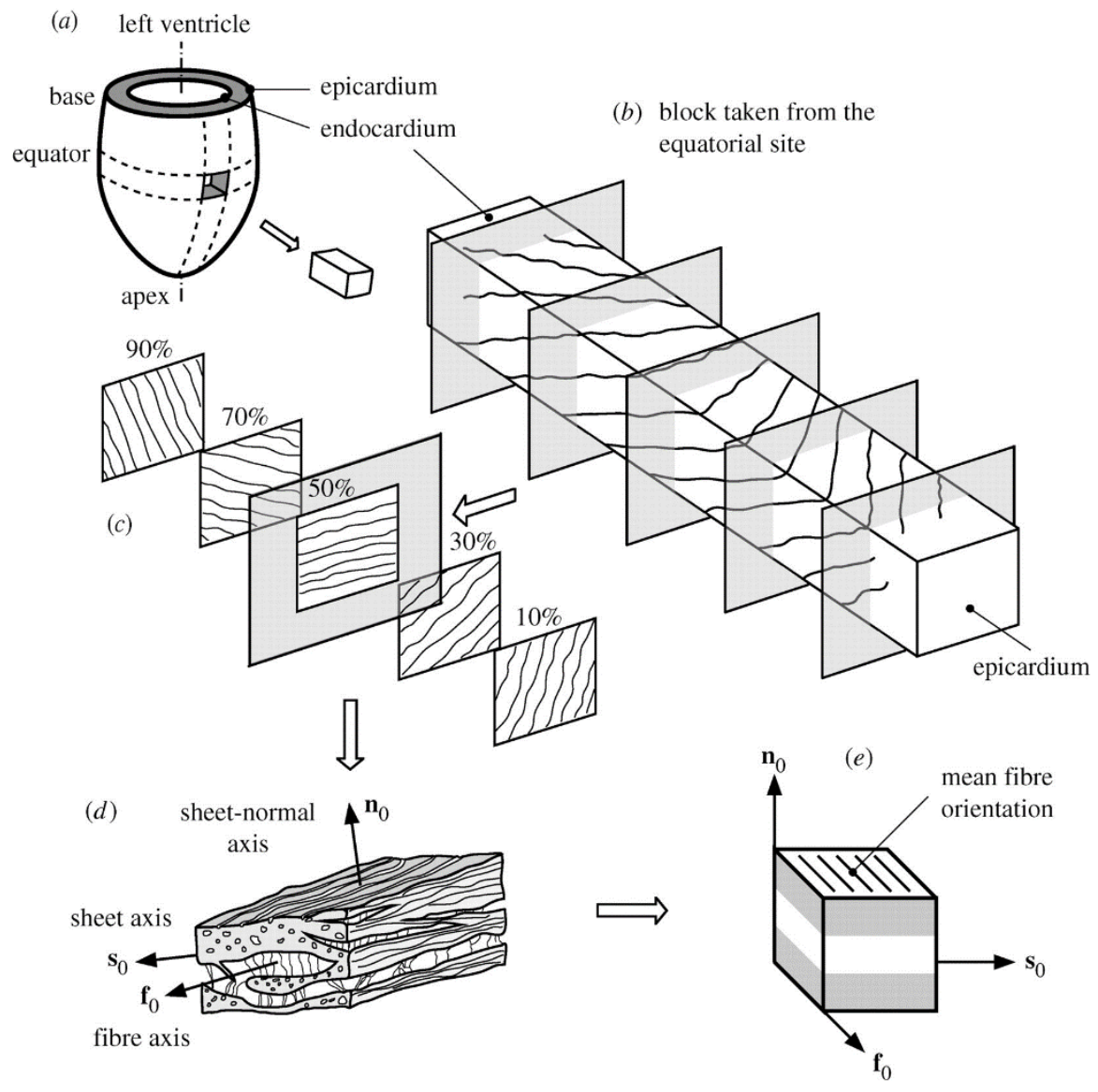


Figure 2.2: (a) The left ventricle and a cutout from the wall; (b) the structure through the thickness from the epicardium to the endocardium; (c) Transmural variation of fibers at five longitudinal-circumferential sections at regular intervals from 10 to 90 per cent of the wall thickness; (d) the layered organization of myocytes and the collagen fibres between the sheets referred to a right-handed orthonormal coordinate system with fibre axis f_0 , sheet axis s_0 and sheet-normal axis n_0 ; and (e) a cube of layered tissue showing local material coordinates (f_0, s_0, n_0) . The figure is adapted from [130].

Let, $\chi_{\kappa_0}(X,t)$ describes the mapping from an unloaded reference configuration κ_0 with position X to a current configuration κ with the corresponding material position $x = \chi_{\kappa_0}(X,t)$. The displacement field is given by u = x - X and the deformation gradient tensor is defined

as $\mathbf{F} = \frac{\partial \mathbf{x}}{\partial \mathbf{X}}$. In the volumetric growth framework, the deformation gradient tensor, \mathbf{F} , is multiplicatively decomposed into an elastic and a growth tensor as follows

$$\mathbf{F} = \mathbf{F}_{\mathbf{e}} \mathbf{F}_{\mathbf{g}} \,, \tag{2.1}$$

Here F_e and F_g are the elastic and growth deformation gradients, respectively. The growth deformation gradient F_g was described by

$$F_g = \theta_f f_0 \otimes f_0 + \theta_s s_0 \otimes s_0 + \theta_n n_0 \otimes n_0 , \qquad (2.2)$$

where, f_0 , s_0 and n_0 are the local myofiber, sheet, and sheet-normal directions in the reference configuration, respectively (Figure 2.2).

The evolution of the growth multipliers associated with the deviations of a prescribed stimulant s_i from its homeostatic value $s_{i,h}$ is given by

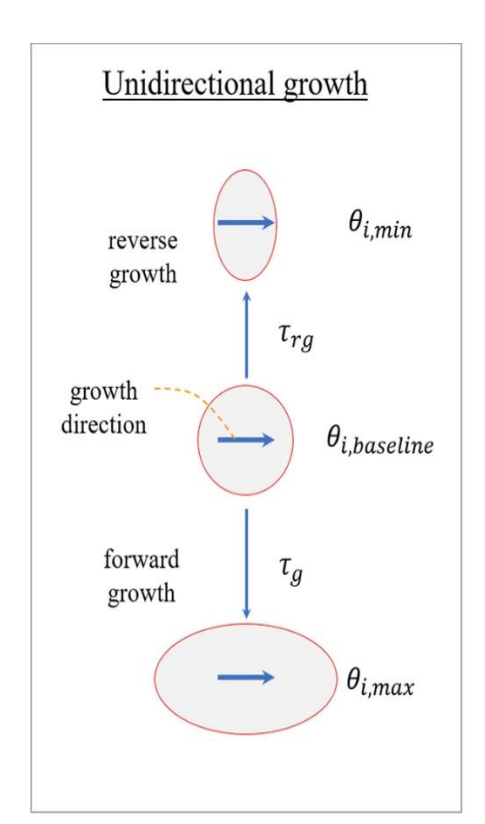
$$\dot{\theta}_i = k_i(\theta_i, s_i) g_i(s_i, s_{i,h}), \tag{2.3}$$

where $\dot{\theta}_i$ is the derivative of growth multipliers with respect to time t. Based on the local stimulus, the function $g_i(s_i, s_{i,h})$ is prescribed as $g_i(s_i, s_{i,h}) = s_i - s_{i,h}$. The rate limiting function, which restricts forward and reverse growth rates, is defined as follows

$$k_{i}(\theta_{i}, s_{i}) = \begin{cases} \frac{1}{\tau_{g,i}} \left(\frac{\theta_{max,i} - \theta_{i}}{\theta_{max,i} - \theta_{min,i}} \right)^{\gamma_{g,i}} & \text{if } g_{i}(s_{i}, s_{i,h}) \geq 0\\ \frac{1}{\tau_{rg,i}} \left(\frac{\theta_{i} - \theta_{min,i}}{\theta_{max,i} - \theta_{min,i}} \right)^{\gamma_{rg,i}} & \text{if } g_{i}(s_{i}, s_{i,h}) < 0 \end{cases}$$

$$(2.4)$$

where the subscript $i \in f$, s, n denote the association with the myofiber, sheet, and sheet-normal directions. The growth constitutive model parameters are $\tau_{g,i}$, $\gamma_{g,i}$, $\tau_{rg,i}$ and $\gamma_{rg,i}$. The application of rate-limiting function are two folds. One, it restricts the evolution of the growth multipliers θ_i within some prescribed limits. Second, prescribing different value of k_i in each i direction enables a broad spectrum of anisotropic growth deformation.



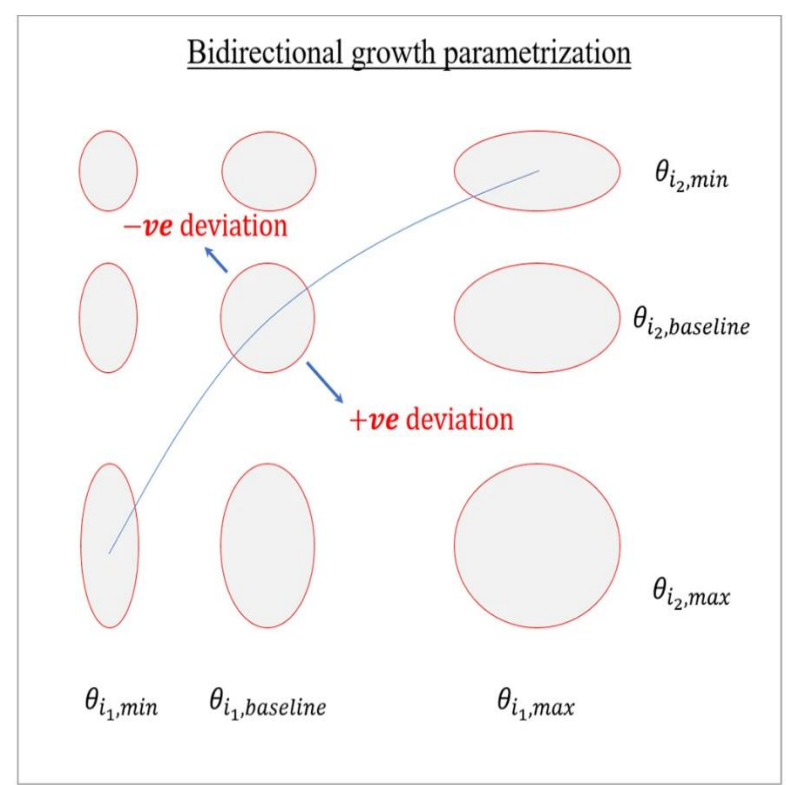


Figure 2.3: Schematic of the anisotropic growth evolution in response to local stimulus.

Maximum elastic myofiber stretch was prescribed as the growth stimuli in all 3 material directions. The myofiber stretch is defined as

$$\lambda_f = \sqrt{f_0 \cdot C \cdot f_0} \,, \tag{2.5}$$

where *C* denotes the right Cauchy-Green deformation tensor with respect to the end-diastolic configuration. Positive deviations from the homeostatic point will results towards the evolution of maximum growth multiplier, whereas negative deviations from the homeostatic point will drag the evolution towards the minimum as depicted in **Figure 2.3.**

2.2.2 Electrophysiology model

Based on modified Fitzhugh-Nagumo model, cardiac electrical activity and its propagation was modeled. Specifically, the spatio-temporal evolution of cardiac action potential φ is described in the reference configurations by

$$\dot{\varphi} = div(\mathbf{D}grad\varphi) + f_{\varphi}(\varphi, r) + I_{s}, \qquad (2.6)$$

$$\dot{r} = f_r(\varphi, r) \quad , \tag{2.7}$$

where D is the anisotropic electrical conductivity tensor, I_s is the constant electrical stimulus for prescribing local excitation initiation during pacing, and r is a dimensionless recovery variable. The excitation properties of cardiac tissue are defined by

$$f_{\varphi} = c\varphi \left(\varphi - a\right)(1 - \varphi) - r\varphi , \qquad (2.8)$$

$$f_r = \left(\gamma + r \frac{\mu_1}{\mu_2 + \varphi}\right) \left(-rc\varphi(\varphi - b - 1)\right),\tag{2.9}$$

Here c, α , b, γ , μ_1 and μ_2 are the Fitzhugh-Nagumo model parameters.

2.2.3 Mechanics model

Mechanical behavior of the cardiac tissue was described by an active stress formulation. In this formulation, mechanical behavior is additively decomposed into a passive component and an active component. More specifically, the second Piola-Kirchhoff or PK2 stress tensor S has a passive component, S_p and an active component, S_a , i.e.

$$S = S_p + S_a , (2.10)$$

Passive mechanical properties is described using the following Fung-type strain energy function

$$w(\mathbf{E}) = \frac{c}{2}(e^{Q} - 1.0), \tag{2.11a}$$

$$Q = b_f E_{ff}^2 + b_{fs} \left(E_{fs}^2 + E_{sf}^2 + E_{fn}^2 + E_{nf}^2 \right) + b_{xx} \left(E_{ss}^2 + E_{nn}^2 + E_{ns}^2 + E_{sn}^2 \right), \tag{2.11b}$$

In the above equations, C, b_f , b_{fs} , b_{xx} are material parameters. And E_{ij} with $(i,j) \in (f, s, n)$ denote components of the elastic Green-Lagrange strain tensor, $\mathbf{E} = \frac{1}{2}(\mathbf{F}_e^T \mathbf{F}_e - 1)$. The passive stress is determined from the strain energy function by

$$S_p = \frac{\partial w(E_e)}{\partial E_e} , \qquad (2.11c)$$

Based on a phenomenological active contraction model, active mechanical behavior of the cardiac tissue is described by an active stress tensor directed in the myofiber direction, i.e.,

$$S_a = T_{max} \frac{Ca_0^2}{1 + ECa_{50}^2(E_{ff})} \frac{1 - \cos(\omega(t, t_{init}, E_{ff}))}{2} f_0 \otimes f_0, \qquad (2.12a)$$

$$ECa_{50} = \frac{(Ca_0)_{max}}{\sqrt{\exp(B(l-l_0))-1}},$$
(2.12b)

Here, T_{max} , Ca_0 , and ECa_{50} are the scaling factor associated with the tissue contractility, the peak intracellular calcium concentration and the length-dependent calcium sensitivity, respectively. Also, $(Ca_0)_{max}$, B, l_0 are the maximum peak intracellular calcium concentration, a material constant, and the sarcomere length at which no active tension develops, respectively. The instantaneous sarcomere length is defined as $l = l_{s0}\sqrt{f_0 \cdot C \cdot f_0}$ with the prescribed initial length of sarcomere, l_{s0} .

To incorporate a spatially heterogeneous activation initiation time, $t_{init}(X)$, the active contraction model is modified in the function ω i.e.,

$$\omega = \begin{cases} \pi \frac{t_{sa}}{t_0} & \text{if } 0 \le t_{sa} < t_0, \\ \pi \frac{t_{sa} - t_0 + t_r}{t_r} & \text{if } t_0 \le t_{sa} < t_0 + t_r, \\ 0 & \text{if } t_0 \le t_{sa} < t_0 + t_r, \end{cases}$$
(2.12c)

Here, t_0 is the prescribed time to maximum active tension and t_r is the sarcomere length-dependent active tension relaxation time that is given by $t_r = ml + b$ with parameters m and b. Time since activation $t_{sa}(X) = t_{current} - t_{init}(X)$ couples cardiac electrophysiology and mechanics, where $t_{current}$ denotes the current time in the cardiac cycle and $t_{init}(X)$ defines the local initiation time that is given as

$$t_{init}(X) = \inf\{t(X)|\varphi(X,t) \ge 0.9\},$$
 (2.13)

2.2.4 Computational approximation

Finite element formulation of the BiV mechanics problem was obtained by minimizing the following Lagrangian functional [128, 131]

$$\mathcal{L} = \int_{\Omega} \Psi_{T}(\boldsymbol{u}) dV - \int_{\Omega} p(J-1)dV - P_{LV}(V_{LV,cav}(\boldsymbol{u}) - V_{LV}) - P_{RV}(V_{RV,cav}(\boldsymbol{u}) - V_{RV}) - \frac{1}{2} \int_{d\Omega_{eni}} k_{spring}(\boldsymbol{u}.\boldsymbol{u})dS - \frac{1}{2} \int_{d\Omega_{h}} k_{spring}(\boldsymbol{u}.\boldsymbol{u})dS - \boldsymbol{c}_{1} \int_{\Omega} \boldsymbol{u}dV - \boldsymbol{c}_{2} \int_{\Omega} \boldsymbol{X} \times \boldsymbol{u}dV,$$
 (2.14)

In Eq. (2.14), Ψ_T is the total strain energy of the myocardium, $\mathbf{u} \in \mathbf{H}^1(\Omega_0)$ is the displacement field. On the other hand, $(P_{LV}, P_{RV}) \in R$, $p \in L_2(\Omega_0)$, $\mathbf{c}_1 \in R^3$ and $\mathbf{c}_2 \in R^3$ are the Lagrange multipliers for, respectively, constraining the cavity volume $V_{LV,cav}(\mathbf{u})$ and $V_{RV,cav}(\mathbf{u})$ to the prescribed value V_{LV} and V_{RV} , respectively, enforcing incompressibility in which the Jacobian of the deformation gradient tensor J=1, enforcing zero mean translation and enforcing zero mean rotation, respectively. Spring (robin-type) boundary conditions with spring constant k_{spring} and $k_{spring2}$ were also imposed on the epicardial surface $d\Omega_{epi}$ and base $d\Omega_b$, respectively.

The approximate solution of the weak formulation of the acute electromechanics problem are obtained from solving Euler-Lagrange problem by finding $\boldsymbol{u} \in H^1(\Omega^-), p \in L^2(\Omega^-), P_{LV} \in \mathbb{R}, P_{RV} \in \mathbb{R}, \boldsymbol{c}_1 \in \mathbb{R}^3$, $\boldsymbol{c}_2 \in \mathbb{R}^3$, $\boldsymbol{\varphi} \in H^1(\Omega^-)$, $r \in H^0(\Omega^-)$ that satisfies

$$\begin{split} \delta \mathcal{L} &= \int_{\Omega} \; (\boldsymbol{F} \boldsymbol{S} - J \boldsymbol{F}^{-T}) : \nabla \delta u \; dV - \int_{\Omega} \; \delta p(J-1) dV - P_{LV} \int_{\Omega_{LV}} J \boldsymbol{F}^{-T} : \nabla \delta u \; dV - \\ & P_{RV} \int_{\Omega_{RV}} J \boldsymbol{F}^{-T} : \nabla \delta u \; dV - \delta P_{LV} \big(V_{LV,\text{cav}}(\boldsymbol{u}) - V_{LV} \big) - \delta P_{RV} \big(V_{RV,\text{cav}}(\boldsymbol{u}) - V_{RV} \big) - \\ & \delta \boldsymbol{c_1} \cdot \int_{\Omega} \; \boldsymbol{u} \; dV - \; \delta \boldsymbol{c_2} \cdot \int_{\Omega} \; \boldsymbol{X} \times \boldsymbol{u} \; dV - \boldsymbol{c_1} \cdot \int_{\Omega} \; \delta \boldsymbol{u} \; dV - \; \boldsymbol{c_2} \cdot \int_{\Omega} \; \boldsymbol{X} \times \delta \boldsymbol{u} \; dV - \end{split}$$

$$\int_{\delta\Omega_{eni}} k_{spring} \mathbf{u} \cdot \delta \mathbf{u} \, dS - \int_{\delta\Omega_b} k_{spring2} \mathbf{u} \cdot \delta \mathbf{u} \, dS = 0, \tag{2.15a}$$

$$\int_{\Omega} (\varphi - \varphi_n) \Delta t^{-1} \delta \varphi = \int_{\Omega} \mathbf{D} \operatorname{grad} \varphi. \operatorname{grad} \delta \varphi + \int_{\Omega} (f_{\varphi} + I_s) \delta \varphi, \tag{2.15b}$$

$$\int_{\Omega} (r - r_n) \Delta t^{-1} \delta r = \int_{\Omega} f_r \, \delta \varphi, \tag{2.15c}$$

for all test functions $\delta \boldsymbol{u} \in H^1(\Omega)$, $\delta p \in L^2(\Omega)$, $\delta P_{LV} \in \mathbb{R}$, $\delta P_{RV} \in \mathbb{R}$, $\delta \boldsymbol{c}_1 \in \mathbb{R}^3$, $\delta \boldsymbol{c}_2 \in \mathbb{R}^3$, $\delta \varphi \in H^1(\Omega)$, $\delta r \in H^0(\Omega)$. In Eq. (2.15), $\delta \boldsymbol{u}$, δp , δP_{LV} , δP_{RV} , $\delta \boldsymbol{c}_1$, $\delta \boldsymbol{c}_2$ are the first variation of the displacement field, Lagrange multipliers for enforcing incompressibility (J=1)

and volume constraint for LV and RV, zero mean translation and rotation, respectively. Besides, $\delta \varphi$, δr are the first variation of the action potential and recovery state variable, respectively. Spring constants k_{spring} and $k_{spring2}$ are associated with boundary conditions imposed at epicardium and basal surface, respectively.

Similarly, approximate solution of the weak formulation of the G&R problem were obtained from solving Euler-Lagrange problem by finding $\boldsymbol{u} \in H^1(\Omega_{-})$, $p \in L^2(\Omega_{-})$, that satisfies $\delta \mathcal{L}_G = \int_{\Omega_{-}} (\boldsymbol{F}\boldsymbol{S} - J\boldsymbol{F}^{-T})$: $\operatorname{grad} \delta \boldsymbol{u} \, dV - \int_{\Omega_{-}} \delta p(J-1) dV - \int_{\delta\Omega_{epi}} k_{spring} \boldsymbol{u} \cdot \delta \boldsymbol{u} \, dS = 0$, (2.16) for all test functions $\delta \boldsymbol{u} \in H^1(\Omega_{-})$, $\delta p \in L^2(\Omega_{-})$. Here, k_{spring} is associated with boundary conditions imposed at epicardium.

2.2.5 Simulation scheme

Two cases differing in terms of the prescribed activation initiation location were simulated. These cases are, namely,

- *Normal:* activation was initiated at the septum near the base,
- *Pacing:* activation was initiated at the LVFW near the base.

Table 2.2: Growth Parameters

Direction	$ au_g$	$ au_{rg}$	γ	θ_{min}	θ_0	θ_{max}
	Days	Days	Days	(no units)	(no units)	(no units)
$ heta_f$	3.8	9.6	1.0	0.5	1.0	2.0
θ_s	9.6	3.8	1.0	0.5	1.0	2.0
θ_n	9.6	3.8	1.0	0.5	1.0	2.0

A schematic of the simulation timeline and pacing location is shown in **Figure 2.1**. The homeostatic set point for the maximum elastic myofiber stretch in the growth constitutive model was prescribed using the local values obtained from the *Normal* case with septal activation.

Deviations of the maximum elastic myofiber stretch in the *Pacing* case from the homeostatic values were used as growth stimuli. The calibrated growth parameters are mentioned in **Table2.2.**

2.3 Results & Discussion

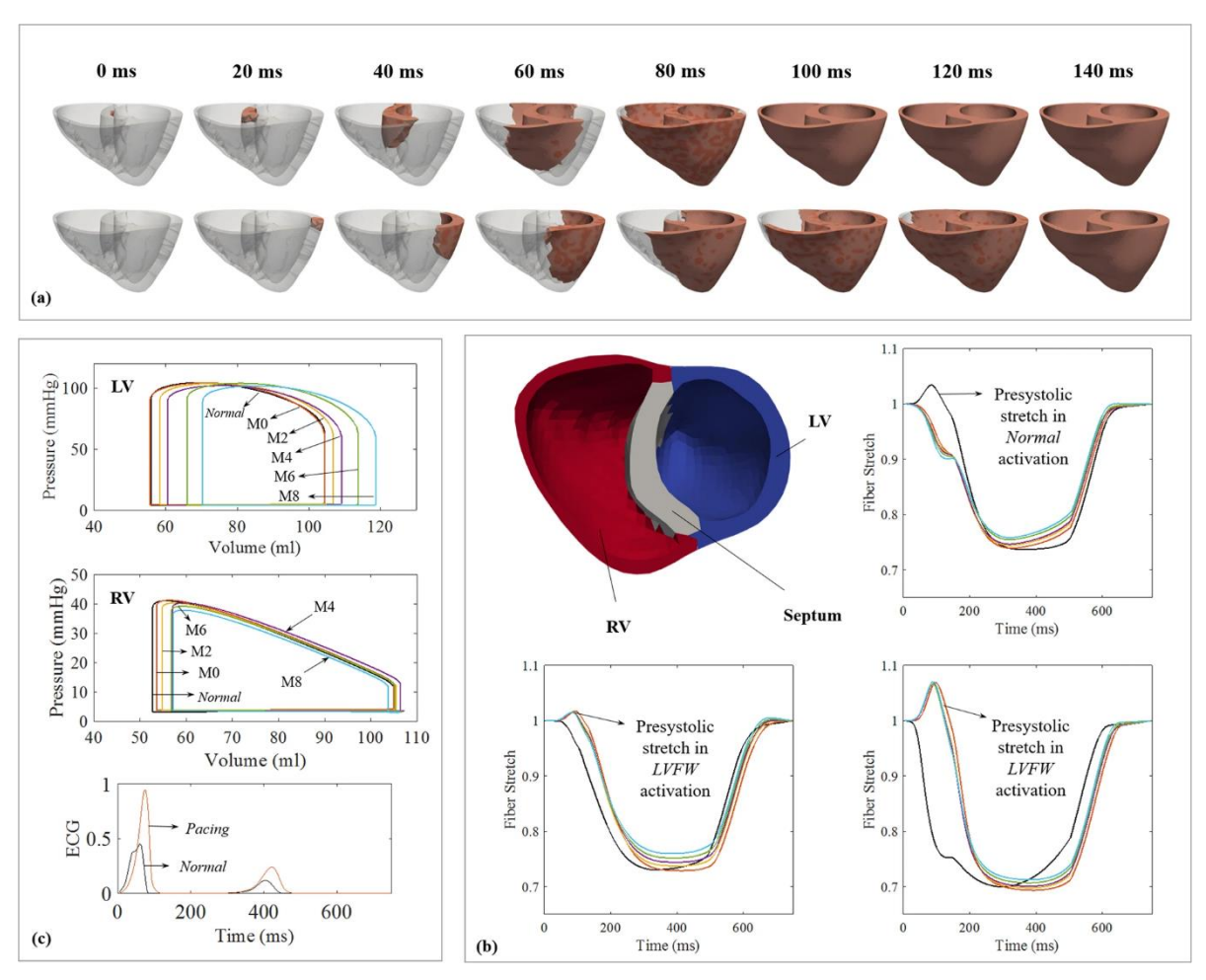


Figure 2.4: (a) Propagation of the depolarization isochrones in the Normal (top) and Pacing (bottom) cases. (b)Long term changes in RV (left) and LV (right) PV loops in the Pacing case; M0–8 denote results at 0–8 month. Refer to (c) for line color. (c) Myofiber stretch, λ_f , as a function of time over a cardiac cycle at 0–8 month. Normal case is in black.

Our simulations showed that due to the presence of electromechanics alterations induced by LVFW pacing, a pre-stretch occurs at the late activated regions (Septum + RVFW) in the beginning of systole (Figure 2.4) that produced a higher maximum elastic myofiber stretch

compared to the homeostatic set point value (during normal activation) found in those regions. On the other hand, the early activated region (LVFW) has a lower maximum elastic myofiber stretch when compared to its corresponding homeostatic set point value. These results are consistent with observations in animal models of asynchronous activation [132, 133] and LBBB patients [21], where abnormal stretching of the tissue at the beginning of systole (i.e., pre-systolic stretching) was found at the late activated regions. Consequently, myofiber stretch in the septum + RVFW and LVFW of the *Pacing* case deviated positively and negatively from the homeostatic value in the *Normal* case. This heterogeneity in myofiber stretch λ_f resulted in the evolution of growth scalars θ_i 's towards $\theta_{i,max}$ in the late activated septum/RV, and $\theta_{i,max}$ in the early-activated LVFW, leading to long-term asymmetrical geometrical changes.

Using the alteration of elastic myofiber stretch as a stimulant for G&R in all 3 material directions, the model predictions, after appropriate calibration of parameters, were compared with local and global measurements in experiments where a similar chronic LVFW pacing protocol was applied to the canine model [43, 44]. In terms of long-term hemodynamic changes in the LV and RV (Figure 2.3c), there was no immediate substantial reduction in the pump function in the *Pacing* case (0 month). Changes were, however, noticeable at 2 months with the onset of progressive LV dilation. Specifically, in the span of 8 months, LV end-diastolic volume (EDV) increased from 104.3 ml to 118.6 ml whereas end-systolic volume (ESV) increased from 55.65 ml to 70.3 ml. This led to a rightward shift in the LV PV loop that was accompanied by a slight reduction in ejection fraction (EF) from 48.7% to 48.3% at 8 months. On the other hand, the simulations also show long-term changes of the RV PV loops arising largely from the thickening of septum. RV EDV was slightly decreased from 104.9 ml to 103.7 ml whereas RV ESV increased from 53.6 ml to 57.1 ml at 8 months.

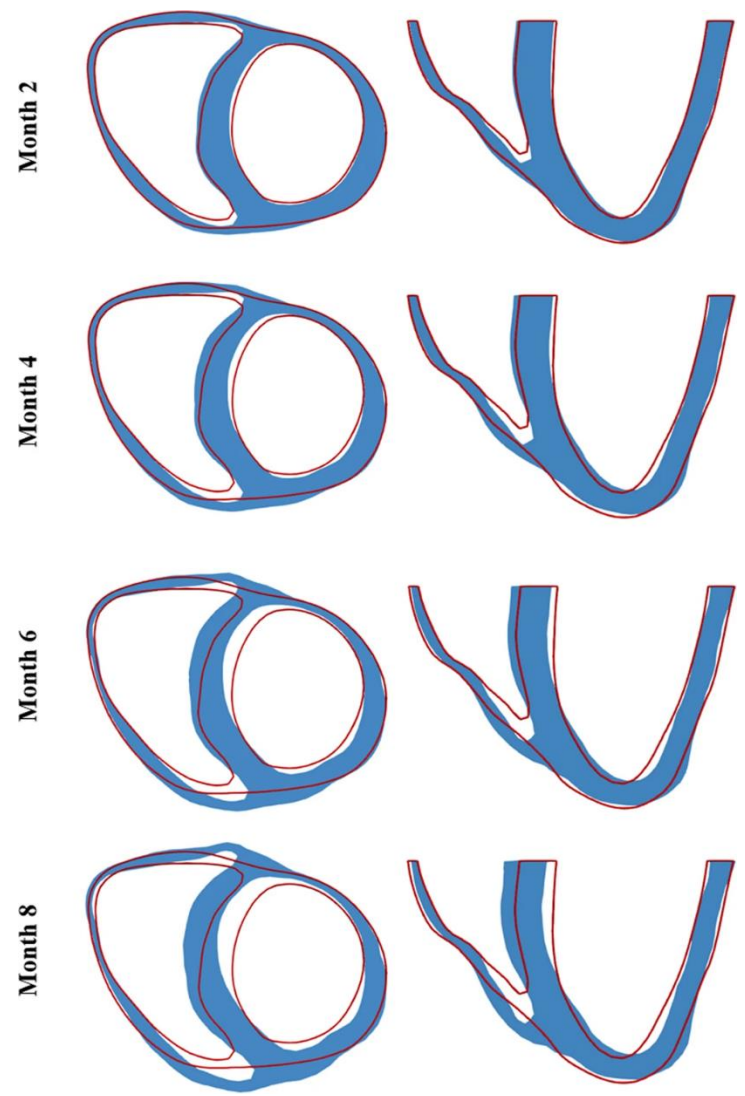


Figure 2.5: Long-term changes in biventricular geometry (blue) are superimposed on the original (red outline). Left: short-axis view; Right: long-axis view.

Long-term changes in the geometry is highly asymmetrical in the biventricular unit in the *Pacing* case with radial wall thickening occurring at the late-activated septum and wall thinning occurring at the early-activated LVFW (**Figure 2.5**). In terms of local geometrical changes (**Figure 2.6**), the model predicted an increase in septum wall thickness by 18.5% (cf. $23 \pm 12\%$ in the experiments [43]) and a decrease in LVFW thickness by 19.7% (cf. $17 \pm 17\%$ in the experiments [43]) after 6 months of pacing. In terms of global geometrical changes, the model predicted an increase in LV EDV by 9% (cf. $7.4 \pm 29\%$ in the experiments) and LVFW + Septum wall volume

by 9.5% (cf. $15 \pm 17\%$ in the experiments) for the same duration. The chronic features of LVFW pacing predicted by the model are also found in LBBB [118], which produces MD via an opposite activation pattern (i.e., septum is activated first followed by the LVFW).

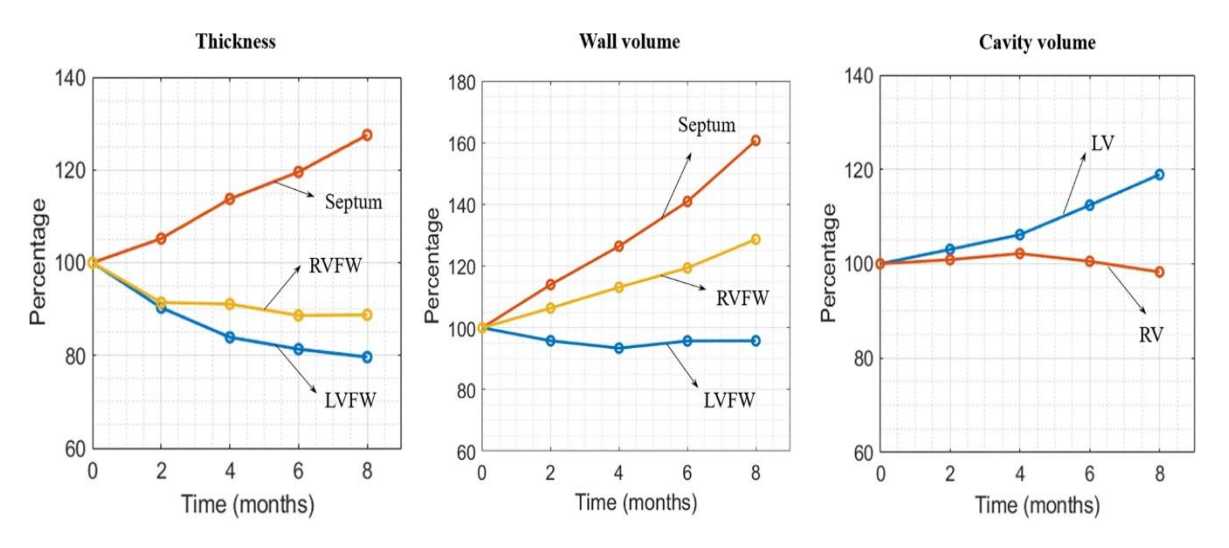


Figure 2.6: Long-term local geometrical changes. Left: wall thickness; Middle: wall volume; Right: Cavity volume.

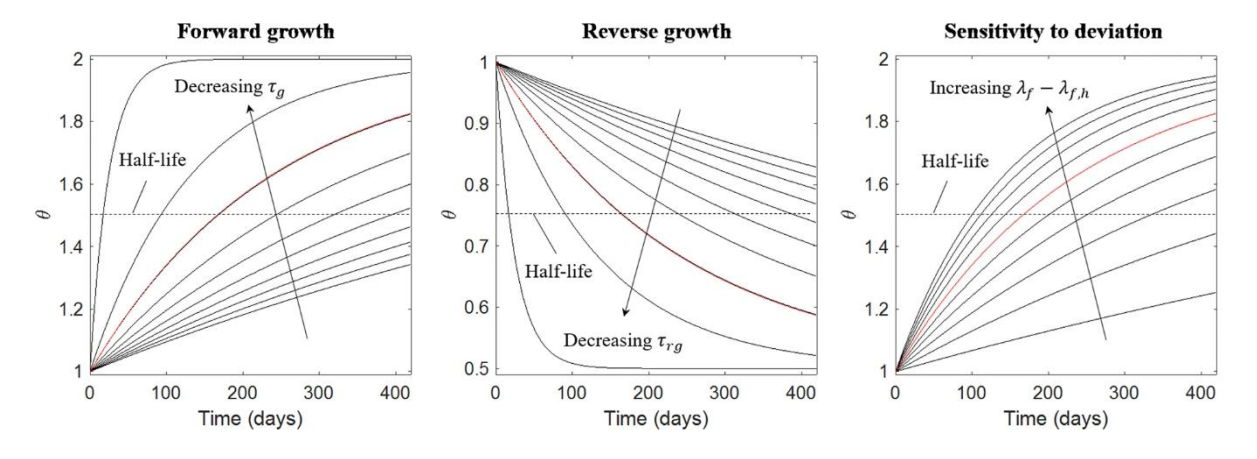


Figure 2.7: Effect of varying G&R parameters. Changes in Left: τg from 40.0 to 1.0 for $\lambda_f - \lambda_{f,h} = 0.06$; Middle: τ_g from 40.0 to 1.0 for $\lambda_f - \lambda_{f,h} = -0.06$; Right: $\lambda_f - \lambda_{f,h}$ from 0.01 to 0.1 for $\tau_g = 9.6$. Red: Parameter values in **Table 2.2**.

Calibration of G&R parameters showed that in order to reproduce asymmetrical hypertrophy, it is necessary to impose different forward growth rate τ_g and reverse growth rate τ_{rg}

not only because of the heterogeneity in myofiber stretch in heart, but also due to the high sensitivity of the G&R parameters to the deviation (**Figure 2.7**).

2.4 Conclusion

With appropriate calibration, we showed that the prescription of a single growth stimuli based only on the elastic myofiber stretch can quantitatively reproduce the largely local G&R features found with MD (**Table 2.1**), which reinforce the theory that transverse growth maybe controlled, at least to some extent, by elastic myofiber stretch.

CHAPTER 3 ANIMAL SPECIFIC LEFT VENTRICULAR MODEL ON PRESSURE OVERLOAD

3.1 Introduction

LV afterload as reflected by an elevated systolic pressure [45] can lead to acute changes in cardiac mechanics and produce chronic G&R. An increase in afterload caused by pathological conditions (e.g., aortic stenosis and hypertension) can impair longitudinal myocardial deformation and produce local changes in myocardial stresses and stretches, which in turn, can trigger the development of concentric hypertrophy. Several computational models [30, 32] focusing mostly on global G&R features during pressure overload have been developed. These models, however, do not consider local/regional G&R features and how they are correlate with changes in the local stresses or strains, which can provide insights into which mechanical quantity is driving G&R.

To address this issue, we used a combination of computational modeling and experiments to investigate whether normal stresses or strains along 3 orthogonal material directions can better correlate with regional measurements of growth in swine models during aortic banding. While changes in stretch in the pressure overloaded hearts can, in principle, be measured experimentally, the combination of a complex ventricular wall structure with highly nonlinear mechanical behavior and the limitations of current available techniques, however, do not allow for stresses in the muscle fibers to be quantified directly through experiment [11]. As such, we developed animal-specific finite element (FE) models of the LV to simulate the acute effects of pressure overload and estimate the regional changes in normal stresses or strains, which were then correlated with the corresponding regional growth.

3.2 Methods

3.2.1 LV geometry model

Left ventricular geometries segmented from the 3D echocardiography (3D echo) images were discretized using (~4000) tetrahedral elements (**Figure 3.1**), which is sufficient for

convergence based on a previous study using a biventricular mesh [134]. Myofiber direction f_o , was prescribed based on a linear transmural variation of the helix angle from 60° at the endocardium to -60° at the epicardium [135] across the wall using a Laplace-Dirichlet rule-based algorithm [136].

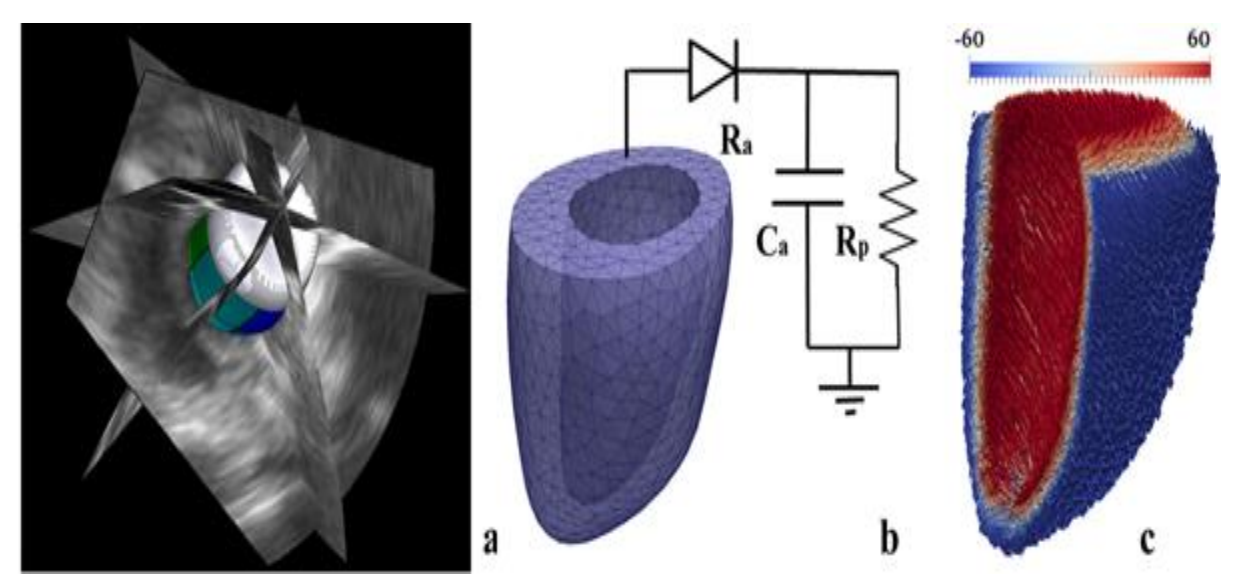


Figure 3.1: Construction of animal-specific LV FE model. (a) Segmentation of LV surfaces from 3D echo images, (b) Meshing of geometry to construct a LV FE model that is connected to a 3-element Windkessel model [137] (c) Transmural distribution of myofiber angle from $+60^{\circ}$ at endocardium to -60° at epicardium is prescribed in the LV FE model.

3.2.2 Experimental measurements

Measurements were acquired *in vivo* from the animals before aortic constriction (baseline) and 2 weeks after aortic constriction (growth). Specifically, aortic and LV pressure waveforms were measured using catheterization while 3D echo (EPIQ-C system, Philips Healthcare, Andover, MA, USA) was performed on the animals from which the LV geometry and volume waveforms were acquired. The LV pressure and volume waveforms were synchronized to obtain pressure-volume (PV) loops in each animal at baseline and after growth. Based on the LV geometry segmented from 3D echo, we also computed the regional thickness by measuring the local shortest distance between the endocardium and epicardium. The local regional wall thickness was projected

on the endocardium and regional growth was indexed by the difference between thickness at baseline and after growth.

3.2.3 Mechanics model

Left ventricular mechanics was described using an active stress formulation, where total stress tensor was additively decomposed into an active and a passive component. The passive mechanics model is briefly described in **section 2.2.3** by Eq. 2.11. Active mechanics was described using an active contraction model modified from that of Guccione et al. [138, 139] with the active stress tensor given as

$$S_a = T_{max} \left(\frac{Ca_0^2}{Ca_0^2 + ECa_{50}^2} \right) C_t f_0 \otimes f_0, \tag{3.1a}$$

$$C_t = \frac{1}{2} \left(1 - \cos \omega \right), \tag{3.1b}$$

$$\omega = \begin{cases} \pi \frac{t}{t_0}; & 0 \le t < t_0 \\ \pi \frac{t - t_0 + t_r}{t_r}; & t_0 \le t < t_0 + t_r, \\ 0; & t_0 + t_r \le t \end{cases}$$
(3.1c)

$$t_r = ml + b, (3.1d)$$

In Eq. (3.1), T_{max} is the isometric tension achieved at the longest sarcomere length, Ca_0 denotes the peak intracellular calcium concentration, ECa_{50} is the length dependent calcium sensitivity. The parameter t_0 is the prescribed time to maximum active tension, whereas t_r denotes the duration of relaxation that varies linearly with the instantaneous sarcomere length governed by parameters m and b.

3.2.4 Finite element formulation

Finite element formulation of the LV mechanics problem was obtained by minimizing the following Lagrangian functional [128, 131]

$$\mathcal{L}(\boldsymbol{u}, P, c_1, c_2) = \int_{\Omega_0} \Psi_T(\boldsymbol{u}) dV - \int_{\Omega_0} p(J-1) dV - P(V_{cav}(\boldsymbol{u}) - V_p) - \frac{1}{2} \int_{d\Omega_{0,epi}} k_{spring}(\boldsymbol{u}, \boldsymbol{u}) dS - c_1 \int_{\Omega_0} \boldsymbol{u} dV - c_2 \int_{\Omega_0} \boldsymbol{X} \times \boldsymbol{u} dV,$$
(3.2)

In Eq. (3.2), Ψ_T is the total strain energy of the myocardium, $\mathbf{u} \in H^1(\Omega_0)$ is the displacement field. On the other hand, $P \in R$, $p \in L_2(\Omega_0)$, $\mathbf{c}_1 \in R^3$ and $\mathbf{c}_2 \in R^3$ are the Lagrange multipliers for, respectively, constraining the cavity volume $V_{cav}(\mathbf{u})$ to the prescribed value V_p , enforcing incompressibility in which the Jacobian of the deformation gradient tensor J=1, enforcing zero mean translation and enforcing zero mean rotation, respectively. A spring (robin-type) boundary condition with spring constant k_{spring} was also imposed on the epicardial surface $d\Omega_{0,epi}$ to describe the loading by the pericardial fluid.

The weak formulation was then obtained by taking the first variation of the Lagrangian functional as follows:

$$\begin{split} \delta \mathcal{L}(\boldsymbol{u}, \mathbf{p}, \mathbf{P}, c_1, c_2) &= \int_{\Omega_0} \boldsymbol{F} \boldsymbol{S} : \operatorname{grad} \delta \boldsymbol{u} \ dV - \int_{\Omega_0} \left(p J \boldsymbol{F}^{-T} : \operatorname{grad} \delta \boldsymbol{u} \ + \ \delta p (J-1) \right) dV - \\ \delta P \left(V_{cav}(\boldsymbol{u}) - V_p \right) - \int_{\Omega_{cav}} P J \boldsymbol{F}^{-T} : \operatorname{grad} \delta \boldsymbol{u} \ dV - \int_{d\Omega_{0,epi}} k_{spring}(\boldsymbol{u}. \delta \boldsymbol{u}) dS - \\ \int_{\Omega_0} (c_1 \delta \boldsymbol{u} \ + \boldsymbol{u} \delta c_1) dV - \int_{\Omega_0} \{ \delta c_2 (\boldsymbol{X} \times \boldsymbol{u}) + c_2 (\boldsymbol{X} \times \delta \boldsymbol{u}) \} dV = 0, \end{split}$$
(3.3)

In the above equation, $\delta u \in H^1(\Omega_0)$, $\delta p \in L^2(\Omega_0)$, $\delta P \in R$, $\delta c_1 \in R^3$, $\delta c_2 \in R^3$ are the test functions corresponding to u, p, P, c_1 and c_2 , respectively. Displacement at the LV base was constrained from moving out of plane i.e.,

$$\mathbf{u}.\,\mathbf{n}_{\mathsf{base}}\,=\,0,\tag{3.4}$$

The displacement field u(X) and Lagrange multiplier p were interpolated using quadratic and linear tetrahedral elements, respectively. An implicit backward Euler scheme was used for

numerical time-integration with a fixed time step. The modeling framework was implemented using the open-source FE library FEniCS [140].

3.2.5 Simulation cases

We considered two simulation cases for each of the 4 swine models:

- **Baseline**: Before a ortic banding was performed on the animals
- Acute overload: Acute effects of aortic banding

To simulate aortic constriction in the acute (immediate) pressure overload cases, only parameters of the Windkessel model were adjusted to match the elevated peak systolic pressure measured at 2nd week after aortic banding in the animals. As the pressure was not measured immediately after banding, we assumed that the elevated pressure associated with aortic banding was sustained for the 2 weeks. Also, we assumed that end-diastolic volume was not changed immediately after aortic banding based on a previous canine study by Crozatier et al. [141], which found no increase in acute end-diastolic diameter after aortic stenosis in most of the animals. Other model parameters as well as myofiber orientation distribution in the acute overload case for each swine were prescribed to be the same as those in the corresponding baseline case.

3.3 Results & Discussion

Experimental measurements of four swine models before and after 2 weeks of aortic banding are tabulated in **Table 3.1**. A significant increase in the mean peak systolic pressure (~43%) was found in the post aortic banding animals. Mean EDV was increased (~10%) while mean EF was decreased (~5% absolute) after 2 weeks of banding. Mean aortic pressure was also increased (~53%) whereas average maximum and minimum thickness remained relatively unchanged. The mean septum thickness was decreased (~10%), however, while the mean free-wall thickness was increased (~8%). The experimental results are consistent with previous studies of

pressure overload using aortic constriction large animal (porcine and sheep) model, which reported an increase in systolic pressure (~27% vs. ~42% here), elevated aortic pressure gradient (~40 mmHg vs. ~31 mmHg here), increase in LV diameter and EDV [142–144]. The increase in LVFW thickness found here is also consistent with a study, which reported an increase in posterior wall thickness (~31% vs. ~8% here) and a reduction in EF (~12% vs. ~10% here) after 2 weeks of aortic constriction in a mouse model [145]. We note, however, that some experimental studies have reported a decrease in EDV (~31%) (over a longer time period of 4 weeks) in a swine model of severe aortic stenosis [146] and preserved ejection fraction [147].

Table 3.1: Experimental measurements

Parameters	0th Week	2nd Week
End Diastolic Volume, EDV (ml)	72 ± 14.38	79 ± 19.18
End Diastolic Pressure, EDP (mm Hg)	14.4 ± 5.23	28.48 ± 16.3
End Systolic Volume, ESV (ml)	39 ± 8.5	46.27 ± 10.04
Stroke volume, SV (ml)	33 ± 7	32.35 ± 10
Ejection Fraction, EF (%)	46 ± 3	41 ± 3
Peak Systolic pressure (mm Hg)	79 ± 8.41*	112.36 ± 16*
Aortic Pressure (mm Hg)	58 ± 3	89 ± 19
Maximum Thickness (mm)	13 ± 4	13 ± 2.06
Minimum Thickness (mm)	5 ± 1	5 ± 1
Septum Thickness (mm)	11 ± 3	9.49 ± 2.02
LV Free wall Thickness (mm)	9 ± 2	9.4 ± 1.22
Wall volume (ml)	63 ± 23	66 ± 13

Data are expressed as mean \pm SD. * α < 0.05

Regional wall thickness and growth as indexed by the change in the LV wall thickness before and after banding are shown in **Figure 3.2.** In 3 swine models (1–3), the septum became thinner, and the LV free wall became thicker after banding. In swine model 4, both septum and free wall are thickened.

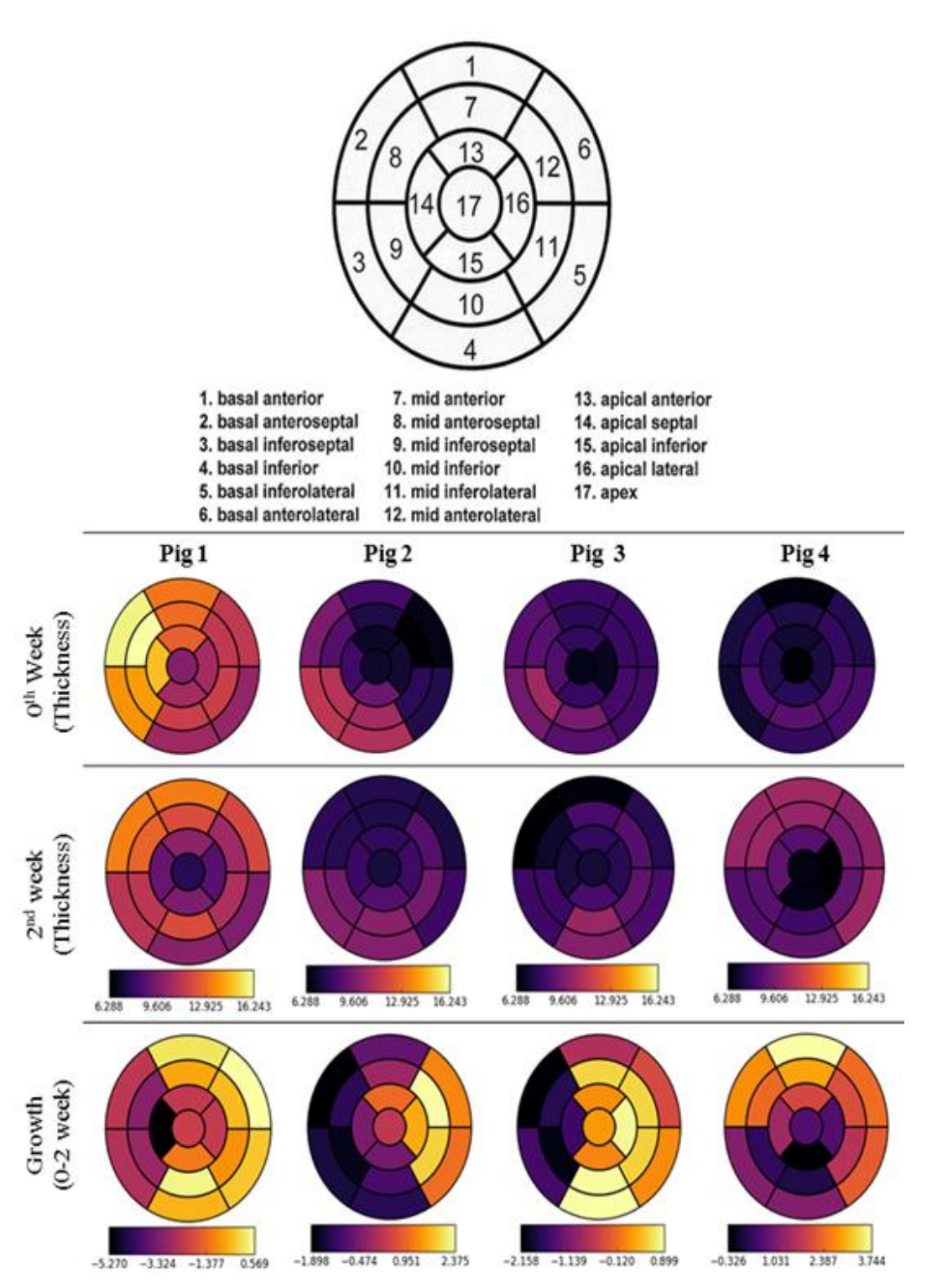


Figure 3.2: Regional measured wall thickness and growth of 4 swine models based on 17 AHA segmentation [148]. Unit in mm.

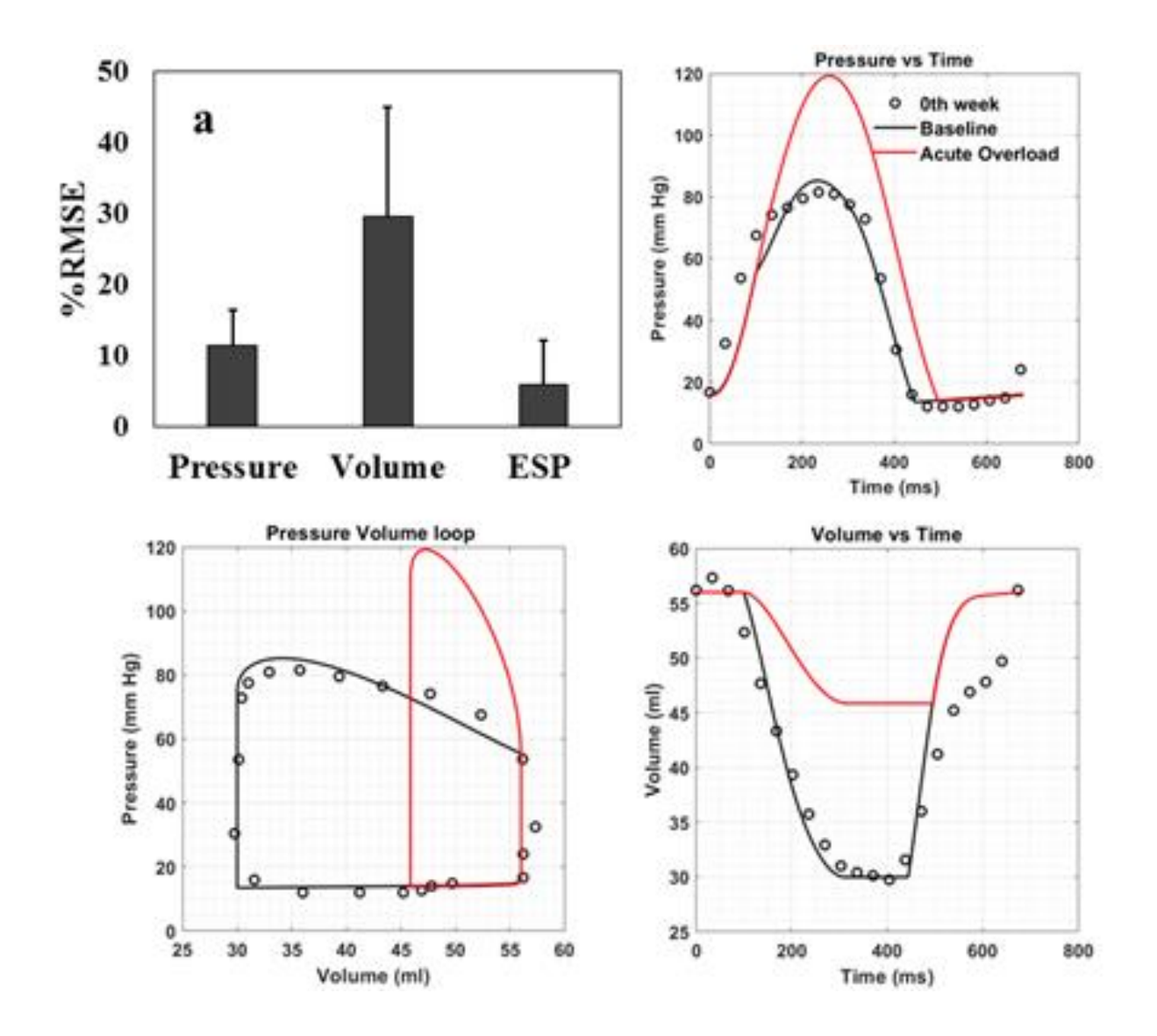


Figure 3.3: Comparison between model prediction and experimental measurements. (a) RMSE (expressed as mean \pm SD) for pressure, volume waveforms and end systolic pressure over a cardiac cycle. (b) Pressure waveforms, (c) PV loop and (d) volume waveforms from one representative animal (Swine 2). Baseline simulation case (black line); experimental measurement (black dots); acute overload simulation case (red line). Note that there are no corresponding measurements for the acute overload simulation case.

Model predictions of the baseline cases are in good agreement with the corresponding pressure and volume measurements. Specifically, the normalized root mean square error (RMSE) between model prediction and experimental measurement is $11.47 \pm 5\%$ for the pressure waveform and $29.6 \pm 15.4\%$ for the volume waveform (**Figure 3.3a**). Differences in stroke volume and EF

between the baseline model prediction and experimental measurements are 0.5% and 0.85%, respectively. Representative pressure waveform (**Figure 3.3b**), volume waveform (**Figure 3.3c**) as well as PV loop (**Figure 3.3d**) are also presented for one swine. For the acute overload LV FE models, which were calibrated to match peak systolic pressure measured at 2 weeks after aortic constriction, the RMSE between model prediction and measurements of the pressure is $6 \pm 6.1\%$.

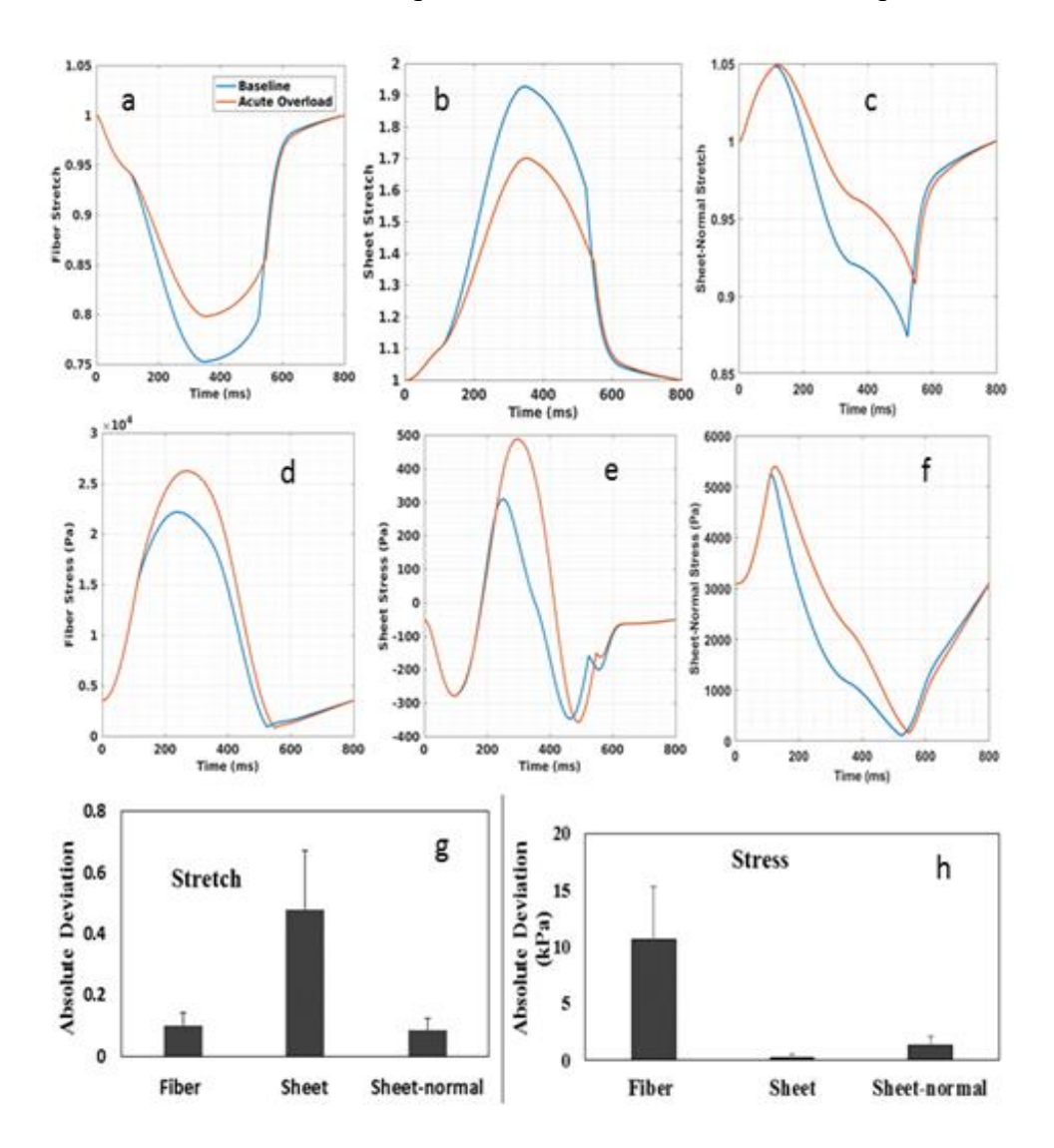


Figure 3.4: Comparison of normal stress and stretch in the myofiber, sheet and sheet-normal directions between the baseline and acute overload cases. Spatially averaged waveforms of the baseline (blue) and acute overload (red) for: (a) myofiber stretch (b) sheet stretch (c) sheet-normal stretch (d) myofiber stress (in Pa) (e) sheet stress (in Pa) and (g) sheet-normal stress (in Pa). Stretch was computed with end-diastolic configuration as reference. Average maximum absolute deviation of (g) stretch and (h) stress (in kPa) in four swines.

A comparison of the spatially averaged normal stress and stretch in the myofiber, sheet and sheet-normal directions between the baseline and acute overload cases reveals that the amount of normal stretch was reduced in all directions in the latter (**Figure 3.4a-c**). This corresponds to a reduction in ESV in the acute overload cases (**Figure 3.4c**). On the other hand, spatially averaged normal stress in all directions was increased in the acute overload cases (**Figure 3.4d-f**). Among the 3 stretch components, spatially averaged normal stretch in the sheet direction has the largest change (0.47 ± 0.194) followed by normal stretch in the myofiber (0.1 ± 0.041) and sheet-normal (0.086 ± 0.04) directions (**Figure 3.4g**) associated with acute overload. Conversely, the spatially averaged myofiber stress has the largest change $(10.66 \pm 4.68 \text{ kPa})$ associated with acute overload followed by the sheet-normal $(1.29 \pm 0.82 \text{ kPa})$ and sheet stresses $(0.48 \pm 0.2 \text{ kPa})$ (**Figure 3.4h**).

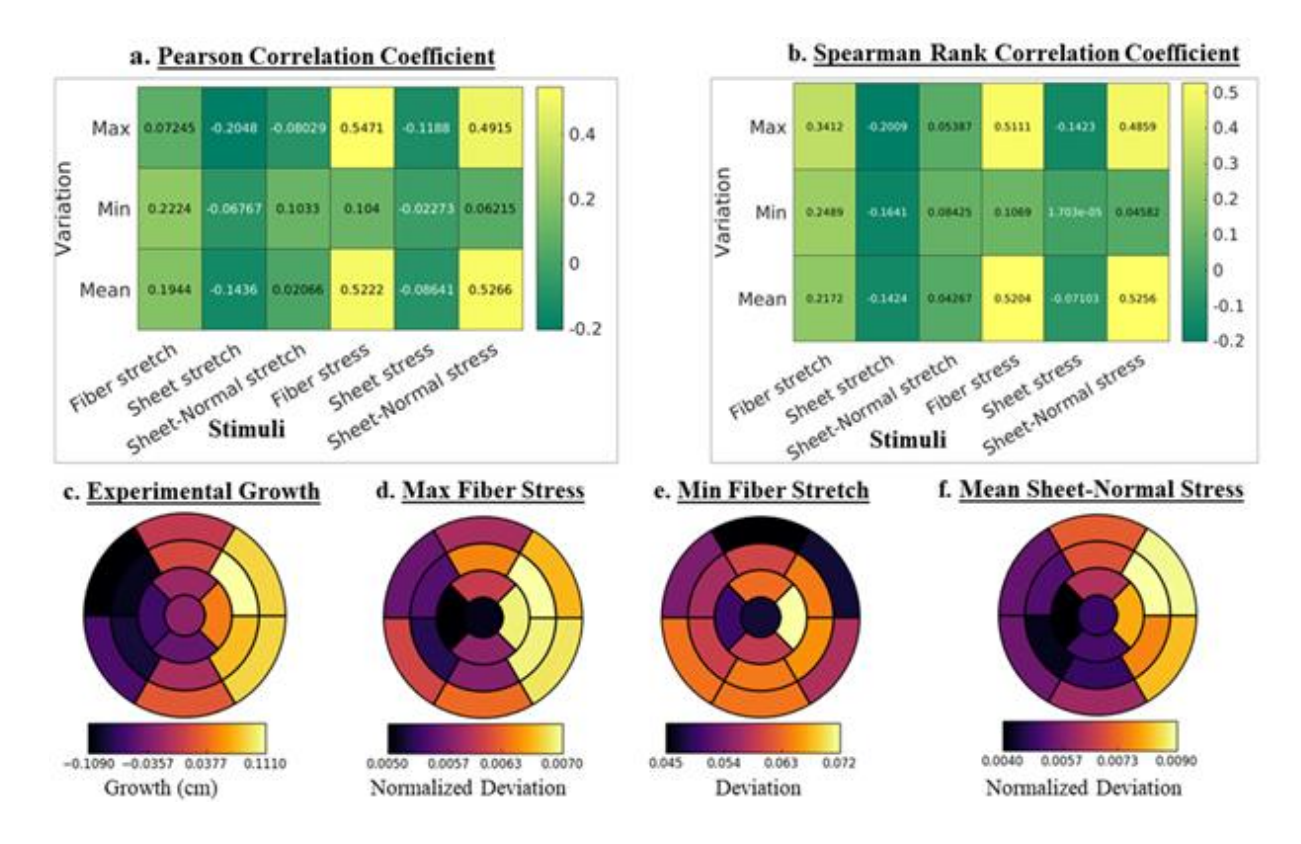


Figure 3.5: (a) Pearson correlation coefficients of growth with changes in maximum, minimum and mean stress and stretch over a cardiac cycle. (b) Regional growth measured experimentally. (c) - (e): Regional changes in maximum, minimum and mean myofiber stress, myofiber stretch and sheet-normal stress, respectively. Quantities are averaged over 4 swines.

By performing a correlation analysis of regional growth with the regional changes in mechanics of 4 aortic banding swine models, we found that the changes in maximum and mean myofiber stress exhibits the strongest (positive) correlation with growth (Figure 3.5a), where regions that has the largest (smallest) changes in maximum and mean myofiber stress correspond to regions that has the largest (smallest) increase in wall thickness (Figure 3.5b). Pearson and Spearman rank correlation coefficients were computed to quantify the degree of correlation of growth with the change in maximum, mean and minimum in the 6 mechanical quantities over a cardiac cycle (18 coefficients in total) for each swine. Averaging the coefficients over the 4 swine models reveals that the changes in maximum myofiber stress (0.5471) has the strongest correlation with growth, followed by the changes in the mean sheet-normal stress (0.5266) based on the Pearson correlation coefficient (Figure 3.5a). Based on the Spearman rank correlation coefficient, the changes in mean sheet normal stress (0.5256) and mean myofiber stress (0.5204) show the strongest correlation with growth, followed by changes in the maximum myofiber stress (0.5111) (Figure 3.5b). On the other hand, none of the stretch components has a good correlation with growth, with changes in the mean sheet-normal stretch showing the worst correlation with growth (Pearson = 0.02066, Spearman rank = 0.04267). Averaging the change in maximum myofiber stress over the 4 swine models reveals that the largest increase occurs in the LV free wall, which also shows the greatest increase in wall thickness (Figure 3.5c). These results support the "systolic stress-correction hypothesis" that had been applied in some growth constitutive model.

Scatter plots of the local changes in maximum myofiber, mean sheet-normal and mean myofiber stresses (that have the best correlation) with local growth in the LV are shown in **Figure 3.6** for a representative case. In this case, the changes in the maximum myofiber stress (Pearson: 0.5471, Spearman: 0.5111) showed the strongest correlation with growth whereas changes in the

minimum sheet-normal stretch (Pearson: 0.02066, Spearman: 0.04267) showed the worst correlation.

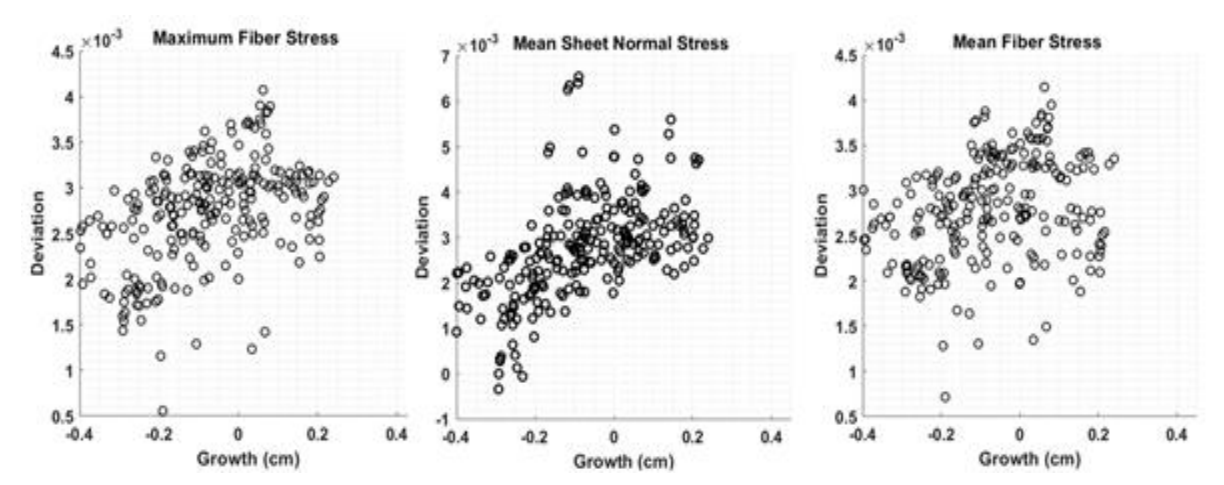


Figure 3.6: Scatter plots of the local growth with changes in stimuli in the LV of a representative case (swine 1). These three stimuli show best correlation with growth (see **Figure 3.5a**).

Interestingly, our result also shows that regional (acute) changes in myocardial stretches are not correlated with the regional changes in LV wall thickness. This is despite our findings showing that the myocardial stretches change globally in response to pressure overload in a manner that is consistent with clinical studies of aortic stenosis patients [149–151] and acute experimental studies of pressure overload in dogs [141] (where the amount of shortening in both the major and minor axes and the amount of thickening are reduced). Correspondingly, these results suggest that while using the changes in myocardial stretches as growth stimuli may be sufficient to describe changes in global features of remodeling, it may not be sufficient to reproduce regional changes in LV wall thickness associated with pressure overload.

3.4 Conclusion

Based on our study, local myofiber stress is strongly correlated local growth compared to local myofiber stretch. This result suggests that prescribing local myofiber stresses as the local stimuli in the growth constitutive law will better capture regional geometrical changes in the LV thickness

associated with pressure overload than prescribing local myofiber stretch as the local growth stimuli.

CHAPTER 4 IDEALIZED LEFT VENTRICULAR MODEL ON HYPERTROPHIC CARDIOMYOPATHY

4.1 Introduction

HCM (as discussed in Chapter 1) is characterized by myofiber disarray, fibrosis, asymmetrical hypertrophy and a reduction in both longitudinal and circumferential strains. Mathematical modeling incorporating these features can be helpful in investigating the adaptive or maladaptive changes in LV mechanics associated with this disease. Computational models based on idealized ellipsoidal geometry have been developed to investigate the effects of remodeling features in both normal and diseased LV. Specifically, Usyk et al [152] developed a mathematical model based on an idealized LV geometry to investigate the mechanism of regional dysfunction caused by myofiber dispersion in mice heart. By increasing the myofiber angular dispersion and reducing sarcomere length in their model, they showed that focal changes in the microstructural properties of the disarrayed myocardium are directly responsible for the patterns of regional dysfunction in the LV. In another study, Deng et al [153] developed an idealized LV model for healthy, subaortic obstructive and midventricular obstructive phenotypes of HCM to investigate the genesis of apical aneurysm and reported that higher myofiber stress at the apex might initiate the formation process of aneurysm. Recently, a few directions and limitations of developing multiscale models in HCM have also been reviewed by Campbell et al. [154]. None of these studies, however, have investigated the change in LV mechanics due to myofiber disarray in the HCM heart.

To address these limitations, we developed computational frameworks based on an idealized LV model to investigate the changes in ventricular mechanics associated with myofiber disarray in HCM heart. The finite element framework coupled with closed loop circulatory model was applied on two different geometry, namely normal LV and HCM LV. The strain along longitudinal and circumferential directions for normal LV without disarray were validated using

published data. To investigate the effects of myofiber disarray on LV mechanics, different degrees of myofiber disarray were applied globally (in both models) and regionally (in normal LV model).

4.2 Methods

4.2.1 Geometry reconstruction

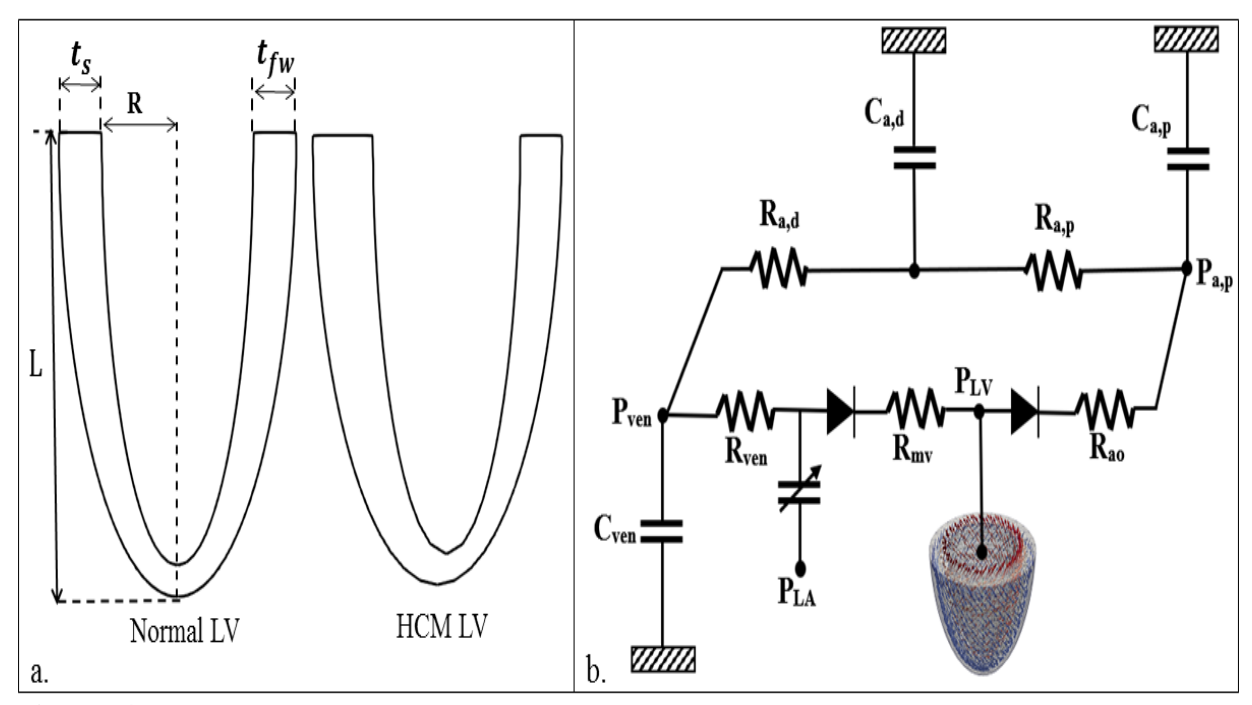


Figure 4.1: Construction of LV FE model. (a) Variation in septum (t_s) and LVFW (t_{fw}) thickness on Baseline and HCM model. Here R and L are the inner radius along short axis and outer radius along long axis, respectively, of the ellipsoid. (b) Schematic representation of LV mesh coupled with closed loop Windkessel model.

An idealized half prolate geometry was used to represent a normal and HCM LV. The normal LV has a wall thickness that is axisymmetric whereas the HCM LV has a wall thickness that is asymmetrical about the long axis (**Figure 4.1a**). Geometrical parameters were prescribed based on clinical measurements. The ratio of septum vs. LVFW thickness for HCM model was prescribed to be 1.63, which is within the range found in Tanaka et al [155]. The geometries were discretized with 4353 quadratic tetrahedral elements. Mean myofiber direction was prescribed based on a linear transmural variation of the helix angle from +60° at the endocardium to -60° at

the epicardium across the LV wall using a Laplace-Dirichlet rule-based algorithm.

4.2.2 Incorporation of myofiber disarray

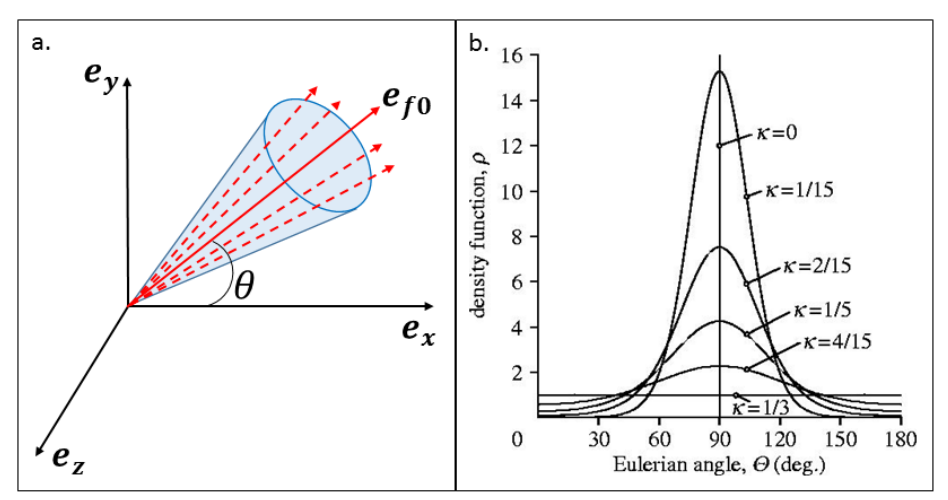


Figure 4.2: (a) Myofiber dispersion following a probability distribution density function. Solid red arrow represents the initial myofiber direction, where dashed line represents one of many possible orientations of respective myofiber. (b) The two dimensional representation of distribution density function for varying angle (θ) and disarray (κ). Figure (b) is adapted from Gasser et al [156].

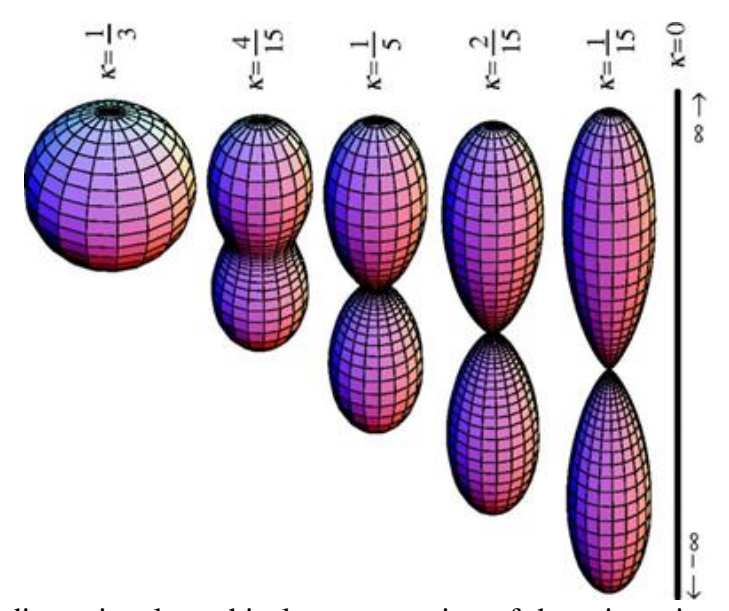


Figure 4.3: Three-dimensional graphical representation of the orientation for the fibers based on transversely isotropic density function. The figure is adapted from Gasser et al [156].

Based on the assumption of axisymmetric fiber distribution, myofiber disarray was incorporated through a structure tensor \boldsymbol{H} [156] describing a conical dispersion of myofibers about

a mean myofiber direction, e_{f0} . The structure tensor is given by

$$H = \kappa I + (1 - 3\kappa)e_{f0} \otimes e_{f0}, \tag{4.1}$$

where I is the identity tensor and κ represents the fiber distribution in an integral sense that is defined as,

$$\kappa = \frac{1}{4} \int_0^{\pi} \rho(\theta) \sin^3 \theta d\theta. \tag{4.2}$$

Here, $\rho(\theta)$ is the probability density function representing the fiber dispersion. At the lower limit of the disarray parameter ($\kappa = 0$), myofibers are perfectly aligned along the e_{f0} direction (i.e., the structure tensor reduces to $e_{f0} \otimes e_{f0}$). At the upper limit of the disarray parameter ($\kappa = 1/3$), the structure tensor reduces to I, representing a distribution of myofibers that produces an isotropic material response (i.e., a complete myofiber disarray). Hence, the structure tensor, H, depends on a single dispersion parameter, κ , which represents the fiber distribution in an integral sense and describes its "degree of anisotropy". The von-mises distribution is depicted in **Figure 4.2** for different degree of κ varying between 0 to 1/3. The distribution changes from a bone like structure when $\kappa = 0$ to a sphere in three dimension when $\kappa = 1/3$ is graphically (**Figure 4.3**).

4.2.3 Constitutive law for LV model

An active stress formulation was used to describe the mechanical behavior of the ventricular geometry in the cardiac cycle. In this formulation, the stress tensor S can be decomposed additively into a passive component S_p and an active component S_a (i.e., $S = S_a + S_p$). The passive stress tensor was defined based on the strain energy function of a Fung-type transversely-isotropic hyperelastic material [157],

$$W = \frac{1}{2}C(e^{Q} - 1), \tag{4.3a}$$

where

$$Q = b_{ff}E_{ff}^2 + b_{xx}(E_{ss}^2 + E_{nn}^2 + E_{sn}^2 + E_{ns}^2) + b_{fx}(E_{fn}^2 + E_{nf}^2 + E_{fs}^2 + E_{sf}^2).$$
(4.3b)

In Eq. (4.3b), E_{ij} with $(i, j) \in (f, s, n)$ are components of the Green-Lagrange strain tensor with f, s, n denoting the myocardial fiber, sheet and sheet normal directions, respectively. Material parameters of the passive constitutive model are denoted by C, b_{ff} , b_{xx} and b_{fx} .

Based on a previously developed active contraction model [139, 158, 159], the active stress (S_a) directed in the local myofiber direction was calculated as

$$\mathbf{S}_{a} = T_{max} \left(\frac{Ca_{0}^{2}}{Ca_{0}^{2} + ECa_{50}^{2}} \right) C_{t} \mathbf{H} , \qquad (4.4a)$$

In the above equation, T_{max} is the isometric tension achieved at the longest sarcomere length and Ca_0 denotes the peak intracellular calcium concentration. The length dependent calcium sensitivity ECa_{50} and the variable C_t are given by,

$$ECa_{50} = \frac{(Ca_0)_{max}}{\sqrt{\exp(B(l-l_0)) - 1}},$$
(4.4b)

$$C_{t} = \begin{cases} \frac{1}{2} \left(1 - \cos\left(\frac{\pi t}{t_{0}}\right) \right); & 0 \le t < t_{r} \\ \frac{1}{2} \left(1 - \cos\left(\frac{\pi t_{r}}{t_{0}}\right) \right) e^{-(t-t_{r})/\tau}; & t \ge t_{r} \end{cases}$$

$$(4.4c)$$

In Eq. (4.4b), B is a constant, $(Ca_0)_{max}$ is the maximum peak intracellular calcium concentration and l_0 is the sarcomere length at which no active tension develops. In Eq. (4.4c), t_0 , t_r and τ are the time taken to reach peak tension, the duration of relaxation and the relaxation time constant, respectively. The sarcomere length l is calculated from the myofiber stretch λ_{LV} by

$$\lambda_{LV} = \sqrt{tr(\mathbf{HC})}, \tag{4.5a}$$

$$l = \lambda_{IV} l_r \,. \tag{4.5b}$$

In Eq. (4.5), $\mathbf{C} = \mathbf{F}^T \mathbf{F}$ is the right Cauchy-Green deformation tensor and l_r is the relaxed sarcomere length.

4.2.4 Closed-loop circulatory model

The LV FE model was coupled to a closed-loop lumped parameter modeling framework that describes the circulatory system (**Figure 4.1b**). The ventricular model consists of five compartments (namely LA, LV, venous, peripheral, and distal artery) yielding five volume states $(V_{LA}, V_{LV}, V_{ven}, V_{a,p}, V_{a,d})$. Based on mass conservation, the rate of volume change in each storage compartment of the circulatory system depends on the variation in flow rates, both in and out, $(q_{mv}, q_{ao}, q_{a,p}, q_{a,d}, q_{ven})$ at different segments,

$$\frac{dV_{LA}(t)}{dt} = q_{ven}(t) - q_{mv}(t),\tag{4.6a}$$

$$\frac{dV_{LV}(t)}{dt} = q_{mv}(t) - q_{ao}(t), \tag{4.6b}$$

$$\frac{dV_{a,p}(t)}{dt} = q_{ao}(t) - q_{a,p}(t), \tag{4.6c}$$

$$\frac{dV_{a,d}(t)}{dt} = q_{a,p}(t) - q_{a,d}(t), \tag{4.6d}$$

$$\frac{dV_{ven}(t)}{dt} = q_{a,d}(t) - q_{ven}(t), \tag{4.6e}$$

Flowrate at different segments of the circulatory model depends on their resistance to flow $(R_{mv}, R_{ao}, R_{a,p}, R_{a,d}, R_{ven})$ and the pressure difference between the connecting storage compartments (i.e., pressure gradient). The flow rates are given by,

$$q_{ao}(t) = \begin{cases} \frac{P_{LV}(t) - P_{ao}(t)}{R_{ao}}; & if P_{LV} > P_{ao}, \\ 0; & if P_{LV} < P_{ao} \end{cases}$$
(4.7a)

$$q_{a,p}(t) = \frac{P_{ao}(t) - P_{a,d}(t)}{R_{a,p}},$$
 (4.7b)

$$q_{a,d}(t) = \frac{P_{a,d}(t) - P_{ven}(t)}{R_{a,d}},$$
(4.7c)

$$q_{ven}(t) = \frac{P_{ven}(t) - P_{LA}(t)}{R_{ven}},$$
 (4.7d)

$$q_{mv}(t) = \begin{cases} \frac{P_{LA}(t) - P_{LV}(t)}{R_{mv}}; & if P_{LA} > P_{LV} \\ 0; & if P_{LA} < P_{LV} \end{cases}$$
(4.7e)

A time varying elastance function was used to describe the contraction of LA [131]. Specifically, pressure in the LA $P_{LA}(t)$ was prescribed to be a function of its volume $V_{LA}(t)$ by the following equations that describe its contraction using a time-varying elastance function e(t):

$$P_{LA}(t) = e(t)P_{es,LA}(V_{LA}(t)) + (1 - e(t))P_{ed,LA}(V_{LA}(t)),$$

$$P_{es,LA}(V_{LA}(t)) = E_{es,LA}(V_{LA}(t) - V_{0,LA}),$$
(4.8a)
(4.8b)

$$P_{es,LA}(V_{LA}(t)) = E_{es,LA}(V_{LA}(t) - V_{0,LA}), \tag{4.8b}$$

$$P_{ed,LA}(V_{LA}(t)) = A_{LA}(e^{B_{LA}(V_{LA}(t) - V_{0,LA})} - 1), \tag{4.8c}$$

$$e(t) = \begin{cases} \frac{1}{2} \left(sin\left[\left(\frac{\pi}{t_{max}} \right) t - \frac{\pi}{2} \right] + 1 \right); 0 < t \le \frac{3}{2} t_{max} \\ \frac{1}{2} e^{-\left(t - \frac{3}{2} t_{max} \right) / \tau}; \qquad t > \frac{3}{2} t_{max} \end{cases}$$
(4.8d)

In Eq. (4.8a-d), $E_{es,LA}$ is the end-systolic elastance of the LA, $V_{0,LA}$ is the volume-intercept of the end-systolic pressure volume relationship (ESPVR), and both A_{LA} and B_{LA} are parameters of the end-diastolic pressure volume relationship (EDPVR) of the LA. The driving function e(t)is given in Eq. (4.8d) in which t_{max} is the point of maximal chamber elastance and τ is the time constant of relaxation.

Pressure in each vessel (arteries and veins) in both systemic and pulmonary circulation was calculated by a simplified pressure volume relationship

$$P_{ven}(t) = \frac{V_{ven}(t) - V_{ven,0}}{C_{ven}},$$
(4.9a)

$$P_{a,p}(t) = \frac{V_{a,p}(t) - V_{ap,0}}{C_{a,p}},\tag{4.9b}$$

$$P_{a,d}(t) = \frac{V_{a,d}(t) - V_{ad,0}}{C_{a,d}},$$
(4.9c)

where, $V_{ven,0}$, $V_{ad,0}$ are constants representing the resting volumes and C_{ven} , $C_{a,p}$, $C_{a,d}$ are the total compliance of the veins, proximal and distal arteries, respectively. Finally, pressure in the LV depends on their corresponding volume through a non-closed form function,

$$P_{LV,cav}(t) = f^{FE}(V_{LV}(t)). \tag{4.10}$$

The functional relationship between pressure and volume in the LV was obtained using the FE method as described in the next section.

4.2.5 Ventricular FE model

The Lagrangian functional for the left ventricular FE formulation is given by,

$$\mathcal{L}(\boldsymbol{u}, p, P_{LV}, \boldsymbol{c}_{1}, \boldsymbol{c}_{2}) \\
= \int_{\Omega_{0}} W(\boldsymbol{u}) dV - \int_{\Omega_{0}} p(J-1) dV \\
- P_{LV} (V_{LV,cav}(\boldsymbol{u}) - V_{LV}) - \boldsymbol{c}_{1} \cdot \int_{\Omega_{0}} \boldsymbol{u} dV \\
- \boldsymbol{c}_{2} \cdot \int_{\Omega} \boldsymbol{x} \times \boldsymbol{u} dV,$$
(4.11)

In the above equation, u is the displacement field, p is a Lagrange multiplier to enforce incompressibility of the tissue (i.e., Jacobian of the deformation gradient tensor, J=1), P_{LV} is the Lagrange multiplier to constrain the LV cavity volume $V_{LV,\text{cav}}(u)$ to a prescribed value V_{LV} [160], and both c_1 and c_2 are Lagrange multipliers to constrain rigid body translation (i.e., zero mean translation) and rotation (i.e., zero mean rotation) [161]. The functional relationship between the cavity volumes of the LV and RV to the displacement field is given by,

$$V_{LV,\text{cav}}(\boldsymbol{u}) = \int_{\Omega_{k,inner}} dv = -\frac{1}{3} \int_{\Gamma_{k,inner}} \boldsymbol{x}.\,\boldsymbol{n}\,da\,, \tag{4.12}$$

where $\Omega_{k,inner}$ is the volume enclosed by the inner surface $\Gamma_{k,inner}$ and the basal surface at z=0, and \boldsymbol{n} is the outward unit normal vector. The first variation of the Lagrangian functional in Eq. (4.11) leads to the following expression:

$$\delta \mathcal{L}(\boldsymbol{u}, p, P_{LV}, P_{RV}, \boldsymbol{c}_{1}, \boldsymbol{c}_{2}) = \int_{\Omega_{0}} (\boldsymbol{P} - p\boldsymbol{F}^{-T}) : \nabla \delta \boldsymbol{u} \, dV -$$

$$\int_{\Omega_{0}} \delta p(J - 1) \, dV - P_{LV, \text{cav}} \int_{\Omega_{0}} cof(\boldsymbol{F}) : \nabla \delta \boldsymbol{u} \, dV -$$

$$\delta P_{LV, \text{cav}} (V_{LV, \text{cav}}(\boldsymbol{u}) - V_{LV}) - \delta \boldsymbol{c}_{1} \cdot \int_{\Omega_{0}} \boldsymbol{u} \, dV -$$

$$\delta \boldsymbol{c}_{2} \cdot \int_{\Omega_{0}} \boldsymbol{X} \times \boldsymbol{u} \, dV - \boldsymbol{c}_{1} \cdot \int_{\Omega_{0}} \delta \boldsymbol{u} \, dV -$$

$$\boldsymbol{c}_{2} \cdot \int_{\Omega_{0}} \boldsymbol{X} \times \delta \boldsymbol{u} \, dV,$$

$$(4.13)$$

In Eq. (4.13), P is the first Piola Kirchhoff stress tensor, F is the deformation gradient tensor, δu , δp , $\delta P_{LV,\text{cav}}$, δc_1 , δc_2 are the variation of the displacement field, Lagrange multipliers for enforcing incompressibility and volume constraint, zero mean translation and rotation, respectively. The Euler-Lagrange problem then becomes finding $u \in H^1(\Omega_0)$, $p \in L^2(\Omega_0)$, $P_{LV,\text{cav}} \in \mathbb{R}$, $c_1 \in \mathbb{R}^3$, $c_2 \in \mathbb{R}^3$ that satisfies,

$$\delta \mathcal{L}(\boldsymbol{u}, p, P_{LV, \text{cav}}, \boldsymbol{c}_{1,}, \boldsymbol{c}_{2}) = 0, \qquad (4.14)$$

and $\boldsymbol{u}.\boldsymbol{n}|_{base}=0$ (for constraining the basal deformation to be in-plane) $\forall \, \delta \boldsymbol{u} \in H^1(\Omega_0), \delta p \in L^2(\Omega_0), \delta P_{LV,cav} \in \mathbb{R}, \delta \boldsymbol{c}_1 \in \mathbb{R}^3, \delta \boldsymbol{c}_2 \in \mathbb{R}^3.$

An explicit time integration scheme was used to solve the five ODEs in Eq. (4.6). The compartment volumes (V_{LA} , V_{LV} , $V_{a,p}$, $V_{a,d}$, V_{ven}) at each timestep t_i were determined from their respective values and the segmental flow rates (q_{mv} , q_{ao} , $q_{a,p}$, $q_{a,d}$, q_{ven}) were determined using Eq. (4.7) at previous timestep t_{i-1} . The computed compartment volumes at t_i were used to update the corresponding pressures (P_{LA} , P_{LV} , $P_{a,p}$, $P_{a,d}$, P_{ven}). Pressures in LA (P_{LA}) and vessels ($P_{a,p}$, $P_{a,d}$, P_{ven}) were computed from Eq. (4.8a) and (4.9a-c), respectively. On the other hand,

pressures in the LV $(P_{LV,cav})$ was computed from the FE solutions of Eq. (4.10) with the volumes (V_{LV}) at timestep t_i as input. We note here that $(P_{LV,cav})$ are scalar Lagrange multipliers in the FE formulation for constraining the cavity volumes to the prescribed values (V_{LV}, V_{art}) . The computed pressures at timestep t_i were then used to update the segmental flow rates in Eq. (4.7) that will be used to compute the compartment volumes at timestep t_{i+1} in the next iteration.

4.2.6 Model parameterization

Parameters of LV FE model associated with the normal geometry without disarray was manually adjusted so that its predictions agree well with the previously reported clinical studies (**Figure 4.4**). The predicted longitudinal strain showed a good match with the clinical data (Root mean squared error (RMSE) ~25% compared with Gorcsan et al [162], ~21% compared with Smiseth et al. [103]). The circumferential strain also shows a good match with the clinical data [162, 163]. To calibrate the model, preload was adjusted by changing the venous return ($V_{ven,0}$) in the model, whereas the afterload was adjusted by changing the peripheral resistance ($R_{a,p}$). The same parameters were used in subsequent simulations using the normal and HCM LV ellipsoidal geometries, where the disarray index (κ) was varied from 0 to 1/3 in both cases. Later the LV model was segmented into 4 sections and the disarray parameter was varied regionally between the septum and LVFW. Specifically, the simulation cases are:

- *Normal LV*: Uniform wall thickness of 1.13 cm with κ varying from 0 to 1/3 globally.
- *HCM LV*: Septal thickness (1.63 cm) is higher than LVFW (1.13 cm) with κ varying from 0 to 1/3 globally.
- Normal LV with regional myofiber disarray: Uniform wall thickness of 1.13 cm with κ varying from 0 to 1/3 regionally in the septum and $\kappa = 0$ in the LVFW.

For each case, the simulation was performed over several cardiac cycles at a heart rate of 75bpm

until the pressure-volume loop reached a steady state.

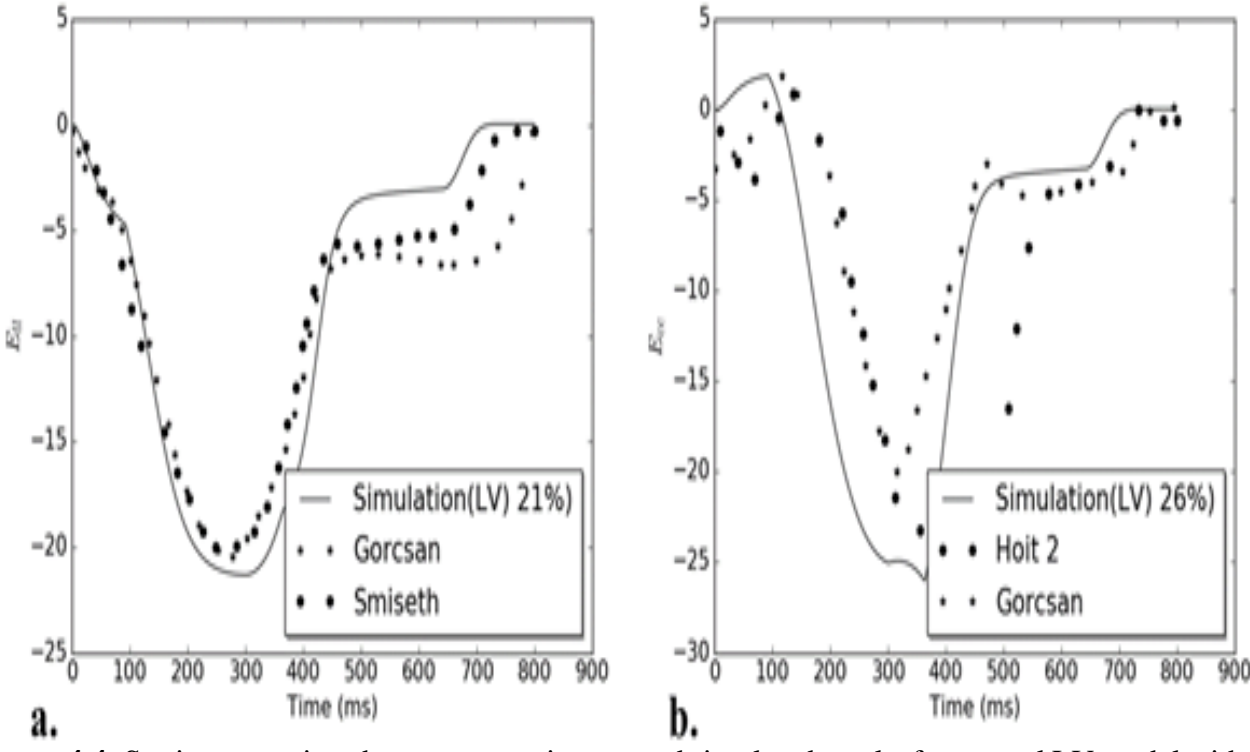


Figure 4.4: Strain comparison between experiments and simulated results for normal LV model without disarray. (a) Longitudinal strain, (b) Circumferential strain for $\kappa = 0$.

4.3 Results

4.3.1 Pressure-volume loop

The steady state pressure-volume loops of the LV for *normal LV* and *HCM LV* cases were obtained from the FE model (**Figure 4.5 c, f**). Hemodynamics of the LV was greatly altered with increasing myofiber disarray with increasing κ (from 0 to 1/3). In the *normal LV* case, a significant reduction in peak systolic pressure (~55% decrease), stroke volume (~65% decrease) and EF (~68% decrease) were observed in the results for complete myofiber disarray compared to the case without myofiber disarray. Similar trend was also observed in the *HCM LV* case.

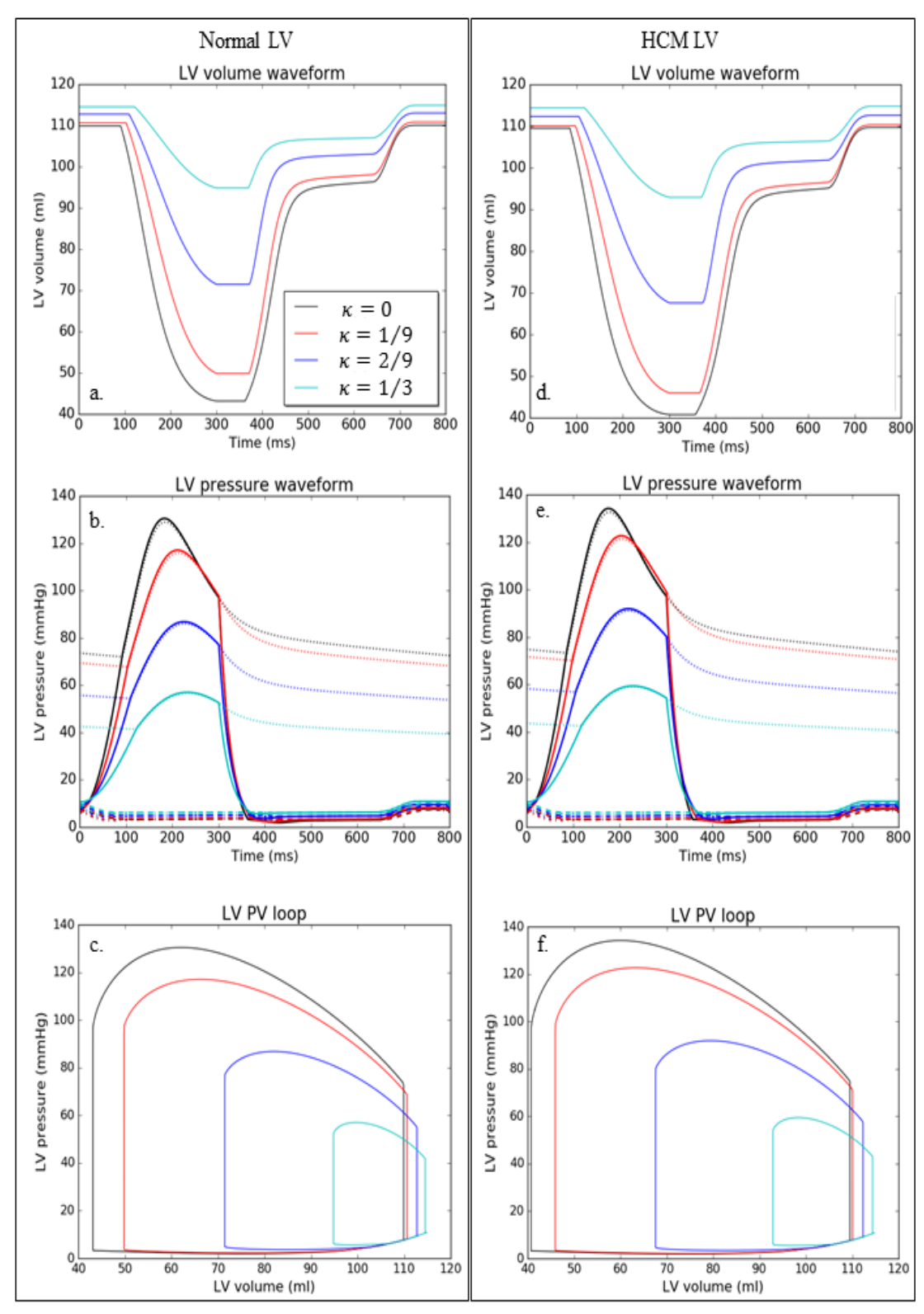


Figure 4.5: Volume-time plot (a,d), pressure-time plot(b,e), PV loop (c,f). The top and bottom row denoted normal LV geometry and HCM LV geometry, respectively.

4.3.2 Myocardial strains

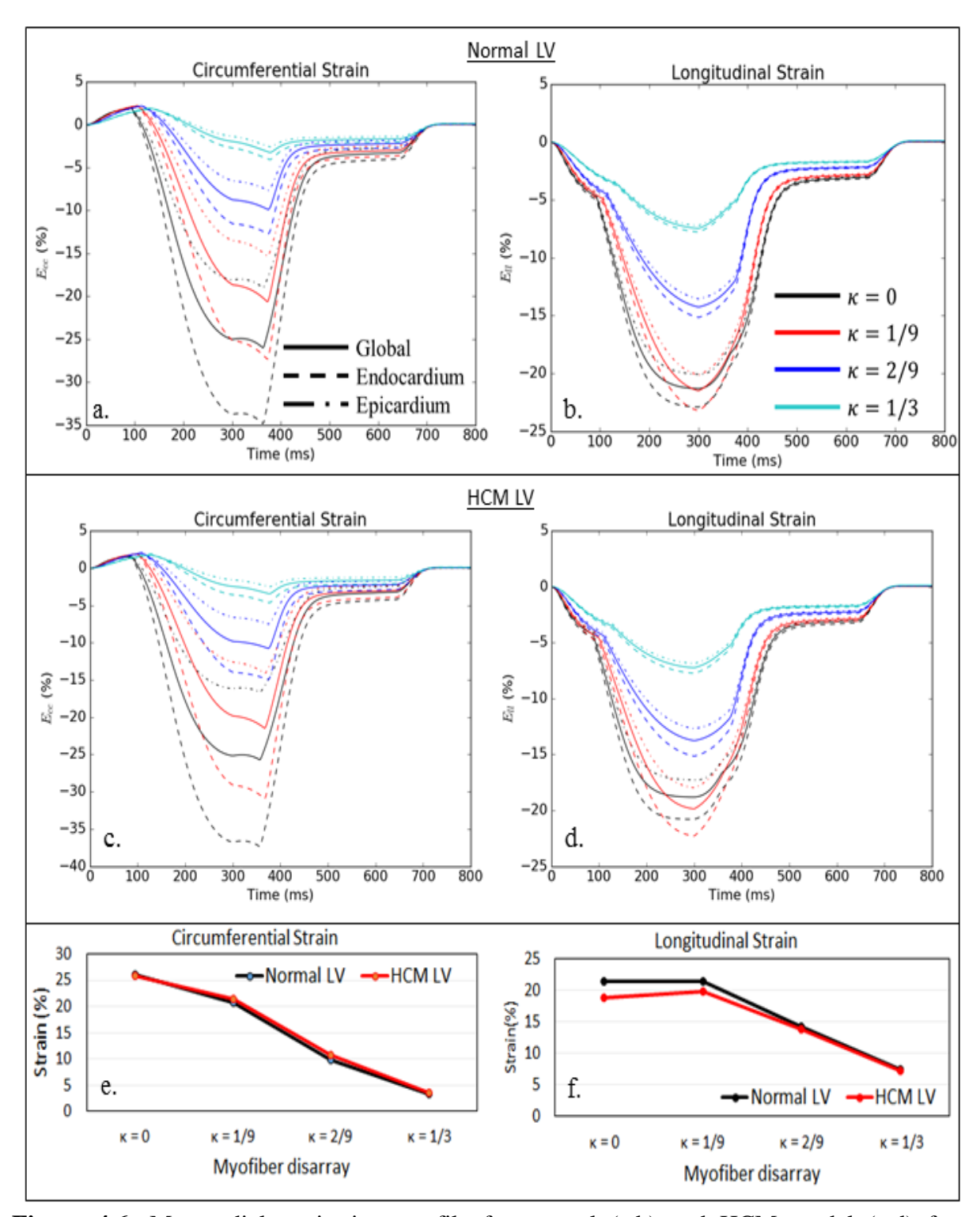


Figure 4.6: Myocardial strain-time profile for normal (a,b) and HCM model (c,d) from endocardium to epicardium. (e, f) Peak global strain comparison with varying disarray parameter. The global strain results are shown with solid lines.

Myocardial strains at the endocardium and epicardium over a cardiac cycle with varying myofiber disarray for both normal LV and HCM LV cases are shown in Figure 4.6 a-d. With an increase in myofiber disarray, the strain is reduced significantly in both cases. With the increase in κ from 0 to $\frac{1}{3}$, the reduction in global peak circumferential strain between endocardium and epicardium was significant in both cases (~15.8% when $\kappa = 0$ vs. ~1.6% when $\kappa = \frac{1}{3}$ in the *normal* LV case; ~20.75% when $\kappa = 0$ vs. ~2.2% when $\kappa = \frac{1}{3}$ in the HCM LV case). Also, the reduction in peak longitudinal strain between the endocardium and epicardium was similar (~2.8% when $\kappa = 0$ vs. ~0.5% when $\kappa = \frac{1}{3}$ in the *normal LV* case; ~3.5% when $\kappa = 0$ vs. ~1% when $\kappa = \frac{1}{3}$ in the HCM LV case). The average circumferential and longitudinal strain in both the normal LV and HCM LV cases (shown by the solid line in the strain profile) were reduced with an increase in κ from 0 to $\frac{1}{3}$. Although the peak longitudinal strain was higher in the normal LV case compared to the HCM LV case (~21% at normal vs ~18.8% at HCM) at $\kappa = 0$, the difference was mostly diminished with complete myofiber disarray. This lower value of longitudinal strain in the HCM LV case when $\kappa = 0$ could be due the increase in septum thickness of the HCM LV geometry. While peak circumferential strain is reduced with increasing myofiber disarray, it did not show any substantial difference between the *normal LV* and *HCM LV* cases.

Regional strain variation over the cardiac cycle for both *normal LV* and *HCM LV* cases is shown in **Figure 4.7**. While there was no significant variation in strain distribution between the septum and LVFW with myofiber disarray in the *normal LV* case, a slight decrease in peak strain at the septum (compared to LVFW) was observed in the *HCM LV* case. This decrease could be due to the increase in thickness at the septum in the LV geometry of the *HCM LV* case. At $\kappa = 0$ and 1/9, a slight reduction in peak circumferential and longitudinal strains at the thicker septum

region in the $HCM\ LV$ case was also found compared to the thinner LVFW region. This difference was diminished at higher value of κ .

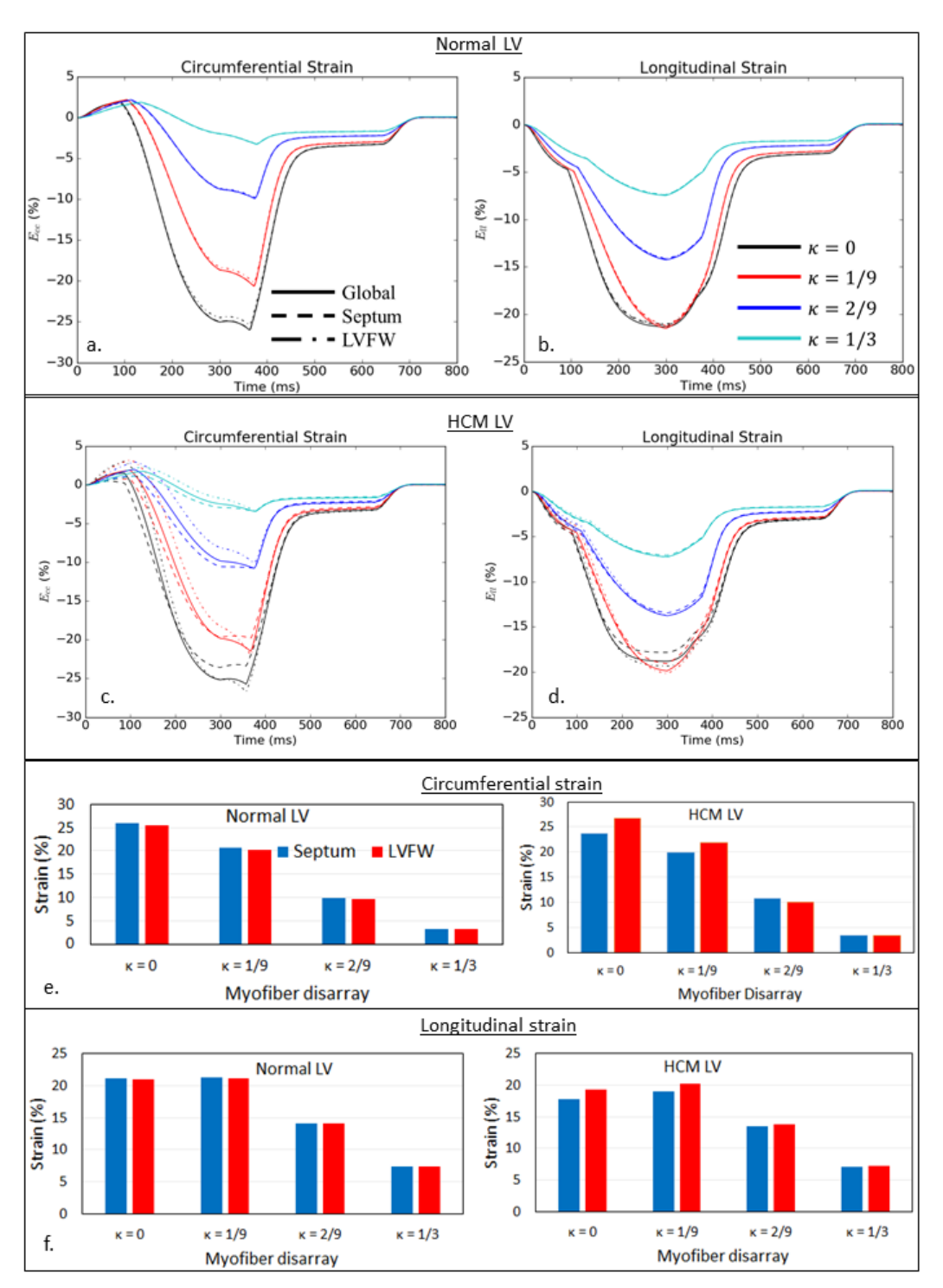


Figure 4.7: Myocardial strain-time profile for normal (a,b) and HCM model (c,d) from septum to LVFW. (e, f) Regional peak strain comparison with varying disarray parameter. The global strain results are shown with solid lines.

4.3.3 Spatial variation of myofiber disarray

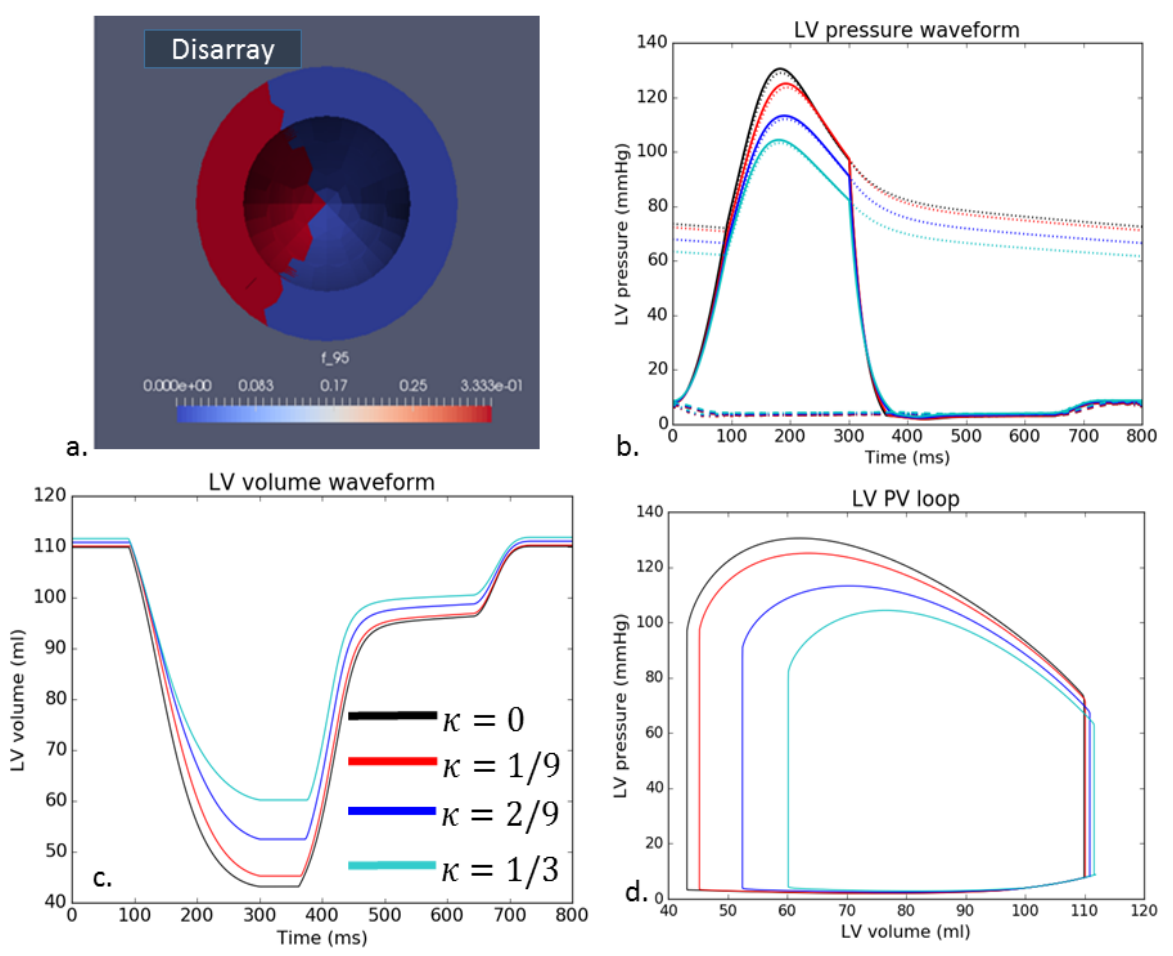


Figure 4.8: Results of variation of myofiber disarray in septum. Segmentation of LV (a-left) and distribution of disarray parameter of 1/3 at septum and 0 at rest of LV (a-right). pressure-time plot(b), Volume-time plot (c), PV loop (d) of Normal LV model. The value of disarray parameter was increased from 0 to 1/3 at septum while kept 0 at other regions.

The disarray parameter κ was distributed regionally and was prescribed different values at the septum and LVFW (**Figure 4.8**). The value of $\kappa = 0$ was kept constant at the rest of the LV while at septum region, κ was varied from 0 to 1/3. With the increase of κ , the performance of LV was reduced, although not as significantly as seen previously in **Figure 4.5**, when κ was varied globally. With increasing κ from 0 to 1/3 at septum region, the peak pressure (~22% reduction), stroke volume (~26% reduction) and EF (~27% reduction) were all reduced with complete myofiber disarray at the septum compared to without disarray.

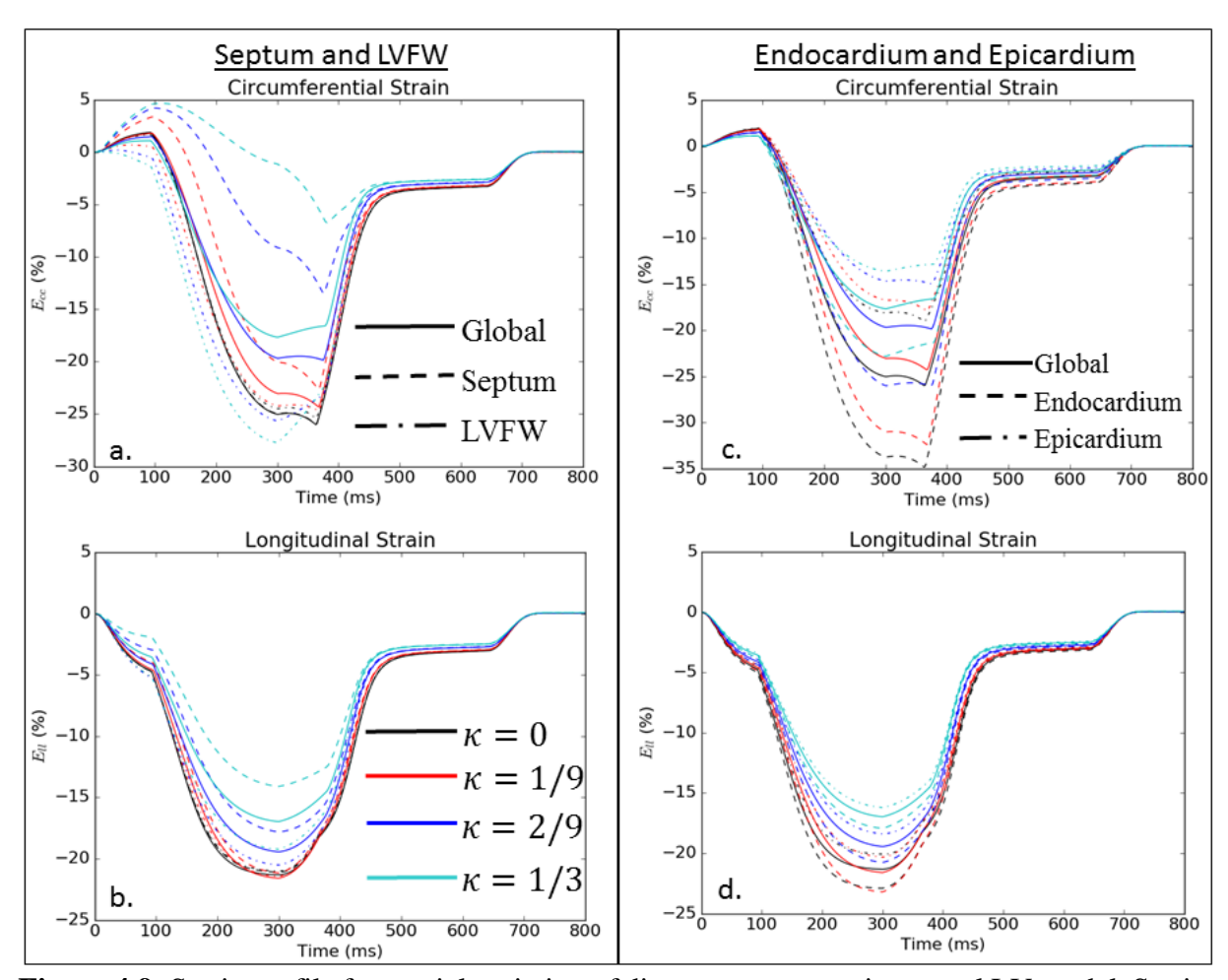


Figure 4.9: Strain profile for spatial variation of disarray parameter in normal LV model. Strain distribution from septum to LVFW: Circumferential strain (a), Longitudinal strain(b). Strain distribution from endocardium to epicardium: Circumferential strain (c), Longitudinal strain(d).

The strain distribution over a cardiac cycle with varying degree of myofiber disarray is shown in **Figure 4.9**. With an increase in septal myofiber disarray, a reduction in peak global circumferential (~26% when $\kappa = 0$ vs. ~17.7% when $= \frac{1}{3}$) and longitudinal (~21% when $\kappa = 0$ vs. ~17% when $\kappa = \frac{1}{3}$) strains was found. Myocardial strains in the septum region were also reduced in the circumferential (~26% when $\kappa = 0$ vs. ~6.7% when $= \frac{1}{3}$) and longitudinal (~21% when = 0 vs. ~14.1% when = 0 vs. ~14.1% when = 0 vs. ~14.1% when = 0 vs. ~19% lightly reduced (~21% when = 0 vs. ~19%

when $=\frac{1}{3}$), whereas circumferential strain, was slightly increased (~25.4% when $\kappa=0$ vs. ~27.7% when $\kappa=\frac{1}{3}$) with increasing septal myofiber disarray. A pre-systolic strain up to ~5% (i.e., positive strain values at the onset of contraction) was also observed at the septum with increasing septal myofiber disarray. Both circumferential and longitudinal strains were also reduced at the endocardium and epicardium with the increase in septal disarray.

4.4 Discussion

We developed an LV model based on an idealized ellipsoidal geometry with different septum wall thickness based on those published in the literature to investigate the effects of global and regional myofiber disarray. The model showed that with increasing disarray, LV mechanics gets impaired. More specifically, our results showing reduced circumferential and longitudinal strains with increasing disarray both globally and regionally at septum are consistent with the clinical results (Section 1.4.3). The pump function also reduced as the ejection fraction and SV decreased with increasing disarray.

The ratio of septum wall thickness to the LVFW wall thickness in our HCM model was 1.6, which is over the threshold (≥ 1.3) prescribed in other studies [109]. The LV function represented by stroke volume, ejection fraction and peak systolic pressure was impaired with increasing disarray in both models. Besides, the reduction in global longitudinal strain and circumferential strain are consistent with previous studies [90–92, 100, 107]. The increased wall thickness at the septum also led to a reduction in longitudinal and circumferential strains (without the presence of myofiber disarray) in the HCMLV case compared to $normal\,LV$ case (**Figure 4.7e**, **f**) suggesting that the heterogeneity in LV wall thickness induced by hypertrophy (observed clinically) are affecting the reduction in wall strain. At higher degree of disarray, however, there is no difference in strain between septum and LVFW. One reason could be the consideration of the

extreme disarray ($\kappa = \frac{1}{3}$), representing the fractional anisotropy value of 0 (**Figure 5.2**), might not be clinically feasible. Even if it is feasible, the associated G&R induced by the disarray is not simulated here. Also, LV function and mechanics was impaired globally by regional variation of disarray in *normal LV* case. Specifically, increase of regional septum strain, the strain was reduced more along septum than LVFW, suggesting the effect of heterogeneous disarray will impact differently on both global and local mechanics.

The limitations and future scope related to idealized HCM model will be described in **Chapter 6**.

4.5 Conclusion

Based on published thickness data for HCM patients, we developed a FE modeling framework to investigate the changes in global and regional mechanics due to different degree of myofiber disarray based on an idealized LV geometry. The results showed that both LV function and mechanics are impaired with increasing disarray, which are consistent with the clinical results. Further development of a patient specific model will help further investigate the intricate mechanism associated with development and progression of HCM.

CHAPTER 5 PATIENT SPECIFIC LEFT VENTRICULAR MODEL ON HYPERTROPHIC CARDIOMYOPATHY

5.1 Introduction

Myocardial fiber disarray is a histopathological hallmark in both obstructive and nonobstructive HCM [164]. The disarray of myofibers is either confined to some particular region in
the LV or is distributed throughout the entire LV. In obstructive HCM patients, a pressure gradient
> 50mm Hg across the LV outflow tract, either at resting or provoked condition, is also present
[165, 166]. Besides myofiber disarray, HCM is also associated with other key histopathological
features such as asymmetrical septal hypertrophy in the LV, changes in the myocardial contractility,
and cardiac fibrosis [81–89]. These features have been associated with changes in the LV function
seen in HCM patients, such as a reduction in (global and segmental) longitudinal and
circumferential strains [63, 90–92], active tension [167], an increase in relative ATP consumption
during tension generation [93], and a reduction in myocardial work (pressure-strain loop area)
[94].

Given the multiple histopathological features present in HCM patients, how each of these features contributes to the changes in the LV function is not clear. Although clinical studies can help reveal abnormalities of myocardial structure (e.g., myofiber disarray) associated with HCM [99], the causal link of these features to LV function is difficult to ascertain from these studies. As such, the relative contribution of these remodeling features (i.e., asymmetrical hypertrophy, myofiber disarray) to the impairment of LV function in HCM patients remains unclear. Mathematical modeling can help resolve this issue by quantifying the causal effects of the remodeling features to changes in the LV function in HCM patients. In relation to HCM, a few computational models have been developed to investigate the effects of remodeling features on LV function [154, 168]. Specifically, mathematical models based on an idealized ellipsoidal LV geometry has been developed to investigate how regional strain is affected by myofiber disarray

[152] and sarcomeric mutation [154]. A study was also conducted on the effects of remodeling features associated with HCM by perturbing the heart geometry of a healthy volunteer [168]. Besides LV wall mechanics, other studies have investigated the contribution of diffuse fibrosis distribution in promoting arrhythmogenesis and ventricular arrhythmia in HCM patients [169], as well as the effect of abnormal morphological and functional aspect of the LV on the behavior of intraventricular blood flow dynamics [170]. In the latter study, they found a correlation between higher pressure gradient across the LV outflow tract due to obstruction and the HCM-induced thickening at basal portion of the septum, which further led to clinical indications useful for designing possible surgical treatment by septal myectomy. All these studies, however, do not consider the difference in LV wall mechanics between obstructive and non-obstructive HCM and patient-specific LV geometries that encapsulate the heterogeneous distribution of wall thickness associated with this disease. Other computational studies are focused only on obstructive HCM [153][171], but they did not consider the effects of myofiber disarray.

To address these limitations, we developed patient-specific FE LV models based on clinical measurements from patients with 2 different types of HCM (obstructive and non-obstructive) and a control subject here. These models were constructed based on patient-specific LV geometries that were segmented from cardiac magnetic resonance images of these subjects. The models were coupled to a closed loop circulatory model and calibrated using patient-specific clinical measurements of the LV volume waveform, blood pressures and peak global longitudinal strain (GLS). Contractile function of the cardiac muscle fibers in the 3 subjects were determined by the calibration. The calibrated models were then applied to investigate the effects of different degrees of myofiber disarray on LV function in both the obstructive and non-obstructive HCM subjects.

5.2 Methods

5.2.1 Clinical data

Table 5.1: Clinical measurements of each subject

Parameters	Control	Obstructive	Non-obstructive
Age (years)	69	57	61
Weight (kg)	58.1	97	75
Heart rate (bpm)	60	51	66
End diastolic volume (ml)	63	114	82
End systolic volume (ml)	18	38	12
Ejection fraction (%)	70	66.8	85.3
Global longitudinal strain (%)	-20	-13	-19
Body surface area (m ²)	1.56	2.04	1.72
Blood Pressure (mm Hg)	126/65	151/80	133/66

Clinical data of 2 female HCM patients (obstructive and non-obstructive) along with a control female subject were acquired from the University of California San Francisco Medical Center. Specifically, the data consists of CMR images, blood pressure measurements and peak GLS estimated from 3D echocardiographic images. Left ventricular cavity volume waveform of each subject was estimated by segmenting the endocardial wall from the CMR images (Figure 5.1a) over the cardiac cycle with MeVisLab (MeVis Medical Solutions AG). The clinical data are listed in Table 5.1. In addition to the patient-specific data, we also used published pressure waveforms from HCM patients and healthy human subjects to reconstruct the pressure-volume (PV) loop of each subject [172].

5.2.2 Reconstruction of LV FE model

Left ventricular endocardial and epicardial surfaces were segmented from the MR images associated with end-diastole (ED) (**Figure 5.1b**). Patient-specific 3D LV geometries were then reconstructed from these surfaces and a FE mesh was generated for each geometry. The meshes

consist of approximately 13000 tetrahedral elements (**Figure 5.1c**). Mean myofiber direction (**Figure 5.1d**) e_{f_0} was prescribed based on a linear transmural variation of the helix angle from +70° at the endocardium to -70° at the epicardium across the LV wall using a Laplace-Dirichlet rule-based algorithm [173].

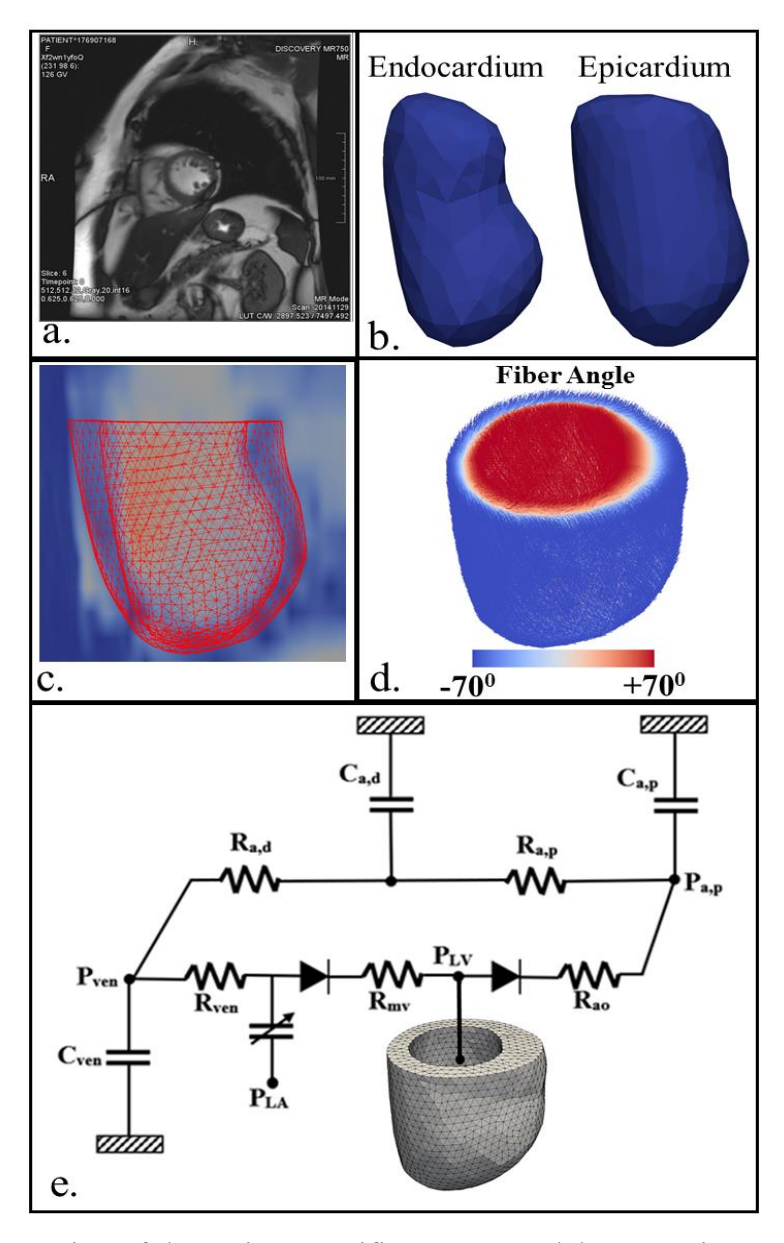


Figure 5.1: Construction of the patient specific LV FE model. **a:** MR image segmentation; **b:** Segmented endocardium and epicardium of the LV; **c:** FE model overlaid on the MR image in a long axis view; **d:** Transmural variation of mean myofiber direction across the LV wall; **e:** Schematic representation of LV FE model coupled with a closed loop circulatory model. A sample representation is shown for non-obstructive HCM patient.

5.2.3 Circulatory model

The computational framework consists of the LV FE model, LA, the proximal (a,p) and distal (a,d) arterial and venous (ven) compartments that are connected in a closed-loop circulatory system (**Figure 5.1 e**)[174–176]. This framework is previously explained in **section 4.2.4**.

5.2.4 FE model formulation

Finite element formulation of the LV model has been described previously [128, 174, 177, 178]. Briefly, denoting z as the apex-to-base axis and x, y are axes orthogonal to z, the functional relationship between pressure and volume of the LV was obtained based on the Lagrangian functional given by,

$$\mathcal{L}(\boldsymbol{u}, p, P_{LV}, c_x, c_y, c_z) = \int_{\Omega_0} W(\boldsymbol{u}) dV - \int_{\Omega_0} p(J-1) dV -$$

$$P_{LV}(V_{LV}(\boldsymbol{u}) - V_{LV}) - c_x \cdot \int_{\Omega_0} u_x dV -$$

$$c_y \cdot \int_{\Omega_0} u_y dV - c_z \cdot \int_{\Omega_0} \boldsymbol{z} \times \boldsymbol{u} dV.$$
(5.1)

In the above equation, u is the displacement field, p is a Lagrange multiplier to enforce incompressibility of the tissue (i.e., Jacobian of the deformation gradient tensor, J=1), P_{LV} is the Lagrange multiplier to constrain the LV cavity volume $V_{LV,cav}(u)$ to a prescribed value V_{LV} [160]. Both c_x and c_y are Lagrange multipliers to constrain rigid body translation in x, y directions and c_z is the Lagrange multiplier to constrain rigid body rotation [161]. The functional relationship between the cavity volumes of the LV to the displacement field is given by,

$$V_{LV}(\boldsymbol{u}) = \int_{\Omega_{k,inner}} dv = -\frac{1}{3} \int_{\Gamma_{k,inner}} \boldsymbol{x}.\,\boldsymbol{n}\,da\,,$$
(5.2)

where $\Omega_{k,inner}$ is the volume enclosed by the inner surface $\Gamma_{k,inner}$ and the basal surface at z=0, and n is the outward unit normal vector.

The first variation of the Lagrangian functional in Eq. (5.1) leads to the following expression:

$$\delta \mathcal{L}(\boldsymbol{u}, p, P_{LV}, c_x, c_y, c_z) = \int_{\Omega_0} (\boldsymbol{P} - p \boldsymbol{F}^{-T}) : \nabla \delta \boldsymbol{u} \, dV - \\
\int_{\Omega_0} \delta p(J-1) \, dV - P_{LV, \text{cav}} \int_{\Omega_0} cof(\boldsymbol{F}) : \nabla \delta \boldsymbol{u} \, dV - \\
\delta P_{LV}(V_{LV}(\boldsymbol{u}) - V_{LV}) - \delta c_x \cdot \int_{\Omega_0} u_x \, dV - \\
\delta c_y \cdot \int_{\Omega_0} u_y \, dV - c_y \cdot \int_{\Omega_0} \delta u_y \, dV - \\
\delta c_z \cdot \int_{\Omega_0} \boldsymbol{z} \times \boldsymbol{u} \, dV - c_x \cdot \int_{\Omega_0} \delta u_x \, dV - \\
c_z \cdot \int_{\Omega_0} \boldsymbol{z} \times \delta \boldsymbol{u} \, dV.$$
(5.3)

In Eq. (5.3), P is the first Piola Kirchhoff stress tensor, F is the deformation gradient tensor, δu , δp , $\delta P_{LV,cav}$, δc_x , δc_y , δc_z are the variation of the displacement field, Lagrange multipliers for enforcing incompressibility and volume constraint, zero mean translation along x and y directions and zero mean rotation along z direction, respectively. The Euler-Lagrange problem then becomes finding $u \in H^1(\Omega_0)$, $p \in L^2(\Omega_0)$, $P_{LV,cav} \in \mathbb{R}$, $c_x \in \mathbb{R}$, $c_y \in \mathbb{R}$, $c_z \in \mathbb{R}$ that satisfies,

$$\delta \mathcal{L}(\boldsymbol{u}, p, P_{LV}, c_x, c_y, c_z) = 0, \qquad (5.4)$$

and $\boldsymbol{u}.\boldsymbol{n}|_{base}=0$ (for constraining the basal deformation to be in-plane) $\forall \, \delta \boldsymbol{u} \in H^1(\Omega_0), \delta p \in L^2(\Omega_0), \delta P_{LV} \in \mathbb{R}, \delta c_x \in \mathbb{R}$, $\delta c_y \in \mathbb{R}$, $\delta c_z \in \mathbb{R}$.

5.2.5 Constitutive relation

Mechanical behavior of the LV was described using an active stress formulation in which the first Piola Kirchhoff stress tensor S was decomposed additively into a passive component S_p and an active component S_a (i.e. $S = S_a + S_p$). The passive stress tensor was defined based on the strain energy function of the Holzapfel-Ogden constitutive model [130, 179, 180] given as

$$W = \frac{a}{2b}e^{b(l_1-3)} + \sum_{i=f,s} \frac{a_i}{2b_i} \left[e^{[b_i(l_{4i}-1)^2]} - 1\right] + \frac{a_{fs}}{2b_{fs}} \left[e^{(b_{fs}l_{8fs}^2)} - 1\right], \tag{5.5a}$$

where

$$C = F^{T}F$$
, $I_{1} = tr(C)$, $I_{4f} = C: H$, (5.5b)
 $I_{4i} = e_{i0} \cdot (Ce_{i0})$, $I_{8fs} = e_{f0} \cdot (Ce_{s0})$.

In Eq. (5.5b), C is the right Cauchy-Green deformation tensor, F is deformation gradient, H is the structure tensor, I_1 , I_{4i} , I_{8fs} are invariants and e_{i0} with $i \in (s, n)$ is a unit vector in the myocardial fiber (f), sheet (s) and sheet normal (n) directions. The effect of myofiber disarray is incorporated via the invariant I_{4f} . Material parameters of the passive constitutive model are denoted by a, b, a_f , b_f , a_s , b_s , a_{fs} and b_{fs} . The structure tensor, H, has been previously explained in section 4.2.2. Active stress calculated based on a previously developed active contraction model [138, 139, 176] was explained briefly in section 4.2.3 by Eq. (4.4) and (4.5).

5.2.6 Simulation cases and protocol

For each subject-specific LV FE model, the following simulations were performed sequentially.

- 1) Estimating the unloaded geometry: First, the unloaded LV configuration was estimated from the LV geometry reconstructed from the CMR images at ED using a backward displacement method [181]. To do so, passive material parameters in the Holzapfel-Ogden model were calibrated manually so that the EDPVR of the LV FE model matches that derived from the single-beat estimation by Klotz et al.[182, 183], which is also applied for HCM subjects.
- 2) Simulation of a beating heart without myofiber disarray ($\kappa = 0$): Following the estimation of unloaded geometry, the unloaded LV FE model was coupled to a closed-loop lumped parameter model of the circulatory system to predict cardiac hemodynamics and mechanics. Myofiber contractility parameter T_{max} in the active contraction model, resistances and compliances in the circulatory model in each subject-specific model were calibrated without myofiber disarray (i.e., $\kappa = 0$) to match the corresponding measured volume waveforms, blood pressure and peak

GLS. The models were also calibrated to maintain a pressure gradient of ~ 60 mmHg across the LVOT assumed for the obstructive HCM subject [184, 185].

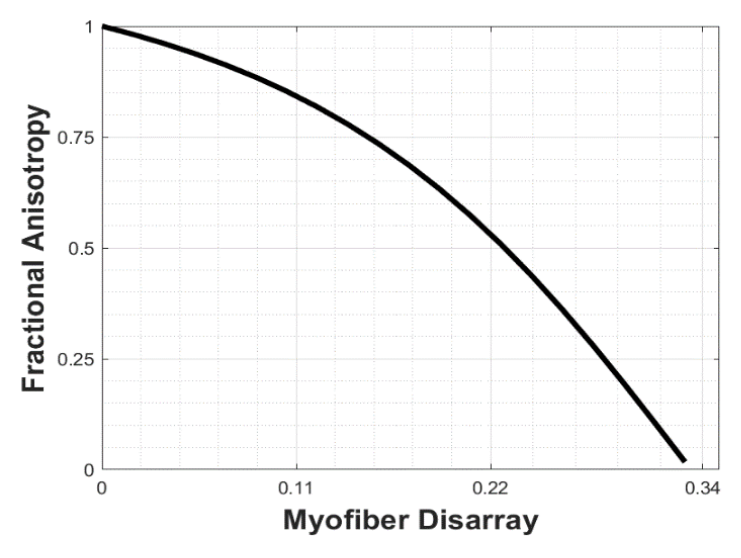


Figure 5.2: Relationship between fractional anisotropy and myofiber disarray.

3) Simulation of a beating heart with disarray ($\kappa > 0$): Thereafter, the relationship between myofiber disarray and myofiber contractility T_{max} was investigated in the 2 HCM patients. To do so, different values of κ was imposed globally into the HCM LV FE models based on fractional anisotropy (FA) measured in HCM patients in previous studies [17, 186, 187]. The relationship between FA and myofiber disarray is shown in **Figure 5.2**, and was established by assuming the structure tensor H to be equivalent to the diffusion tensor measured in the diffusion-tensor MR images (DTMRI). Following the formulation described in Mukherjee et al [188], the eigenvalues ($\lambda_1, \lambda_2, \lambda_3$) of the structure tensor were used to compute the FA based on the following relationship:

$$FA = \sqrt{(\lambda_1 - \lambda_2)^2 + (\lambda_2 - \lambda_3)^2 + (\lambda_3 - \lambda_1)^2} / \sqrt{2(\lambda_1^2 + \lambda_2^2 + \lambda_3^2)},$$
(5.7)

Based on the reported FA, the range of myofiber disarray parameter κ considered here lies between 0.0 to 0.22. For each value of κ , myofiber contractility T_{max} in the active contraction model was adjusted to match the clinical data. We note that the venous resting volume was also adjusted in the obstructive HCM subject in order to keep the EDV at the same value as the measurement and to maintain a pressure gradient across the LVOT as prescribed in previous studies.

5.2.7 Post-processing of simulation

The following quantities were obtained for each simulation of the 3 subjects. Specifically, total normal stress of the myofibers was described by

$$S_f = \mathbf{S} : \mathbf{H} \,, \tag{5.8}$$

where S is the second Piola-Kirchoff stress and H is the structure tensor. respectively. Normal Green-Lagrange strain E_f of the myofibers was determined by

$$E_f = \mathbf{E} : \mathbf{H} \,, \tag{5.9a}$$

$$\mathbf{E} = (\mathbf{C} - \mathbf{I})/2, \tag{5.9b}$$

We note that in the limiting case $\kappa = 0$ (perfect alignment of myofibers), $E_f = e_{f_0} \cdot E \cdot e_{f_0}$ and $S_f = e_{f_0} \cdot S \cdot e_{f_0}$. These stress and strain quantities are used to compute the work density of the myofiber over a cardiac cycle by

$$W_f = \int_{Cardiac \ cycle} S_f \ dE_f, \tag{5.10}$$

Global longitudinal strain was calculated from the right Cauchy-Green stretch tensor with end diastole as the reference configuration C_{ED} by [175]

$$e = \left(1 - \frac{1}{\boldsymbol{e}_I \cdot \boldsymbol{C}_{FD} \cdot \boldsymbol{e}_I}\right) / 2, \tag{5.11}$$

5.2.8 Determination of difference between model prediction and measurements

Relative difference between the model predicted EDPVR and the one based on the empirical relationship by Klotz et al.[182, 183] is defined as

$$err_{passive} = \sum_{i=1}^{N} (P_{klotz}(V_i) - P_{model}(V_i))^2 / \sum_{i=1}^{N} (P_{model}(V_i))^2,$$
 (5.12)

where $P_{klotz}(V)$ and $P_{model}(V)$ are the pressure at the same volume V and N is the number of equally-distributed volume data points in the EDPVR for calculation of the difference. On the other hand, the relative difference between the model predicted and clinical measurements of pressure and volume waveforms over a cardiac cycle is defined as

$$err_{cardiaccycle} = \sum_{i=1}^{M} (y_{clinical}(t_i) - y_{model}(t_i))^2 / \sum_{i=1}^{M} (y_{model}(t_i))^2.$$
 (5.13)

In Eq. (5.13), $y_{clinical} \in \{P_{clinical}, V_{clinical}\}$ and $y_{model} \in \{P_{model}, V_{model}\}$ are, respectively, clinical measurements and model predictions of LV pressure and volume at a particular time point t in the cardiac cycle. Also, M is the no of equally-distributed time steps over a cardiac cycle used to calculate the difference. Relative difference between clinical measurements and model prediction of peak GLS and blood pressure was also calculated for each subject.

5.3 Results

5.3.1 Clinical measurements

End diastolic volume was higher in both HCM subjects (Non-obstructive: 82ml; Obstructive: 115ml) compared to the control subject (63.13ml). Ejection fraction was highest in the non-obstructive HCM subject (85%), and was comparable between obstructive

HCM subject (67%) and the control subject (70%). Absolute peak GLS was reduced substantially in the obstructive HCM subject (13%), but was comparable between the obstructive HCM subject (19%) and the control subject (20%).

5.3.2 LV geometry

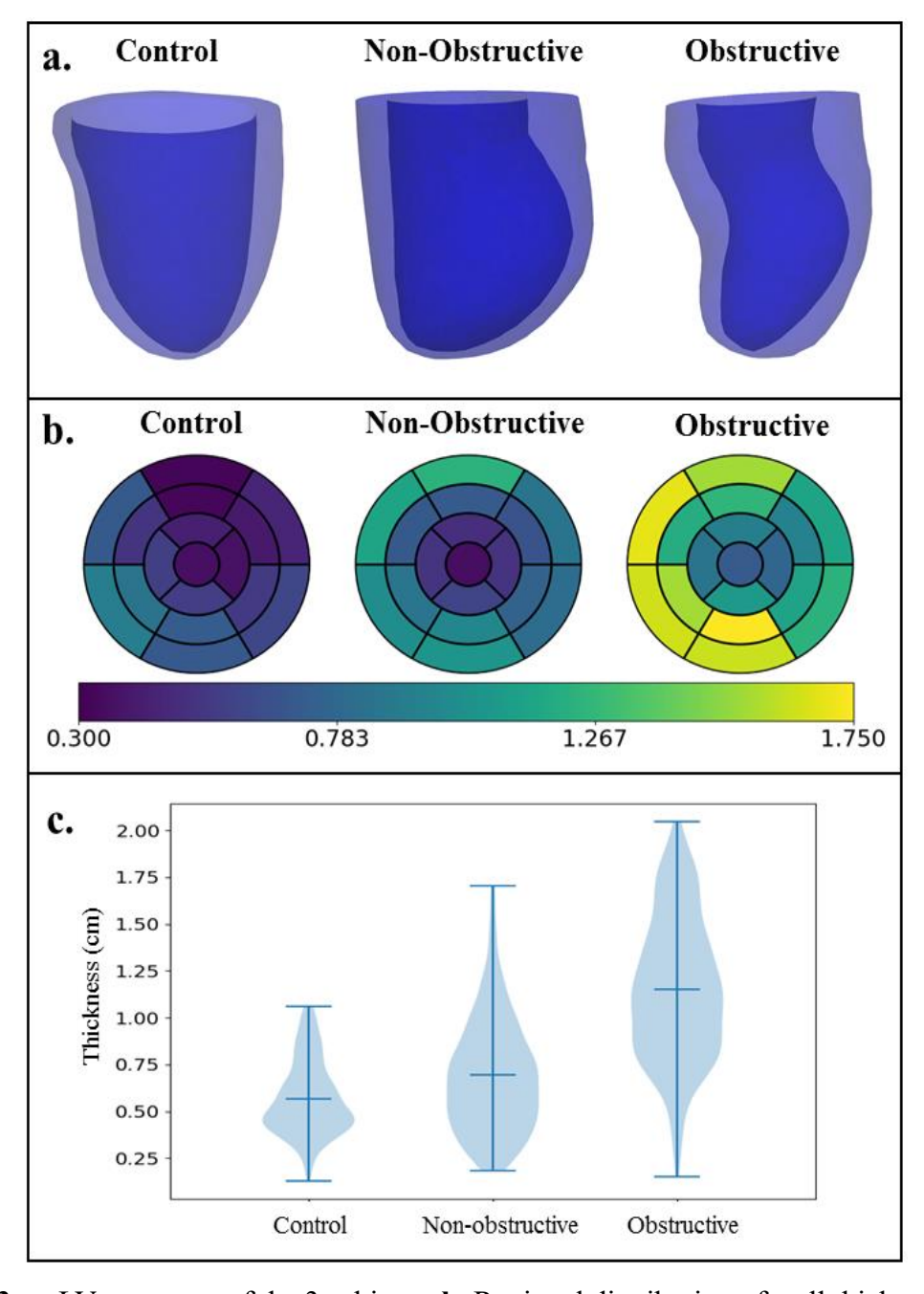


Figure 5.3: a. LV geometry of the 3 subjects. **b.** Regional distribution of wall thickness (in cm) based on AHA segmentation and **c.** Violin plot of the wall thickness.

Left ventricular geometries reconstructed from the CMR images as well as the regional wall thickness based on AHA segmentation for each subject are shown in **Figure 5.3**. Septum wall thickness of the obstructive HCM subject $(1.43 \pm 0.36 \text{ cm})$ was largest followed by that of the non-obstructive HCM subject $(0.85 \pm 0.24 \text{ cm})$ and the control subject $(0.73 \pm 0.14 \text{ cm})$. In each HCM subject, LV free wall thickness was smaller (cf. septum) but was larger when compared to the same region in the control subject (Obstructive HCM: $1.07 \pm 0.18 \text{ cm}$; Non-Obstructive HCM: $0.73 \pm 0.13 \text{ cm}$; Control: $0.5 \pm 0.08 \text{ cm}$). The resultant global wall thickness was higher in the HCM subjects compared to the control (Obstructive HCM: $1.27 \pm 0.33 \text{ cm}$; Non-Obstructive HCM: $0.79 \pm 0.23 \text{ cm}$; Control: $0.58 \pm 0.15 \text{ cm}$).

5.3.3 LV mechanics without consideration of myofiber disarray

The calibrated models' prediction of the EDPVR relationship is consistent with that obtained from the single-beat estimation based on the Klotz relationship (Figure 5.4a). The passive material properties (APPENDIX A) reflected an increased isotropic stiffness (Obstructive: 334.8%, Non-obstructive: 769.6%) and a decrease in stiffness along the fiber direction (over 99%) in both HCM patients when compared to control. The calibrated models' predictions of LV volume waveform, blood pressure and peak GLS also agree with the corresponding patient-specific clinical measurements (Figure 5.4b - e). While LV pressure was not measured in these subjects, the pressure waveforms predicted by the model are also comparable with measurements from previous clinical studies of HCM patients. Differences between the measurements and the model predictions are within about 10%, with the highest difference occurring in the comparison between the EDPVR derived from the empirical Klotz relationship and the model (Figure 5.4f).

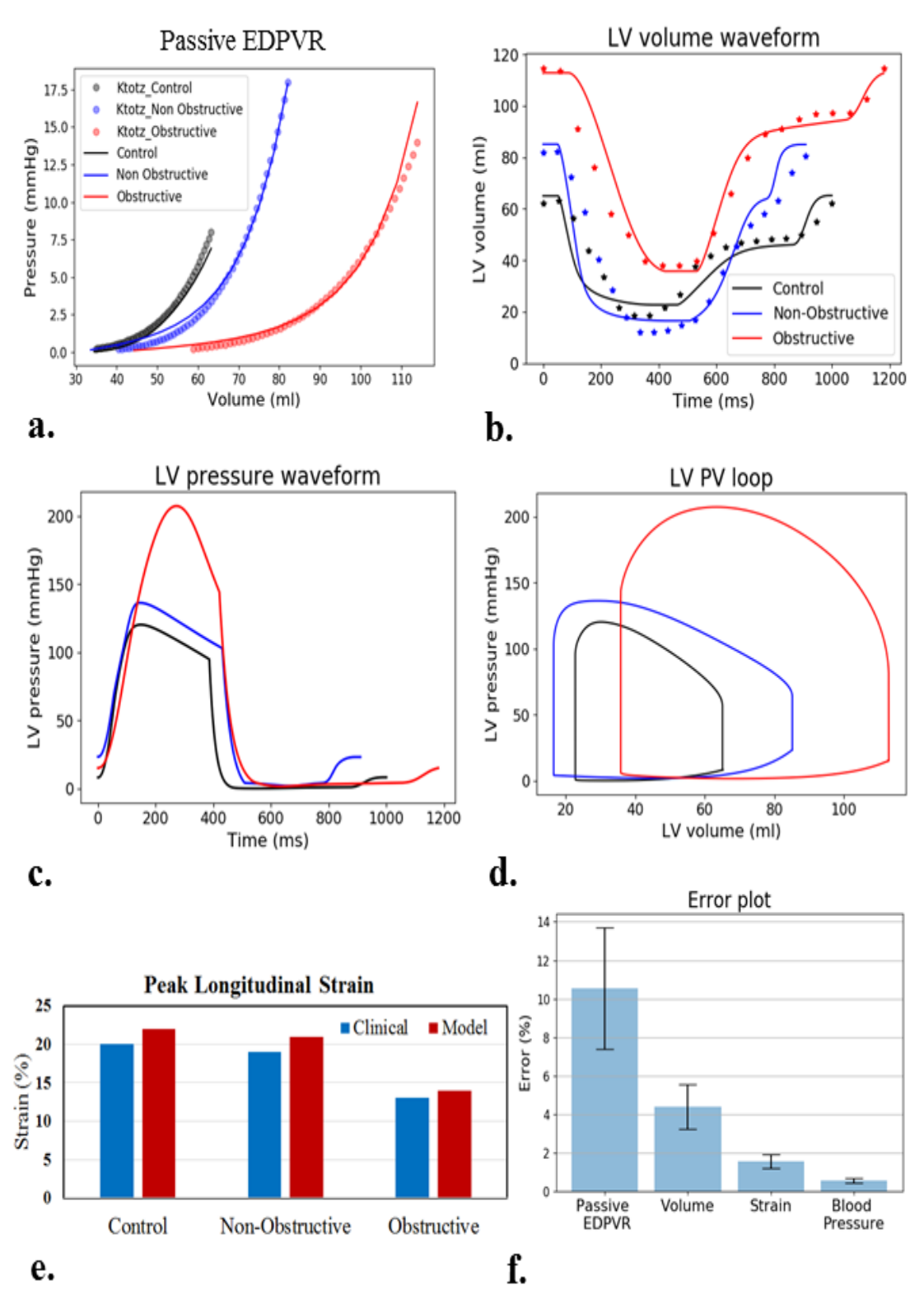


Figure 5.4: Calibration of model parameters for each subject without myofiber disarray. **a.** EDPVR **b.** Volume waveform (Solid line – Simulated results, Dotted line – Clinical results) **c.** Pressure waveform **d.** PV loop **e.** Peak GLS **f.** Difference between model prediction and measurements.

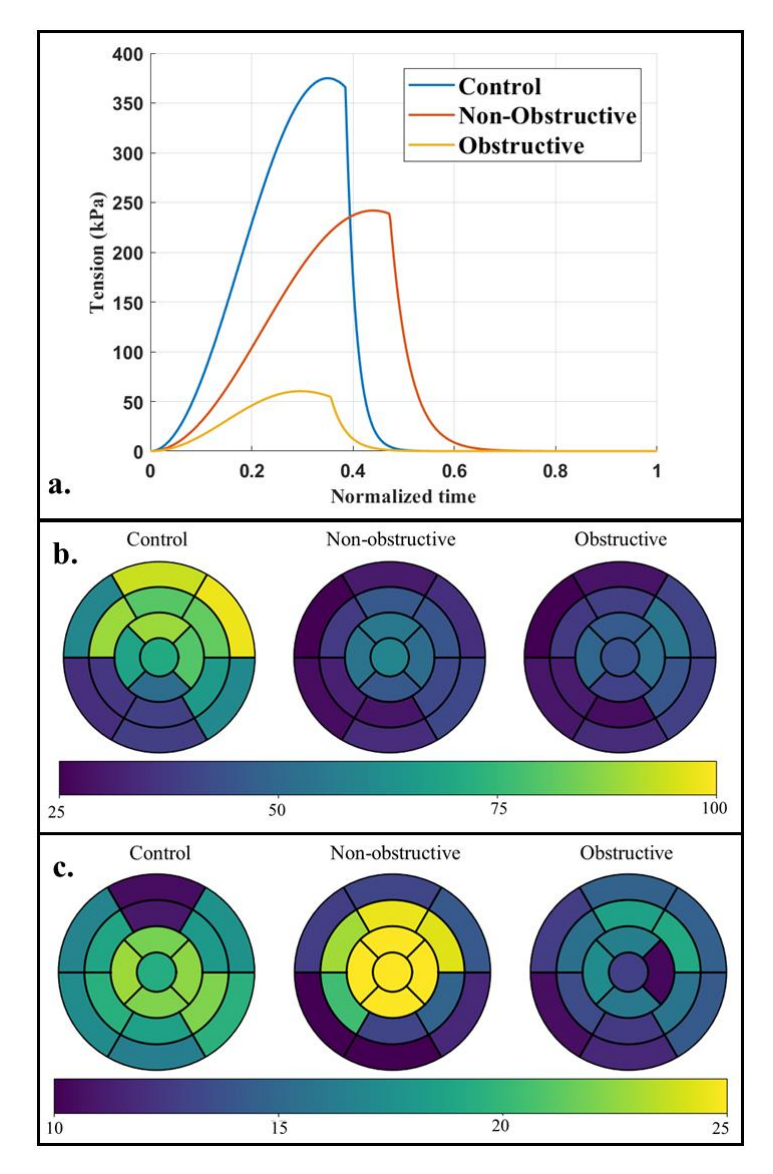


Figure 5.5: a. Isometric tension plot; regional distribution of b. peak total fiber stress (in kPa) and c. peak longitudinal strain (absolute value in %) for each subject.

Peak (isometric) myofiber tension derived from the calibrated active stress model parameters was found to be substantially smaller in the HCM subjects when compared to the control subject (**Figure 5.5a**). The obstructive HCM subject has the smallest peak myofiber tension of 60kPa and the non-obstructive HCM subject has a peak myofiber tension of 242kPa, which were both lower compared to that of the control subject (375kPa). Peak myofiber stress averaged over the entire LV was smallest in the obstructive HCM subject (39 ± 8.85 kPa) followed by the

non-obstructive HCM subject $(40.6 \pm 10.3 \text{ kPa})$ and the control subject $(66.9 \pm 21 \text{ kPa})$ (**Figure 5.5b**). Peak myofiber stress was lower at the septum than the LVFW in both HCM subjects, with the lowest value found in the obstructive HCM subject. Peak GLS was lower in the entire LV of the obstructive HCM subject compared to the other 2 subjects (**Figure 5.5c**). Longitudinal strain was higher at the LVFW (-19.8%) compared to the septum (-12.5%) in the obstructive HCM subject. In the other 2 subjects, however, the difference between longitudinal strain at the septum and LVFW was not prominent (Control: septum -19.5% vs. LVFW -18.8%; non-obstructive HCM: septum -21.8% vs LVFW -18.7%).

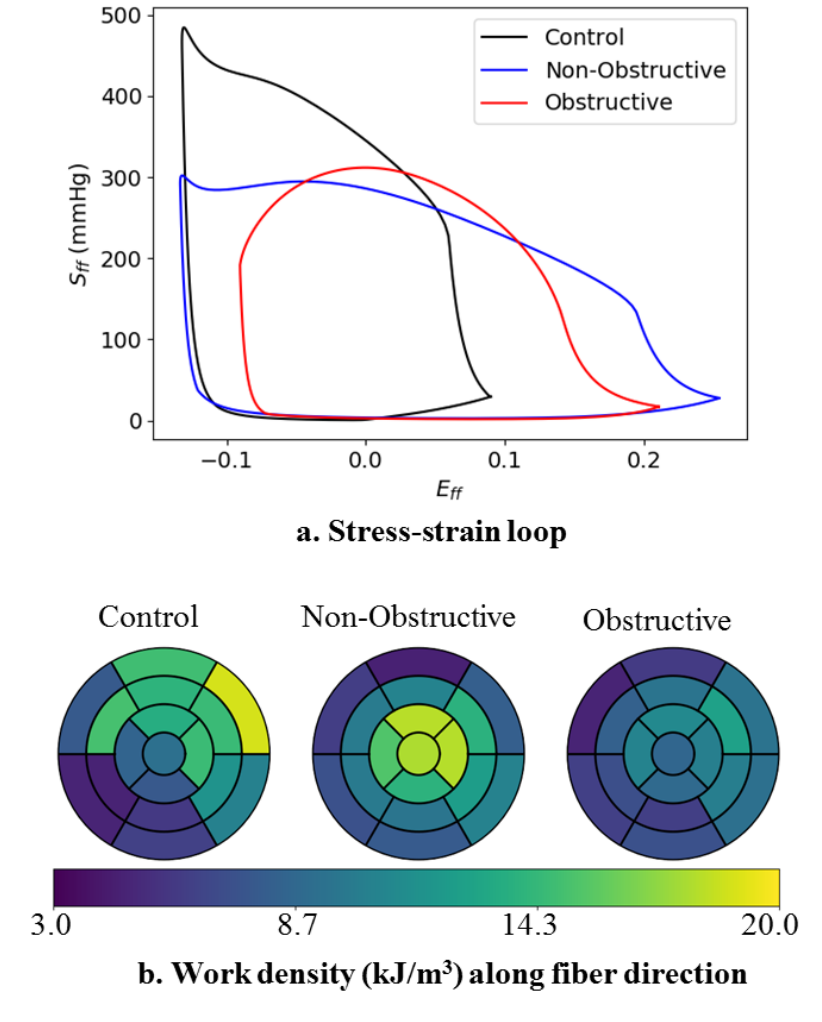


Figure 5.6: Work densities in the HCM and control subjects without myofiber disarray. a. stress-strain loop along mean fiber direction, b. regional distribution of myofiber work density.

Total myofiber work density (indexed by the area of the stress-strain loop along material direction) was lowest in the obstructive HCM subject $(9.0 \ kJ/m^3)$, followed by the control subject $(11.2 \ kJ/m^3)$ and the non-obstructive HCM subject $(11.9 \ kJ/m^3)$ (**Figure 5.6**). In terms of its regional distribution, myofiber work density was higher at the LVFW (control: $14.2 \ kJ/m^3$; non-obstructive: $13.1 \ kJ/m^3$; obstructive: $10.8 \ kJ/m^3$) compared to the septum (control: $8.5 \ kJ/m^3$; non-obstructive: $10.1 \ kJ/m^3$; obstructive: $7.8 \ kJ/m^3$) for all subjects.

5.3.4 Effects of myofiber disarray on the LV mechanics of HCM subjects

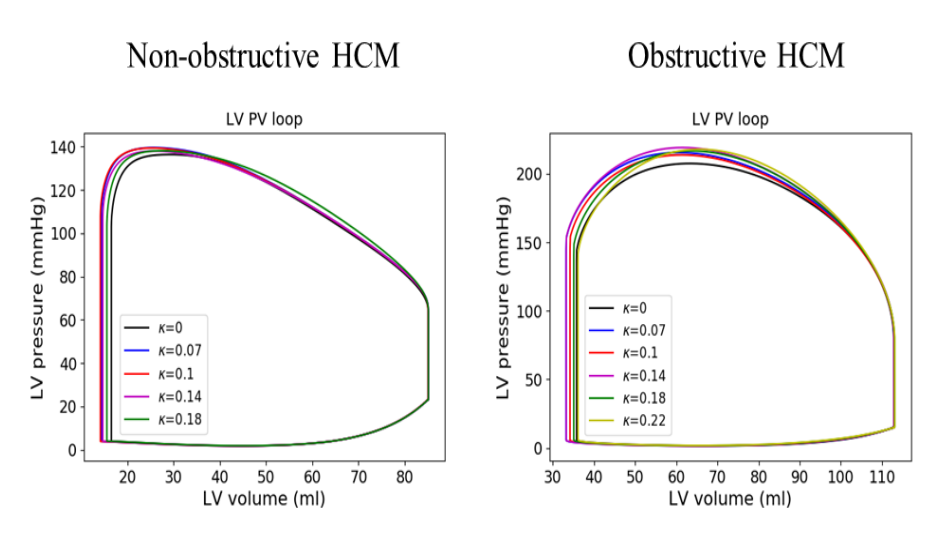


Figure 5.7: PV loop for a. the non-obstructive and b. the obstructive HCM subject.

With an increase in myofiber disarray, it is necessary to increase the scaling parameter T_{max} (associated with myofiber contractility) to match the clinical data of the HCM subjects (**Figure 5.7**). The model parameters are tabulated in **APPENDIX B**. The resultant peak myofiber tension was therefore increased as a result with increasing myofiber disarray (**Figure 5.8**). Specifically, peak myofiber tension associated with the largest degree of disarray was 507.9kPa ($\kappa = 0.18$) and 100.5 kPa ($\kappa = 0.22$) for the non-obstructive and obstructive HCM patients, respectively. Peak GLS did not change substantially (~3%) with increasing myofiber disarray in both HCM subjects. Regional distribution of peak longitudinal strain, peak stress of the myofibers also did not change with different degree of myofiber disarray. In the obstructive HCM subject, peak stress

of the myofibers was decreased in both LVFW and septum with increasing myofiber disarray (**Figure 5.8d**). Conversely in the non-obstructive HCM subject, peak stress of the myofibers was slightly increased with increasing myofiber disarray (**Figure 5.8e**).

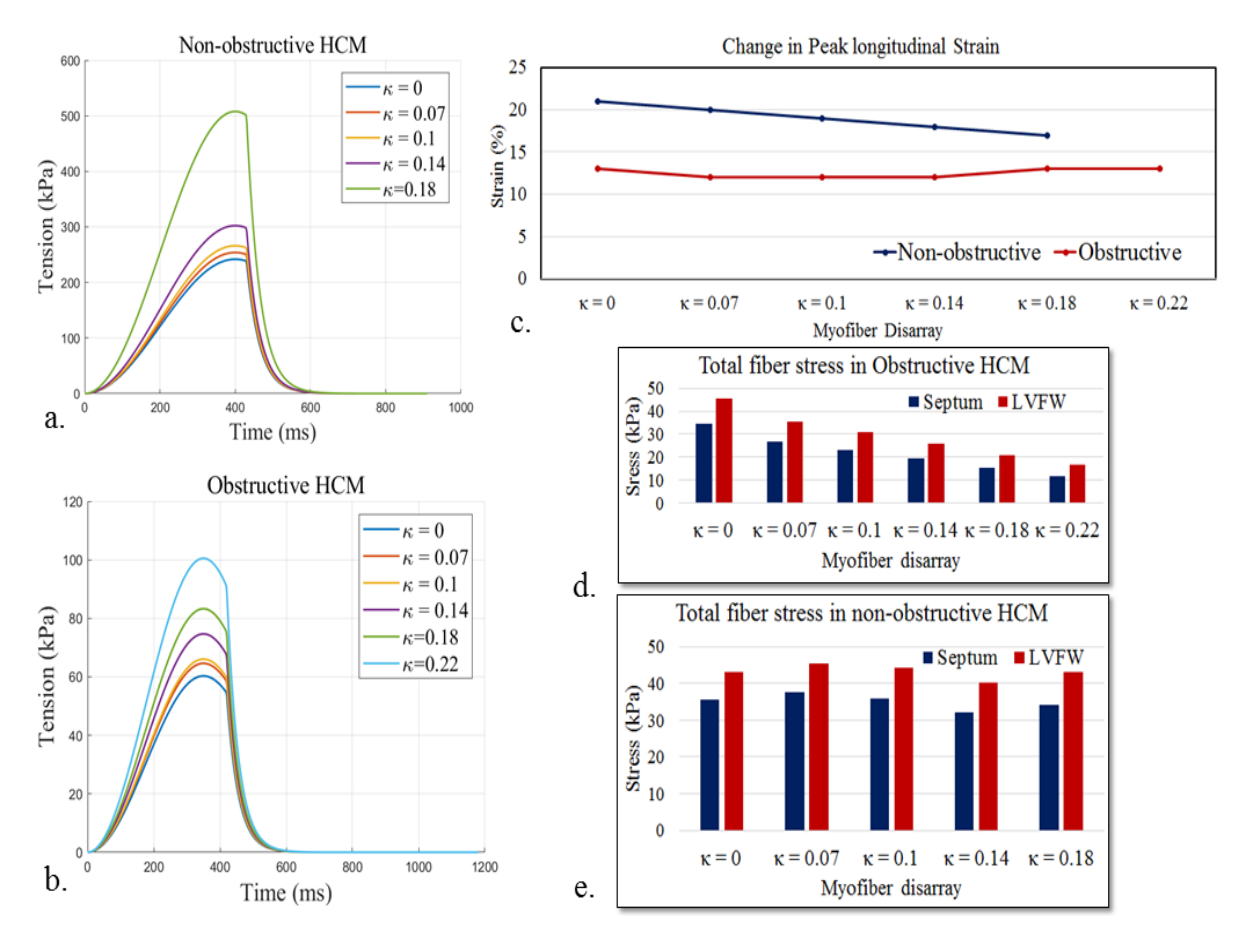


Figure 5.8: Effects of myofiber disarray. Isometric tension-time plot of **a.** non-obstructive and **b.** obstructive HCM subjects. **c.** Peak GLS for the 2 HCM subjects. Peak stress of the myofibers at the septum and LVFW for **d.** obstructive and **e.** non-obstructive HCM subjects.

Myofiber work density was reduced with increasing myofiber disarray in both the non-obstructive HCM subject and obstructive HCM subject (**Figure 5.9a, b**). The reduction in myofiber work density was highest in the septum and lowest in the anterior in the non-obstructive HCM subject (Septum: -74%; Anterior: -71% at $\kappa = 0.18$ cf. $\kappa = 0.0$). On the other hand, in obstructive HCM subject, posterior and LVFW regions have the highest and lowest reduction in myofiber work density, respectively (Posterior: -87%; LVFW: -81% at $\kappa = 0.22$ cf. $\kappa = 0.0$).

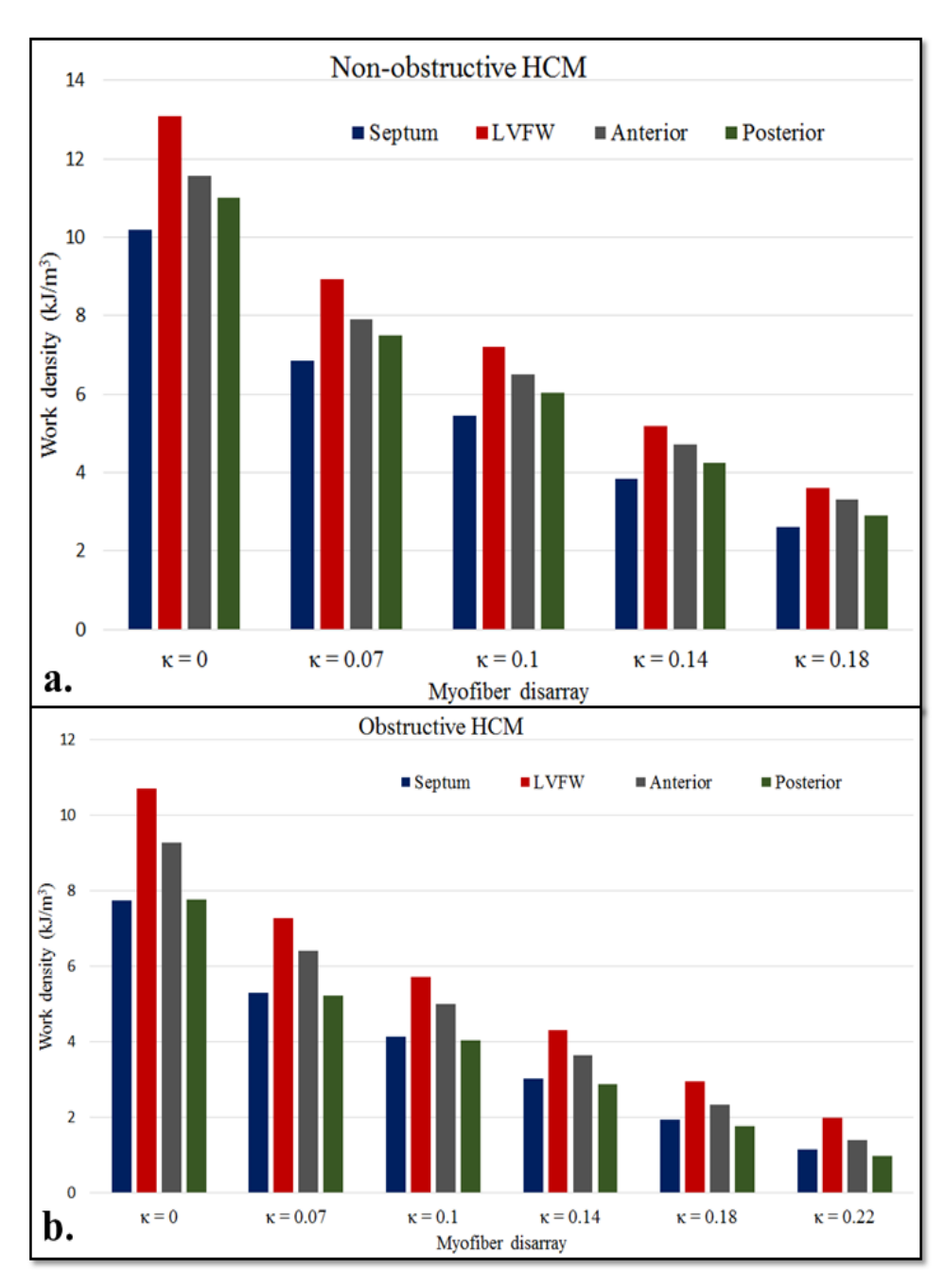


Figure 5.9: Effects of myofiber disarray on myofiber work densities for **a.** the non-obstructive and **b.** the obstructive HCM subject.

5.4 Discussion

We have developed a patient-specific computational framework of LV mechanics to investigate the effects of myofiber disarray using clinical data of 2 HCM subjects with different

phenotypes (obstructive vs non-obstructive) along with a control subject. The key finding of this study suggests that the contractile force generated by the cardiac muscle cell is reduced in the obstructive HCM subject compared to the control subject. In the non-obstructive HCM subject, the contractile force is reduced only if the degree of global myofiber disarray κ is less than 0.14. Specifically, the study found that the contractile force generated by the cell to reproduce the clinical measurements is increased with an increase in global myofiber disarray. An increase in myofiber disarray led to a reduction in myofiber work density in both HCM subjects.

The reconstructed LV geometries of the HCM subjects are consistent with those reported in previous clinical studies. Specifically, the maximum LV wall thickness in the obstructive and non-obstructive HCM subjects are 17.4mm and 12.3 mm are consistent with previous studies [110, 111]. Besides, the ratio of maximum septum wall thickness to minimum posterior wall thickness for the non-obstructive (1.9) and obstructive (1.54) HCM subjects are also within the threshold (≥1.3) used to define asymmetric septal hypertrophy in HCM patients [109].

Both HCM subjects have higher EDV than the control subject (**Figure 5.3**), although ejection fraction is normal (67%) and supra-normal (85%) for the obstructive and non-obstructive HCM subjects, respectively. The supra-normal EF in the non-obstructive HCM patient is a result of its small ESV. Peak GLS is slightly smaller in the non-obstructive HCM subject (19%) compared to the control subject (20%), but is substantially smaller in the obstructive HCM subject (13%).

The smaller peak GLS in the obstructive HCM subject is within the range of -9.65% to -16% reported in previous studies [90, 107]. The results suggest that the reduction in peak GLS is associated with a reduction in myofiber contractility that is indexed by the peak muscle fiber tension. Without considering myofiber disarray, the models predicted that the peak tension to

reproduce the clinical measurements is, respectively, 84% (absolute) and 35% (absolute) smaller in the obstructive and non-obstructive HCM subject when compared to the control subject. By considering myofiber disarray based on the range found in DTMRI studies with κ having values between 0 to 0.22, we found that the peak muscle fiber tension has to increase to compensate for an increasing degree of myofiber disarray in order to reproduce the clinical measurements. Within this range of κ , peak GLS varies by only +/- 2% (absolute) in the obstructive HCM subject and is still depressed compared to the control subject (Figure 5.7c). At the highest degree of myofiber disarray in the obstructive HCM subject, however, the peak muscle fiber tension is still about 72.8 % (absolute) lower than that in the control subject. For the non-obstructive HCM subject, we found that the peak muscle fiber tension is equivalent to the control subject at a disarray $\kappa = 0.14$. At that value of κ , peak GLS is -18 % and lies within the ranges reported previously [189, 190]. These findings therefore suggest myocardial contractility is likely reduced in the HCM subjects, especially in the obstructive phenotype, which can explain the results of a previous CMR study on HCM patients showing that a reduction in FA is associated with a reduction in myocardial strain [186].

The finding that a reduced peak GLS is associated with a reduction in myocardial contractility even with a normal EF is consistent with a previous modeling study based an idealized LV geometry [174]. In that study, only a reduction in myocardial contractility can explain the simultaneous features (including a reduction in GLS) found in patients with HFpEF. Specific to HCM, a reduction in myocardial contractility has also been found in animal studies and is attributed to the mutation of sarcomeric protein [54] [191]. The lower peak tension found here is also consistent with the reduced myofibril density found in vitro studies of myocytes obtained from myocardial biopsies of HCM patients [192].

Peak stress of the myofibers is heterogeneously distributed in the LV (Figure 5.5b). Compared to the control subject, peak myofiber stress is smaller in the HCM subjects, and is smallest in the obstructive HCM subject. This result is largely due to the increase in wall thickness in the HCM subject, and is consistent with previous studies of HCM patients [153, 193]. Peak myofiber wall stress is also lower in the septum (thicker region) than LVFW (thinner region) in all subjects. Between non-obstructive and obstructive HCM subjects, peak stress of the myofibers behaves differently with increasing myofiber disarray (Figure 5.5d, e). With an increase in myofiber disarray, peak stress of the myofibers increases in the non-obstructive HCM subject, whereas decreases in obstructive HCM subject. This result suggests that the effects of myofiber disarray on myofiber stress may be sensitive to geometry.

Global myocardial work density, indexed by the pressure volume area, is linearly correlated to the cardiac metabolism and total myocardial oxygen consumption[194–196]. Local myofiber work density W_f is determined from the area in the average myofiber stress-strain loop (**Figure 5.6**). Without consideration of myofiber disarray, our analysis shows that the non-obstructive HCM subject has the highest mean W_f (11.9 kJ/m^3), followed by the control subject (11.2 kJ/m^3), and the obstructive HCM subject (9.00 kJ/m^3). With disarray where cardiac muscles are oriented in other directions other than the mean myofiber direction, W_f decreases with increasing degree of myofiber disarray in both HCM subjects (**Figure 5.8**). These results showing a lower W_f in the obstructive HCM subject than the non-obstructive HCM subject (and the normal) is consistent with published results of myocardial work index (pressure-strain loop area) assessed noninvasively using echocardiography and blood pressure measurement in HCM patients [197, 198]. The findings that septal W_f is lower than that in the LVFW is also consistent with these studies, especially when in HCM phenotypes with substantial septal hypertrophy. We note that W_f is

defined differently from the myocardial work index measured in the clinic as the latter relies on a global index of stress (i.e., pressure) rather than the local stress of the myofibers. Nevertheless, both of these indices are metric of the total work of the myofiber over a cardiac cycle. Our finding suggests that the development of myofiber disarray further worsens the already lower myofiber work in the HCM subjects, further suggesting that this feature is a contributor to the lower myocardial work index found clinically in HCM patients. The lower work arises because myofibers are disoriented and not contributing efficiently to the overall contraction of the heart (e.g., myofibers oriented in the radial directions are not performing work when the wall thickens during contraction). Therefore, myofiber disarray is one of the key contributors to the worsening of myocardial work in HCM patients (in addition to other features such as mechanical dyssynchrony).

5.5 Conclusion

We have developed patient-specific computational models based on clinical data acquired in 2 HCM (obstructive and non-obstructive) and a control subject to investigate LV mechanics and the relationship between myofiber disarray and myofiber contractility in this disease. Using these models, we show that myofiber contractility must increase to compensate for an increase in myofiber disarray associated with HCM in order to maintain same LV function. For the range of myofiber disarray measured in HCM patients, however, we found that the myofiber contractility in the obstructive HCM subject is still reduced compared to the control subject at the highest degree of myofiber disarray. Myofiber contractility of the non-obstructive HCM subject is close to that of the control subject only when myofiber disarray is substantial with a fractional anisotropy of 0.75. An increase in myofiber disarray also led to a reduction in myofiber work in the HCM subjects. These findings suggest that myofiber contractile stress generated in HCM patients is reduced and

is associated with an increase in wall thickness, and the reduction in myofiber work seen in HCM patients may be due in part to myofiber disarray.

CHAPTER 6 LIMITATIONS AND FUTURE SCOPE

6.1 Biventricular model on Left Bundle Brunch Block

Finite element model based on the idealized biventricular geometry can be developed further. Based on experimental data, incorporation of lateral stretch and wall stress as growth stimuli associated with parallel sarcomere addition can be scope of future study to determine if they are able to reproduce asymmetrical features associated with asynchronous activation. Investigation of change in microstructure property due to remodeling can also be considered. Since preload and afterload can be altered due to G&R, incorporation of the evolution of these two properties over long term G&R modeling to investigate the effect on these in diseased heart and treatment may provide more realism. The model can be further developed by considering electrical conduction through the purkinje fibers. Last, the generalized framework can be further developed through integrating patient specific data.

6.2 Animal specific LV model on pressure overload

Our animal specific computational model is based on two weeks results. Further development of a growth model to simulate G&R associated with pressure overload based on the findings that local changes in myofiber stress is correlated with changes in wall thickness will help better understand the mechanism behind the progression of this disease. The model can be developed by calibrating for mechanical strain found in experimental data related to pressure overload. Besides, future study can investigate any association of local fibrosis seen in pressure overload diseases with local G&R such as changes in wall thickness. As oxygen perfusion gets impaired due to increase in wall thickness, incorporation of a perfusion model will be beneficial, especially for investigating the effect of hypertrophy on regional perfusion.

6.3 Idealized LV model on Hypertrophic Cardiomyopathy

Future studies using an ellipsoidal LV model can investigate the effect of disarray in various geometrical phenotypes of HCM, Also, since in HCM heart, the interaction between actin-myosin play a vital role on the mechanics, incorporation of crossbridge model will be helpful to investigate the interaction of mechanics from cell to organ level. Besides, LV mechanics altered by other features such as fibrosis, extreme outflow tract obstruction, hypertrophy around mid-ventricle and apex can be considered in future.

6.4 Patient specific LV model on Hypertrophic Cardiomyopathy

This study can be extended in future to consider the broad range of disease pattern and variation of morphological phenotypes (such as apical hypertrophy) found in HCM patients. Diffused and regional myofiber disarray based on local DTMRI measurements of myofiber disarray in HCM patients can also be incorporated into the model in future studies. Also, based on LGE quantity, local or diffuse fibrosis can be applied into the model. MD can be considered in future studies using an electromechanics model [128, 177].

6.5 Conclusion

All of these studies suggest that the underlying mechanisms of cardiac hypertrophy are different in different pathological conditions. While these models can help understanding the mechanism of G&R in heart to some extent, a more detailed patient specific multiscale model based on variation in intracellular level (such as genetic expression in specific patient) to change in organ level will provide a pathway to develop treatment and cure for these diseases.

BIBLIOGRAPHY

- 1. Klabunde RE (2005) Cardiovascular physiology concepts / Richard E. Klabunde. In: Cardiovascular physiology concepts
- 2. Lee LC, Kassab GS, Guccione JM (2016) Mathematical modeling of cardiac growth and remodeling. Wiley Interdiscip. Rev. Syst. Biol. Med.
- 3. Maillet M, Van Berlo JH, Molkentin JD (2013) Molecular basis of physiological heart growth: Fundamental concepts and new players. Nat. Rev. Mol. Cell Biol.
- 4. Fernandes T, Soci UPR, Oliveira EM (2011) Eccentric and concentric cardiac hypertrophy induced by exercise training: MicroRNAs and molecular determinants. Brazilian J. Med. Biol. Res.
- 5. Mihl C, Dassen WRM, Kuipers H (2008) Cardiac remodelling: Concentric versus eccentric hypertrophy in strength and endurance athletes. Netherlands Hear. J.
- 6. Müller AL, Dhalla NS (2013) Differences in concentric cardiac hypertrophy and eccentric hypertrophy. In: Cardiac Adaptations: Molecular Mechanisms
- 7. Carruth ED, McCulloch AD, Omens JH (2016) Transmural gradients of myocardial structure and mechanics: Implications for fiber stress and strain in pressure overload. Prog. Biophys. Mol. Biol.
- 8. Grossman W (1980) Cardiac hypertrophy: Useful adaptation or pathologic process? Am. J. Med.
- 9. Tamura T, Onodera T, Said S, Gerdes AM (1998) Correlation of myocyte lengthening to chamber dilation in the spontaneously hypertensive heart failure (SHHF) rat. J Mol Cell Cardiol. https://doi.org/10.1006/jmcc.1998.0775
- 10. Jalil JE, Doering CW, Janicki JS, et al (1988) Structural vs. contractile protein remodeling and myocardial stiffness in hypertrophied rat left ventricle. J Mol Cell Cardiol. https://doi.org/10.1016/0022-2828(88)90597-4
- 11. Yin FC (1981) Ventricular wall stress. Circ. Res.
- 12. Shoucri RM (2000) Active and passive stresses in the myocardium. Am J Physiol Hear Circ Physiol. https://doi.org/10.1152/ajpheart.2000.279.5.h2519
- 13. Grossman W, Jones D, McLaurin LP (1975) Wall stress and patterns of hypertrophy in the human left ventricle. J Clin Invest. https://doi.org/10.1172/JCI108079
- 14. Coelho-Filho OR, Shah R V., Mitchell R, et al (2013) Quantification of cardiomyocyte hypertrophy by cardiac magnetic resonance: Implications for early cardiac remodeling. Circulation. https://doi.org/10.1161/CIRCULATIONAHA.112.000438

- 15. Peter AK, Bjerke MA, Leinwand LA (2016) Biology of the cardiac myocyte in heart disease. Mol. Biol. Cell
- 16. Gorman RC, Jackson BM, Gorman JH, Edmunds LH (2005) The Mechanics of the Fibrosed/Remodeled Heart
- 17. Ariga R, Tunnicliffe EM, Manohar SG, et al (2019) Identification of Myocardial Disarray in Patients With Hypertrophic Cardiomyopathy and Ventricular Arrhythmias. J Am Coll Cardiol. https://doi.org/10.1016/j.jacc.2019.02.065
- 18. Van Pelt NC, Stewart RAH, Legget ME, et al (2007) Longitudinal left ventricular contractile dysfunction after exercise in aortic stenosis. Heart. https://doi.org/10.1136/hrt.2006.100164
- 19. MacIver DH, Clark AL (2016) Contractile Dysfunction in Sarcomeric Hypertrophic Cardiomyopathy. J. Card. Fail.
- 20. Lammerding J, Kamm RD, Lee RT (2004) Mechanotransduction in cardiac myocytes. In: Annals of the New York Academy of Sciences
- 21. Breithardt OA, Stellbrink C, Herbots L, et al (2003) Cardiac resynchronization therapy can reverse abnormal myocardial strain distribution in patients with heart failure and left bundle branch block. J Am Coll Cardiol 42:486–494. https://doi.org/10.1016/s0735-1097(03)00709-5
- 22. Lee LC, Kassab GS, Guccione JM (2016) Mathematical modeling of cardiac growth and remodeling. Wiley Interdiscip. Rev. Syst. Biol. Med.
- 23. Witzenburg CM, Holmes JW (2017) A Comparison of Phenomenologic Growth Laws for Myocardial Hypertrophy. J Elast. https://doi.org/10.1007/s10659-017-9631-8
- 24. Niestrawska JA, Augustin CM, Plank G (2020) Computational modeling of cardiac growth and remodeling in pressure overloaded hearts—Linking microstructure to organ phenotype. Acta Biomater 106:34–53. https://doi.org/https://doi.org/10.1016/j.actbio.2020.02.010
- 25. Sharifi H, Mann CK, Rockward AL, et al (2021) Multiscale simulations of left ventricular growth and remodeling. Biophys Rev 13:729–746. https://doi.org/10.1007/s12551-021-00826-5
- 26. Nakamura M, Sadoshima J (2018) Mechanisms of physiological and pathological cardiac hypertrophy. Nat Rev Cardiol 15:387–407. https://doi.org/10.1038/s41569-018-0007-y
- 27. Rodriguez EK, Hoger A, McCulloch AD (1994) Stress-dependent finite growth in soft elastic tissues. J Biomech. https://doi.org/10.1016/0021-9290(94)90021-3
- 28. Lubarda VA, Hoger A (2002) On the mechanics of solids with a growing mass. Int J Solids Struct. https://doi.org/10.1016/S0020-7683(02)00352-9

- 29. Lee LC, Sundnes J, Genet M, et al (2016) An integrated electromechanical-growth heart model for simulating cardiac therapies. Biomech Model Mechanobiol. https://doi.org/10.1007/s10237-015-0723-8
- 30. Göktepe S, Abilez OJ, Parker KK, Kuhl E (2010) A multiscale model for eccentric and concentric cardiac growth through sarcomerogenesis. J Theor Biol. https://doi.org/10.1016/j.jtbi.2010.04.023
- 31. Kerckhoffs RCP, Omens JH, McCulloch AD (2012) A single strain-based growth law predicts concentric and eccentric cardiac growth during pressure and volume overload. Mech Res Commun. https://doi.org/10.1016/j.mechrescom.2011.11.004
- 32. Göktepe S, Abilez OJ, Kuhl E (2010) A generic approach towards finite growth with examples of athlete's heart, cardiac dilation, and cardiac wall thickening. J Mech Phys Solids. https://doi.org/10.1016/j.jmps.2010.07.003
- 33. Rausch MK, Dam A, Göktepe S, et al (2011) Computational modeling of growth: Systemic and pulmonary hypertension in the heart. Biomech Model Mechanobiol. https://doi.org/10.1007/s10237-010-0275-x
- 34. Yoshida K, McCulloch AD, Omens JH, Holmes JW (2019) Predictions of hypertrophy and its regression in response to pressure overload. Biomech Model Mechanobiol. https://doi.org/10.1007/s10237-019-01271-w
- 35. Neal ML, Kerckhoffs R (2009) Current progress in patient-specific modeling. Brief Bioinform. https://doi.org/10.1093/bib/bbp049
- 36. Prinzen FW, Augustijn CH, Arts T, et al (1990) Redistribution of myocardial fiber strain and blood flow by asynchronous activation. Am J Physiol Hear Circ Physiol. https://doi.org/10.1152/ajpheart.1990.259.2.h300
- 37. Zhang Q, Yu C-M (2012) Clinical implication of mechanical dyssynchrony in heart failure. J Cardiovasc Ultrasound 20:117–123. https://doi.org/10.4250/jcu.2012.20.3.117
- 38. Bear LR, Huntjens PR, Walton RD, et al (2018) Cardiac electrical dyssynchrony is accurately detected by noninvasive electrocardiographic imaging. Hear Rhythm 15:1058–1069. https://doi.org/10.1016/j.hrthm.2018.02.024
- 39. Fahy GJ, Pinski SL, Miller DP, et al (1996) Natural history of isolated bundle branch block. Am J Cardiol 77:1185–1190. https://doi.org/10.1016/s0002-9149(96)00160-9
- 40. Eriksson P, Wilhelmsen L, Rosengren A (2005) Bundle-branch block in middle-aged men: Risk of complications and death over 28 years The primary prevention study in Göteborg, Sweden. Eur Heart J. https://doi.org/10.1093/eurheartj/ehi580
- 41. Schneider JF, Emerson Thomas H, Sorlie P, et al (1981) Comparative features of newly acquired left and right bundle branch block in the general population: The framingham study. Am J Cardiol. https://doi.org/10.1016/0002-9149(81)90196-X

- 42. Delhaas T, Arts T, Prinzen FW, Reneman RS (1994) Regional fibre stress-fibre strain area as an estimate of regional blood flow and oxygen demand in the canine heart. J Physiol 477:481–496. https://doi.org/https://doi.org/10.1113/jphysiol.1994.sp020209
- 43. van Oosterhout MF, Prinzen FW, Arts T, et al (1998) Asynchronous electrical activation induces asymmetrical hypertrophy of the left ventricular wall. Circulation 98:588–595. https://doi.org/10.1161/01.cir.98.6.588
- 44. Prinzen FW, Cheriex EC, Delhaas T, et al (1995) Asymmetric thickness of the left ventricular wall resulting from asynchronous electric activation: A study in dogs with ventricular pacing and in patients with left bundle branch block. Am Heart J 130:1045–1053. https://doi.org/https://doi.org/10.1016/0002-8703(95)90207-4
- 45. Norton JM (2001) Toward consistent definitions for preload and afterload. Am. J. Physiol. Adv. Physiol. Educ.
- 46. Frohlich ED, Susic D (2012) Pressure overload. Heart Fail Clin 8:21–32. https://doi.org/10.1016/j.hfc.2011.08.005
- 47. Schwarzer M (2016) Chapter 8 Models to Investigate Cardiac Metabolism. In: Schwarzer M, Doenst TBT-TSG to CM (eds). Academic Press, Boston, pp 103–122
- 48. Ding Y, Wang Y, Jia Q, et al (2020) Morphological and Functional Characteristics of Animal Models of Myocardial Fibrosis Induced by Pressure Overload. Int J Hypertens 2020:3014693. https://doi.org/10.1155/2020/3014693
- 49. Molina EJ, Gupta D, Palma J, et al (2009) Novel Experimental Model of Pressure Overload Hypertrophy in Rats. J Surg Res 153:287–294. https://doi.org/https://doi.org/10.1016/j.jss.2008.03.043
- 50. Melleby AO, Romaine A, Aronsen JM, et al (2018) A novel method for high precision aortic constriction that allows for generation of specific cardiac phenotypes in mice. Cardiovasc Res 114:1680–1690. https://doi.org/10.1093/cvr/cvy141
- 51. Niimura H, Patton KK, McKenna WJ, et al (2002) Sarcomere protein gene mutations in hypertrophic cardiomyopathy of the elderly. Circulation. https://doi.org/10.1161/hc0402.102990
- 52. Arad M, Penas-Lado M, Monserrat L, et al (2005) Gene mutations in apical hypertrophic cardiomyopathy. Circulation. https://doi.org/10.1161/CIRCULATIONAHA.105.547448
- 53. Niimura H, Bachinski LL, Sangwatanaroj S, et al (1998) Mutations in the Gene for Cardiac Myosin-Binding Protein C and Late-Onset Familial Hypertrophic Cardiomyopathy. N Engl J Med. https://doi.org/10.1056/nejm199804303381802
- 54. Geisterfer-Lowrance AAT, Kass S, Tanigawa G, et al (1990) A molecular basis for familial hypertrophic cardiomyopathy: A β cardiac myosin heavy chain gene missense mutation. Cell. https://doi.org/10.1016/0092-8674(90)90274-I

- 55. Thierfelder L, Watkins H, MacRae C, et al (1994) α-tropomyosin and cardiac troponin T mutations cause familial hypertrophic cardiomyopathy: A disease of the sarcomere. Cell. https://doi.org/10.1016/0092-8674(94)90054-X
- 56. Crilley JG, Boehm EA, Blair E, et al (2003) Hypertrophic cardiomyopathy due to sarcomeric gene mutations is characterized by impaired energy metabolism irrespective of the degree of hypertrophy. J Am Coll Cardiol 41:1776–1782. https://doi.org/10.1016/S0735-1097(02)03009-7
- 57. Makavos G, Kairis C, Tselegkidi M-E, et al (2019) Hypertrophic cardiomyopathy: an updated review on diagnosis, prognosis, and treatment. Heart Fail Rev 24:439–459. https://doi.org/10.1007/s10741-019-09775-4
- 58. Ho CY, Day SM, Ashley EA, et al (2018) Genotype and lifetime burden of disease in hypertrophic cardiomyopathy insights from the sarcomeric human cardiomyopathy registry (SHaRe). Circulation. https://doi.org/10.1161/CIRCULATIONAHA.117.033200
- 59. B.J. M (2002) Hypertrophic cardiomyopathy: A systematic review. J Am Med Assoc
- 60. Maron BJ, Olivotto I, Spirito P, et al (2000) Epidemiology of hypertrophic cardiomyopathyrelated death: Revisited in a large non-referral-based patient population. Circulation. https://doi.org/10.1161/01.CIR.102.8.858
- 61. Maron BJ, McKenna WJ, Danielson GK, et al (2003) American College of Cardiology/European Society of Cardiology clinical expert consensus document on hypertrophic cardiomyopathy. A report of the American College of Cardiology Foundation Task Force on Clinical Expert Consensus Documents and the European . J Am Coll Cardiol 42:1687–1713. https://doi.org/10.1016/s0735-1097(03)00941-0
- 62. Jordà P, García-Álvarez A (2018) Hypertrophic cardiomyopathy: Sudden cardiac death risk stratification in adults. Glob Cardiol Sci Pract 2018:25. https://doi.org/10.21542/gcsp.2018.25
- 63. Cirino AL, Ho C (1993) Hypertrophic Cardiomyopathy Overview
- 64. Weissler-Snir A, Allan K, Cunningham K, et al (2019) Hypertrophic Cardiomyopathy-Related Sudden Cardiac Death in Young People in Ontario. Circulation 140:1706–1716. https://doi.org/10.1161/CIRCULATIONAHA.119.040271
- 65. Norrish G, Ding T, Field E, et al (2019) Development of a Novel Risk Prediction Model for Sudden Cardiac Death in Childhood Hypertrophic Cardiomyopathy (HCM Risk-Kids). JAMA Cardiol 4:918–927. https://doi.org/10.1001/jamacardio.2019.2861
- 66. Gersh BJ, Maron BJ, Bonow RO, et al (2011) 2011 ACCF/AHA guideline for the diagnosis and treatment of hypertrophic cardiomyopathy: executive summary: a report of the American College of Cardiology Foundation/American Heart Association Task Force on Practice Guidelines. Circulation 124:2761–2796. https://doi.org/10.1161/CIR.0b013e318223e230

- 67. Hong Y, Su WW, Li X (2022) Risk factors of sudden cardiac death in hypertrophic cardiomyopathy. Curr Opin Cardiol 37:
- 68. Ommen SR, Mital S, Burke MA, et al (2020) 2020 AHA/ACC Guideline for the Diagnosis and Treatment of Patients With Hypertrophic Cardiomyopathy: A Report of the American College of Cardiology/American Heart Association Joint Committee on Clinical Practice Guidelines. Circulation 142:e558–e631. https://doi.org/10.1161/CIR.0000000000000937
- 69. Zampieri M, Argirò A, Marchi A, et al (2021) Mavacamten, a Novel Therapeutic Strategy for Obstructive Hypertrophic Cardiomyopathy. Curr Cardiol Rep 23:79. https://doi.org/10.1007/s11886-021-01508-0
- 70. Saberi S, Cardim N, Yamani M, et al (2021) Mavacamten Favorably Impacts Cardiac Structure in Obstructive Hypertrophic Cardiomyopathy. Circulation 143:606–608. https://doi.org/10.1161/CIRCULATIONAHA.120.052359
- 71. Hegde SM, Lester SJ, Solomon SD, et al (2021) Effect of Mavacamten on Echocardiographic Features in Symptomatic Patients With Obstructive Hypertrophic Cardiomyopathy. J Am Coll Cardiol 78:2518–2532. https://doi.org/https://doi.org/10.1016/j.jacc.2021.09.1381
- 72. Ho CY, Mealiffe ME, Bach RG, et al (2020) Evaluation of Mavacamten in Symptomatic Patients With Nonobstructive Hypertrophic Cardiomyopathy. J Am Coll Cardiol 75:2649–2660. https://doi.org/https://doi.org/10.1016/j.jacc.2020.03.064
- 73. Syed IS, Ommen SR, Breen JF, Tajik AJ (2008) Hypertrophic cardiomyopathy: identification of morphological subtypes by echocardiography and cardiac magnetic resonance imaging. JACC Cardiovasc Imaging 1:377–379. https://doi.org/10.1016/j.jcmg.2008.02.008
- 74. BRAUNWALD E, LAMBREW CT, ROCKOFF SD, et al (1964) Idiopathic Hypertrophic Subaortic Stenosis: I. A Description of the Disease Based Upon an Analysis of 64 Patients. Circulation 29:IV-3-IV-119. https://doi.org/10.1161/01.CIR.29.5S4.IV-3
- 75. Shapiro LM, McKenna WJ (1983) Distribution of left ventricular hypertrophy in hypertrophic cardiomyopathy: A two-dimensional echocardiographic study. J Am Coll Cardiol 2:437–444. https://doi.org/https://doi.org/10.1016/S0735-1097(83)80269-1
- 76. Veselka J, Anavekar NS, Charron P (2017) Hypertrophic obstructive cardiomyopathy. Lancet 389:1253–1267. https://doi.org/https://doi.org/10.1016/S0140-6736(16)31321-6
- 77. Maron BJ, Gottdiener JS, Epstein SE (1981) Patterns and significance of distribution of left ventricular hypertrophy in hypertrophic cardiomyopathy: A wide angle, two dimensional echocardiographic study of 125 patients. Am J Cardiol 48:418–428. https://doi.org/https://doi.org/10.1016/0002-9149(81)90068-0
- 78. Wigle ED, Sasson Z, Henderson MA, et al (1985) Hypertrophic cardiomyopathy. The importance of the site and the extent of hypertrophy. A review. Prog Cardiovasc Dis 28:1–

- 83. https://doi.org/10.1016/0033-0620(85)90024-6
- 79. members AF, Elliott PM, Anastasakis A, et al (2014) 2014 ESC Guidelines on diagnosis and management of hypertrophic cardiomyopathy: The Task Force for the Diagnosis and Management of Hypertrophic Cardiomyopathy of the European Society of Cardiology (ESC). Eur Heart J 35:2733–2779. https://doi.org/10.1093/eurheartj/ehu284
- 80. Maron BJ, Anan TJ, Roberts WC (1981) Quantitative analysis of the distribution of cardiac muscle cell disorganization in the left ventricular wall of patients with hypertonic cardiomyopathy. Circulation. https://doi.org/10.1161/01.CIR.63.4.882
- 81. St John Sutton MG, Lie JT, Anderson KR, et al (1980) Histopathological specificity of hypertrophic obstructive cardiomyopathy. Myocardial fibre disarray and myocardial fibrosis. Br Heart J. https://doi.org/10.1136/hrt.44.4.433
- 82. Maron BJ, Sato N, Roberts WC, et al (1979) Quantitative analysis of cardiac muscle cell disorganization in the ventricular septum. Comparison of fetuses and infants with and without congenital heart disease and patients with hypertrophic cardiomyopathy. Circulation. https://doi.org/10.1161/01.CIR.60.3.685
- 83. Maron BJ, Roberts WC (1979) Quantitative analysis of cardiac muscle cell disorganization in the ventricular septum of patients with hypertrophic cardiomyopathy. Circulation. https://doi.org/10.1161/01.CIR.59.4.689
- 84. Harris SP, Bartley CR, Hacker TA, et al (2002) Hypertrophic cardiomyopathy in cardiac myosin binding protein-C knockout mice. Circ Res. https://doi.org/10.1161/01.RES.0000012222.70819.64
- 85. Korte FS, McDonald KS, Harris SP, Moss RL (2003) Loaded Shortening, Power Output, and Rate of Force Redevelopment Are Increased With Knockout of Cardiac Myosin Binding Protein-C. Circ Res. https://doi.org/10.1161/01.RES.0000096363.85588.9A
- 86. Carrier L, Knöll R, Vignier N, et al (2004) Asymmetric septal hypertrophy in heterozygous cMyBP-C null mice. Cardiovasc Res. https://doi.org/10.1016/j.cardiores.2004.04.009
- 87. Brickson S, Fitzsimons DP, Pereira L, et al (2007) In vivo left ventricular functional capacity is compromised in cMyBP-C null mice. Am J Physiol Hear Circ Physiol. https://doi.org/10.1152/ajpheart.01037.2006
- 88. Luther PK, Bennett PM, Knupp C, et al (2008) Understanding the Organisation and Role of Myosin Binding Protein C in Normal Striated Muscle by Comparison with MyBP-C Knockout Cardiac Muscle. J Mol Biol. https://doi.org/10.1016/j.jmb.2008.09.013
- 89. Garcia-Canadilla P, Cook AC, Mohun TJ, et al (2019) Myoarchitectural disarray of hypertrophic cardiomyopathy begins pre-birth. J Anat. https://doi.org/10.1111/joa.13058
- 90. Tower-Rader A, Mohananey D, To A, et al (2019) Prognostic Value of Global Longitudinal Strain in Hypertrophic Cardiomyopathy: A Systematic Review of Existing Literature.

- JACC Cardiovasc Imaging 12:1930–1942. https://doi.org/10.1016/j.jcmg.2018.07.016
- 91. Sun JP, Stewart WJ, Yang XS, et al (2009) Differentiation of Hypertrophic Cardiomyopathy and Cardiac Amyloidosis from Other Causes of Ventricular Wall Thickening by Two-Dimensional Strain Imaging Echocardiography. Am J Cardiol. https://doi.org/10.1016/j.amjcard.2008.09.102
- 92. Piella G, De Craene M, Bijnens BH, et al (2010) Characterizing Myocardial Deformation in Patients With Left Ventricular Hypertrophy of Different Etiologies Using the Strain Distribution Obtained by Magnetic Resonance Imaging. Rev Española Cardiol (English Ed. https://doi.org/10.1016/s1885-5857(10)70253-x
- 93. Wijnker PJM, Sequeira V, Kuster DWD, Velden J van der (2019) Hypertrophic Cardiomyopathy: A Vicious Cycle Triggered by Sarcomere Mutations and Secondary Disease Hits. Antioxid Redox Signal 31:318–358. https://doi.org/10.1089/ars.2017.7236
- 94. Hiemstra YL, van der Bijl P, el Mahdiui M, et al (2020) Myocardial Work in Nonobstructive Hypertrophic Cardiomyopathy: Implications for Outcome. J Am Soc Echocardiogr 33:1201–1208. https://doi.org/https://doi.org/10.1016/j.echo.2020.05.010
- 95. Galati G, Leone O, Pasquale F, et al (2016) Histological and Histometric Characterization of Myocardial Fibrosis in End-Stage Hypertrophic Cardiomyopathy. Circ Hear Fail 9:e003090. https://doi.org/10.1161/CIRCHEARTFAILURE.116.003090
- 96. Marian AJ, Braunwald E (2017) Hypertrophic cardiomyopathy: Genetics, pathogenesis, clinical manifestations, diagnosis, and therapy. Circ Res. https://doi.org/10.1161/CIRCRESAHA.117.311059
- 97. Maron BJ, Wolfson JK, Roberts WC (1992) Relation between extent of cardiac muscle cell disorganization and left ventricular wall thickness in hypertrophic cardiomyopathy. Am J Cardiol. https://doi.org/10.1016/0002-9149(92)90560-L
- 98. Tanaka A, Yuasa S, Mearini G, et al (2014) Endothelin-1 induces myofibrillar disarray and contractile vector variability in hypertrophic cardiomyopathy-induced pluripotent stem cell-derived cardiomyocytes. J Am Heart Assoc 3:e001263. https://doi.org/10.1161/JAHA.114.001263
- 99. Ariga R, Tunnicliffe EM, Manohar SG, et al (2019) Identification of Myocardial Disarray in Patients With Hypertrophic Cardiomyopathy and Ventricular Arrhythmias. J Am Coll Cardiol. https://doi.org/10.1016/j.jacc.2019.02.065
- 100. Young AA, Kramer CM, Ferrari VA, et al (1994) Three-dimensional left ventricular deformation in hypertrophic cardiomyopathy. Circulation. https://doi.org/10.1161/01.CIR.90.2.854
- 101. Yang H, Carasso S, Woo A, et al (2010) Hypertrophy Pattern and Regional Myocardial Mechanics Are Related in Septal and Apical Hypertrophic Cardiomyopathy. J Am Soc Echocardiogr 23:1081–1089. https://doi.org/https://doi.org/10.1016/j.echo.2010.06.006

- 102. Urbano-Moral JA, Rowin EJ, Maron MS, et al (2014) Investigation of Global and Regional Myocardial Mechanics With 3-Dimensional Speckle Tracking Echocardiography and Relations to Hypertrophy and Fibrosis in Hypertrophic Cardiomyopathy. Circ Cardiovasc Imaging 7:11–19. https://doi.org/10.1161/CIRCIMAGING.113.000842
- 103. Smiseth OA, Torp H, Opdahl A, et al (2016) Myocardial strain imaging: How useful is it in clinical decision making? Eur. Heart J.
- 104. Ersbøll M, Valeur N, Mogensen UM, et al (2013) Prediction of all-cause mortality and heart failure admissions from global left ventricular longitudinal strain in patients with acute myocardial infarction and preserved left ventricular ejection fraction. J Am Coll Cardiol 61:2365–2373. https://doi.org/10.1016/j.jacc.2013.02.061
- 105. Stanton T, Leano R, Marwick TH (2009) Prediction of all-cause mortality from global longitudinal speckle strain: comparison with ejection fraction and wall motion scoring. Circ Cardiovasc Imaging 2:356–364. https://doi.org/10.1161/CIRCIMAGING.109.862334
- 106. Mignot A, Donal E, Zaroui A, et al (2010) Global longitudinal strain as a major predictor of cardiac events in patients with depressed left ventricular function: a multicenter study. J Am Soc Echocardiogr Off Publ Am Soc Echocardiogr 23:1019–1024. https://doi.org/10.1016/j.echo.2010.07.019
- 107. Liu H, Pozios I, Haileselassie B, et al (2017) Role of Global Longitudinal Strain in Predicting Outcomes in Hypertrophic Cardiomyopathy. Am J Cardiol 120:670–675. https://doi.org/10.1016/j.amjcard.2017.05.039
- 108. G. KH, Andrea S, J. MB (1995) Phenotypic spectrum and patterns of left ventricular hypertrophy in hypertrophic cardiomyopathy: Morphologic observations and significance as assessed by two-dimensional echocardiography in 600 patients. J Am Coll Cardiol 26:1699–1708. https://doi.org/10.1016/0735-1097(95)00390-8
- 109. Williams LK, Frenneaux MP, Steeds RP (2009) Echocardiography in hypertrophic cardiomyopathy diagnosis, prognosis, and role in management. Eur J Echocardiogr 10:iii9—iii14. https://doi.org/10.1093/ejechocard/jep157
- 110. Maron BJ, Edwards JE, Moller JH, Epstein SE (1979) Prevalence and characteristics of disproportionate ventricular septal thickening in infants with congenital heart disease. Circulation. https://doi.org/10.1161/01.CIR.59.1.126
- 111. Parato VM, Antoncecchi V, Sozzi F, et al (2016) Echocardiographic diagnosis of the different phenotypes of hypertrophic cardiomyopathy. Cardiovasc Ultrasound 14:30. https://doi.org/10.1186/s12947-016-0072-5
- 112. Sivalokanathan S (2022) The Role of Cardiovascular Magnetic Resonance Imaging in the Evaluation of Hypertrophic Cardiomyopathy. Diagnostics 12:. https://doi.org/10.3390/diagnostics12020314
- 113. Green JJ, Berger JS, Kramer CM, Salerno M (2012) Prognostic value of late gadolinium

- enhancement in clinical outcomes for hypertrophic cardiomyopathy. JACC Cardiovasc Imaging 5:370–377. https://doi.org/10.1016/j.jcmg.2011.11.021
- 114. Freitas P, Ferreira AM, Arteaga-Fernández E, et al (2019) The amount of late gadolinium enhancement outperforms current guideline-recommended criteria in the identification of patients with hypertrophic cardiomyopathy at risk of sudden cardiac death. J Cardiovasc Magn Reson Off J Soc Cardiovasc Magn Reson 21:50. https://doi.org/10.1186/s12968-019-0561-4
- 115. Andre R, Hassan A-A, Steffen B, et al (2009) Noninvasive Detection of Fibrosis Applying Contrast-Enhanced Cardiac Magnetic Resonance in Different Forms of Left Ventricular Hypertrophy. J Am Coll Cardiol 53:284–291. https://doi.org/10.1016/j.jacc.2008.08.064
- 116. Yang K, Song Y-Y, Chen X-Y, et al (2020) Apical hypertrophic cardiomyopathy with left ventricular apical aneurysm: prevalence, cardiac magnetic resonance characteristics, and prognosis. Eur Hear J Cardiovasc Imaging 21:1341–1350. https://doi.org/10.1093/ehjci/jeaa246
- 117. El-Rewaidy H, Neisius U, Nakamori S, et al (2020) Characterization of interstitial diffuse fibrosis patterns using texture analysis of myocardial native T1 mapping. PLoS One 15:e0233694. https://doi.org/10.1371/journal.pone.0233694
- 118. Vernooy K, Verbeek XAAM, Peschar M, et al (2005) Left bundle branch block induces ventricular remodelling and functional septal hypoperfusion. Eur Heart J. https://doi.org/10.1093/eurheartj/ehi008
- 119. Kroon W, Delhaas T, Arts T, Bovendeerd P (2009) Computational modeling of volumetric soft tissue growth: Application to the cardiac left ventricle. Biomech Model Mechanobiol. https://doi.org/10.1007/s10237-008-0136-z
- 120. Klepach D, Lee LC, Wenk JF, et al (2012) Growth and remodeling of the left ventricle: A case study of myocardial infarction and surgical ventricular restoration. Mech Res Commun. https://doi.org/10.1016/j.mechrescom.2012.03.005
- 121. Kerckhoffs RCP, Omens JH, McCulloch AD (2012) Mechanical discoordination increases continuously after the onset of left bundle branch block despite constant electrical dyssynchrony in a computational model of cardiac electromechanics and growth. Eur Eur pacing, arrhythmias, Card Electrophysiol J Work groups Card pacing, arrhythmias, Card Cell Electrophysiol Eur Soc Cardiol 14 Suppl 5:v65–v72. https://doi.org/10.1093/europace/eus274
- 122. Yang H, Schmidt LP, Wang Z, et al (2016) Dynamic Myofibrillar Remodeling in Live Cardiomyocytes under Static Stretch. Sci Rep 6:20674. https://doi.org/10.1038/srep20674
- 123. Lee LC, Genet M, Acevedo-Bolton G, et al (2015) A computational model that predicts reverse growth in response to mechanical unloading. Biomech Model Mechanobiol. https://doi.org/10.1007/s10237-014-0598-0

- 124. Spragg DD, Akar FG, Helm RH, et al (2005) Abnormal conduction and repolarization in late-activated myocardium of dyssynchronously contracting hearts. Cardiovasc Res. https://doi.org/10.1016/j.cardiores.2005.03.008
- 125. Ypenburg C, Lancellotti P, Tops LF, et al (2007) Acute Effects of Initiation and Withdrawal of Cardiac Resynchronization Therapy on Papillary Muscle Dyssynchrony and Mitral Regurgitation. J Am Coll Cardiol. https://doi.org/10.1016/j.jacc.2007.08.019
- 126. FitzHugh R (1961) Impulses and Physiological States in Theoretical Models of Nerve Membrane. Biophys J. https://doi.org/10.1016/S0006-3495(61)86902-6
- 127. Nagumo J, Arimoto S, Yoshizawa S (1962) An Active Pulse Transmission Line Simulating Nerve Axon*. Proc IRE. https://doi.org/10.1109/JRPROC.1962.288235
- 128. Arumugam J, Mojumder J, Kassab G, Lee LC (2019) Model of Anisotropic Reverse Cardiac Growth in Mechanical Dyssynchrony. Sci Rep 9:. https://doi.org/10.1038/s41598-019-48670-8
- 129. Van Oosterhout MFM, Prinzen FW, Arts T, et al (1998) Asynchronous electrical activation induces asymmetrical hypertrophy of the left ventricular wall. Circulation. https://doi.org/10.1161/01.CIR.98.6.588
- 130. Holzapfel GA, Ogden RW (2009) Constitutive modelling of passive myocardium: a structurally based framework for material characterization. Philos Trans R Soc A Math Phys Eng Sci 367:3445–3475. https://doi.org/10.1098/rsta.2009.0091
- 131. Shavik SM, Jiang Z, Baek S, Lee LC (2018) High spatial resolution multi-organ finite element modeling of ventricular-arterial coupling. Front Physiol. https://doi.org/10.3389/fphys.2018.00119
- 132. McVeigh ER, Prinzen FW, Wyman BT, et al (1998) Imaging asynchronous mechanical activation of the paced heart with tagged MRI. Magn Reson Med 39:507–513. https://doi.org/10.1002/mrm.1910390402
- 133. Prinzen FW, Hunter WC, Wyman BT, McVeigh ER (1999) Mapping of regional myocardial strain and work during ventricular pacing: experimental study using magnetic resonance imaging tagging. J Am Coll Cardiol 33:1735–1742. https://doi.org/10.1016/s0735-1097(99)00068-6
- 134. Finsberg H, Xi C, Tan J Le, et al (2018) Efficient estimation of personalized biventricular mechanical function employing gradient-based optimization. Int j numer method biomed eng. https://doi.org/10.1002/cnm.2982
- 135. Streeter DD, Spotnitz HM, Patel DP, et al (1969) Fiber orientation in the canine left ventricle during diastole and systole. Circ Res. https://doi.org/10.1161/01.RES.24.3.339
- 136. Bayer JD, Blake RC, Plank G, Trayanova NA (2012) A novel rule-based algorithm for assigning myocardial fiber orientation to computational heart models. Ann Biomed Eng.

- https://doi.org/10.1007/s10439-012-0593-5
- 137. Westerhof N, Lankhaar JW, Westerhof BE (2009) The arterial windkessel. Med. Biol. Eng. Comput.
- 138. Guccione JM, McCulloch AD (1993) Mechanics of actiwe contraction in cardiac muscle: Part I—constitutive relations for fiber stress that describe deactivation. J Biomech Eng. https://doi.org/10.1115/1.2895473
- 139. Guccione JM, Waldman LK, McCulloch AD (1993) Mechanics of actiwe contraction in cardiac muscle: Part II—cylindrical models of the systolic left ventricle. J Biomech Eng. https://doi.org/10.1115/1.2895474
- 140. (2015) The FEniCS Project Version 1.5. Arch Numer Softw. https://doi.org/10.11588/ans.2015.100.20553
- 141. Crozatier B, Caillet D, Bical O (1984) Left ventricular adaptation to sustained pressure overload in the conscious dog. Circ Res. https://doi.org/10.1161/01.RES.54.1.21
- 142. Gyöngyösi M, Pavo N, Lukovic D, et al (2017) Porcine model of progressive cardiac hypertrophy and fibrosis with secondary postcapillary pulmonary hypertension. J Transl Med. https://doi.org/10.1186/s12967-017-1299-0
- 143. Sorensen M, Hasenkam JM, Jensen H, Sloth E (2011) Subcoronary versus supracoronary aortic stenosis. An experimental evaluation. J Cardiothorac Surg. https://doi.org/10.1186/1749-8090-6-100
- 144. Aoyagi T, Fujii AM, Flanagan MF, et al (1993) Transition from compensated hypertrophy to intrinsic myocardial dysfunction during development of left ventricular pressure-overload hypertrophy in conscious sheep: Systolic dysfunction precedes diastolic dysfunction. Circulation. https://doi.org/10.1161/01.CIR.88.5.2415
- 145. Merino D, Gil A, Gómez J, et al (2018) Experimental modelling of cardiac pressure overload hypertrophy: Modified technique for precise, reproducible, safe and easy aortic arch banding-debanding in mice. Sci Rep. https://doi.org/10.1038/s41598-018-21548-x
- 146. Ishikawa K, Aguero J, Oh JG, et al (2015) Increased stiffness is the major early abnormality in a pig model of severe aortic stenosis and predisposes to congestive heart failure in the absence of systolic dysfunction. J Am Heart Assoc. https://doi.org/10.1161/JAHA.115.001925
- 147. Charles CJ, Lee P, Li RR, et al (2020) A porcine model of heart failure with preserved ejection fraction: magnetic resonance imaging and metabolic energetics. ESC Hear Fail. https://doi.org/10.1002/ehf2.12536
- 148. Cerqueira MD, Weissman NJ, Dilsizian V, et al (2002) Standardized myocardial segmentation and nomenclature for tomographic imaging of the heart. J Cardiovasc Magn Reson. https://doi.org/10.1081/JCMR-120003946

- 149. Carasso S, Cohen O, Mutlak D, et al (2009) Differential effects of afterload on left ventricular long- and short-axis function: Insights from a clinical model of patients with aortic valve stenosis undergoing aortic valve replacement. Am Heart J. https://doi.org/10.1016/j.ahj.2009.07.008
- 150. Leonardi B, Margossian R, Sanders SP, et al (2014) Ventricular mechanics in patients with aortic valve disease: Longitudinal, radial, and circumferential components. Cardiol Young. https://doi.org/10.1017/S1047951112002326
- 151. Ozkan A, Kapadia S, Tuzcu M, Marwick TH (2011) Assessment of left ventricular function in aortic stenosis. Nat. Rev. Cardiol.
- 152. Usyk TP, Omens JH, McCulloch AD (2001) Regional septal dysfunction in a three-dimensional computational model of focal myofiber disarray. Am J Physiol Hear Circ Physiol. https://doi.org/10.1152/ajpheart.2001.281.2.h506
- 153. Deng L, Zuo H, Li A, et al (2021) Numerical Simulation Study on the Mechanism of Formation of Apical Aneurysm in Hypertrophic Cardiomyopathy With Midventricular Obstruction. Front Physiol 12:. https://doi.org/10.3389/fphys.2021.717717
- 154. Campbell SG, McCulloch AD (2011) Multi-scale computational models of familial hypertrophic cardiomyopathy: genotype to phenotype. J R Soc Interface 8:1550–1561. https://doi.org/10.1098/rsif.2011.0184
- 155. Tanaka M, Fujiwara H, Onodera T, et al (1986) Quantitative analysis of myocardial fibrosis in normals, hypertensive hearts, and hypertrophic cardiomyopathy. Br Heart J. https://doi.org/10.1136/hrt.55.6.575
- 156. Gasser TC, Ogden RW, Holzapfel GA (2006) Hyperelastic modelling of arterial layers with distributed collagen fibre orientations. J. R. Soc. Interface
- 157. Guccione JM, McCulloch AD, Waldman LK (1991) Passive material properties of intact ventricular myocardium determined from a cylindrical model. J Biomech Eng. https://doi.org/10.1115/1.2894084
- 158. Guccione JM, McCulloch AD (1993) Mechanics of actiwe contraction in cardiac muscle: Part I—constitutive relations for fiber stress that describe deactivation. J Biomech Eng. https://doi.org/10.1115/1.2895473
- 159. Lee LC, Genet M, Dang AB, et al (2014) Applications of computational modeling in cardiac surgery. J. Card. Surg.
- 160. Pezzuto S, Ambrosi D (2014) Active contraction of the cardiac ventricle and distortion of the microstructural architecture. Int j numer method biomed eng. https://doi.org/10.1002/cnm.2690
- 161. Pezzuto S, Ambrosi D, Quarteroni A (2014) An orthotropic active-strain model for the myocardium mechanics and its numerical approximation. Eur J Mech A/Solids.

- https://doi.org/10.1016/j.euromechsol.2014.03.006
- 162. Gorcsan J, Tanaka H (2011) Echocardiographic assessment of myocardial strain. J. Am. Coll. Cardiol.
- 163. Hoit BD (2011) Strain and strain rate echocardiography and coronary artery disease. Circ Cardiovasc Imaging. https://doi.org/10.1161/CIRCIMAGING.110.959817
- 164. Lamke GT, Allen RD, Edwards WD, et al (2003) Surgical pathology of subaortic septal myectomy associated with hypertrophic cardiomyopathy: A study of 204 cases (1996-2000). Cardiovasc Pathol. https://doi.org/10.1016/S1054-8807(03)00036-X
- 165. Geske JB, Cullen MW, Sorajja P, et al (2012) Assessment of Left Ventricular Outflow Gradient: Hypertrophic Cardiomyopathy Versus Aortic Valvular Stenosis. JACC Cardiovasc Interv 5:675–681. https://doi.org/https://doi.org/10.1016/j.jcin.2012.01.026
- 166. Nishimura RA, Seggewiss H, Schaff H V (2017) Hypertrophic Obstructive Cardiomyopathy. Circ Res 121:771–783. https://doi.org/10.1161/CIRCRESAHA.116.309348
- 167. Coppini R, Ferrantini C, Yao L, et al (2013) Late sodium current inhibition reverses electromechanical dysfunction in human hypertrophic cardiomyopathy. Circulation 127:575–584. https://doi.org/10.1161/CIRCULATIONAHA.112.134932
- 168. Kovacheva E, Gerach T, Schuler S, et al (2021) Causes of altered ventricular mechanics in hypertrophic cardiomyopathy: an in-silico study. Biomed Eng Online 20:69. https://doi.org/10.1186/s12938-021-00900-9
- 169. O'Hara RP, Binka E, Prakosa A, et al (2022) Personalized computational heart models with T1-mapped fibrotic remodeling predict sudden death risk in patients with hypertrophic cardiomyopathy. Elife 11:. https://doi.org/10.7554/eLife.73325
- 170. Fumagalli I, Vitullo P, Vergara C, et al (2022) Image-Based Computational Hemodynamics Analysis of Systolic Obstruction in Hypertrophic Cardiomyopathy. Front Physiol 12:. https://doi.org/10.3389/fphys.2021.787082
- 171. Huang X, Deng L, Zuo H, et al (2021) Comparisons of simulation results between passive and active fluid structure interaction models for left ventricle in hypertrophic obstructive cardiomyopathy. Biomed Eng Online 20:9. https://doi.org/10.1186/s12938-020-00838-4
- 172. Nishimura RA, Carabello BA (2012) Hemodynamics in the cardiac catheterization laboratory of the 21st century. Circulation 125:2138–2150. https://doi.org/10.1161/CIRCULATIONAHA.111.060319
- 173. Bayer JD, Blake RC, Plank G, Trayanova NA (2012) A novel rule-based algorithm for assigning myocardial fiber orientation to computational heart models. Ann Biomed Eng. https://doi.org/10.1007/s10439-012-0593-5

- 174. Shavik SM, Wall S, Sundnes J, et al (2021) Computational Modeling Studies of the Roles of Left Ventricular Geometry, Afterload, and Muscle Contractility on Myocardial Strains in Heart Failure with Preserved Ejection Fraction. J Cardiovasc Transl Res. https://doi.org/10.1007/s12265-021-10130-y
- 175. Shavik SM, Wall ST, Sundnes J, et al (2017) Organ-level validation of a cross-bridge cycling descriptor in a left ventricular finite element model: Effects of ventricular loading on myocardial strains. Physiol Rep. https://doi.org/10.14814/phy2.13392
- 176. Fan L, Namani R, Choy JS, et al (2021) Transmural Distribution of Coronary Perfusion and Myocardial Work Density Due to Alterations in Ventricular Loading, Geometry and Contractility. Front Physiol 12:. https://doi.org/10.3389/fphys.2021.744855
- 177. Fan L, Choy JS, Raissi F, et al (2021) Optimization of cardiac resynchronization therapy based on a cardiac electromechanics-perfusion computational model. Comput Biol Med 105050. https://doi.org/10.1016/j.compbiomed.2021.105050
- 178. Mojumder J, Choy JS, Leng S, et al (2021) Mechanical stimuli for left ventricular growth during pressure overload. Exp Mech 61:131–146. https://doi.org/10.1007/s11340-020-00643-z
- 179. Sommer G, Schriefl AJ, Andrä M, et al (2015) Biomechanical properties and microstructure of human ventricular myocardium. Acta Biomater. https://doi.org/10.1016/j.actbio.2015.06.031
- 180. Gao H, Li WG, Cai L, et al (2015) Parameter estimation in a Holzapfel–Ogden law for healthy myocardium. J Eng Math 95:231–248. https://doi.org/10.1007/s10665-014-9740-3
- 181. Bols J, Degroote J, Trachet B, et al (2013) A computational method to assess the in vivo stresses and unloaded configuration of patient-specific blood vessels. J Comput Appl Math 246:10–17. https://doi.org/https://doi.org/10.1016/j.cam.2012.10.034
- 182. Klotz S, Hay I, Dickstein ML, et al (2006) Single-beat estimation of end-diastolic pressure-volume relationship: a novel method with potential for noninvasive application. Am J Physiol Heart Circ Physiol 291:H403-12. https://doi.org/10.1152/ajpheart.01240.2005
- 183. Klotz S, Dickstein ML, Burkhoff D (2007) A computational method of prediction of the end-diastolic pressure-volume relationship by single beat. Nat Protoc 2:2152–2158. https://doi.org/10.1038/nprot.2007.270
- 184. Geske JB, Cullen MW, Sorajja P, et al (2012) Assessment of Left Ventricular Outflow Gradient: Hypertrophic Cardiomyopathy Versus Aortic Valvular Stenosis. JACC Cardiovasc Interv 5:675–681. https://doi.org/https://doi.org/10.1016/j.jcin.2012.01.026
- 185. Nishimura RA, Seggewiss H, Schaff H V (2017) Hypertrophic Obstructive Cardiomyopathy. Circ Res 121:771–783. https://doi.org/10.1161/CIRCRESAHA.116.309348

- 186. Tseng WYI, Dou J, Reese TG, Van Wedeen J (2006) Imaging myocardial fiber disarray and intramural strain hypokinesis in hypertrophic cardiomyopathy with MRI. J Magn Reson Imaging. https://doi.org/10.1002/jmri.20473
- 187. Das A, Chowdhary A, Kelly C, et al (2021) Insight Into Myocardial Microstructure of Athletes and Hypertrophic Cardiomyopathy Patients Using Diffusion Tensor Imaging. J Magn Reson Imaging 53:73–82. https://doi.org/https://doi.org/10.1002/jmri.27257
- 188. Mukherjee P, Berman JI, Chung SW, et al (2008) Diffusion tensor MR imaging and fiber tractography: theoretic underpinnings. AJNR Am J Neuroradiol 29:632–641. https://doi.org/10.3174/ajnr.A1051
- 189. Karlsen S, Dahlslett T, Grenne B, et al (2019) Global longitudinal strain is a more reproducible measure of left ventricular function than ejection fraction regardless of echocardiographic training. Cardiovasc Ultrasound 17:18. https://doi.org/10.1186/s12947-019-0168-9
- 190. King A, Thambyrajah J, Leng E, Stewart MJ (2016) Global longitudinal strain: a useful everyday measurement? Echo Res Pract 3:85–93. https://doi.org/10.1530/ERP-16-0022
- 191. Marian AJ, Zhao G, Seta Y, et al (1997) Expression of a Mutant (Arg92Gln) Human Cardiac Troponin T, Known to Cause Hypertrophic Cardiomyopathy, Impairs Adult Cardiac Myocyte Contractility. Circ Res 81:76–85. https://doi.org/10.1161/01.RES.81.1.76
- 192. Witjas-Paalberends ER, Piroddi N, Stam K, et al (2013) Mutations in MYH7 reduce the force generating capacity of sarcomeres in human familial hypertrophic cardiomyopathy. Cardiovasc Res 99:432–441. https://doi.org/10.1093/cvr/cvt119
- 193. Weiss MB, Ellis K, Sciacca RR, et al (1976) Myocardial blood flow in congestive and hypertrophic cardiomyopathy: relationship to peak wall stress and mean velocity of circumferential fiber shortening. Circulation 54:484–494. https://doi.org/10.1161/01.CIR.54.3.484
- 194. Suga H (1979) Total mechanical energy of a ventricle model and cardiac oxygen consumption. Am J Physiol 236:H498-505. https://doi.org/10.1152/ajpheart.1979.236.3.H498
- 195. Duchenne J, Turco A, Ünlü S, et al (2019) Left Ventricular Remodeling Results in Homogenization of Myocardial Work Distribution. Circ Arrhythm Electrophysiol 12:e007224. https://doi.org/10.1161/CIRCEP.118.007224
- 196. Chan J, Edwards NFA, Scalia GM, Khandheria BK (2020) Myocardial Work: A New Type of Strain Imaging? J. Am. Soc. Echocardiogr. Off. Publ. Am. Soc. Echocardiogr. 33:1209– 1211
- 197. Garcia Bras P, Aguiar Rosa S, Moura Branco L, et al (2022) Assessment of myocardial work: a promising tool in obstructive and nonobstructive hypertrophic cardiomyopathy. Eur Hear J Cardiovasc Imaging 23:. https://doi.org/10.1093/ehjci/jeab289.261

198. Batzner A, Seggewiss H, Hahn P, et al (2022) Myocardial work in hypertrophic cardiomyopathy - a new non-invasive parameter for segmental myocardial function? Eur Hear J - Cardiovasc Imaging 23:jeab289.276. https://doi.org/10.1093/ehjci/jeab289.276

APPENDIX A: MODEL PARAMETERS WITHOUT DISARRAY

The calibrated passive and active material described in Eq. (5.5) and Eq. (5.6), respectively, are enlisted in **Table A.1**.

Table A.1: Material parameters

Parameters	Unit	Control	Non-obstructive	Obstructive					
Holzapfel-Ogden model									
a	Ра	46	400	200					
ь		12	5	4					
a_f	Ра	7.51e03	37.5	15					
b_f		5.893	1.47325	22.1					
a_s	Ра	492	492	492					
b_s		3.393	3.393	3.393					
a_{fs}	Ра	70	70	70					
b_{fs}		3.929	3.929	3.929					
Guccione model									
T_{max}	kPa	620	400	99.75					
τ	ms	20	35	35					
t_{trans}	ms	385	430	420					
В		4.75	4.75	4.75					
t_0	ms	350	400	350					
l_0	μт	1.55	1.55	1.55					
Ca_0	μΜ	4.35	4.35	4.35					
Ca_{0max}	μΜ	4.35	4.35	4.35					
l_r	μт	1.85	1.85	1.85					
BCL	ms	1000	910	1180					

The model parameters prescribed in circulatory model and time varying elastance model are enlisted in **Table A.2.**

Table A.2: Circulatory and left atrium model parameters

Parameter	Unit	Control	Non-obstructive	Obstructive				
Circulatory model								
$C_{a,p}$	ml Pa	Pa 0.00208 0.00544		0.0048				
$C_{a,d}$	ml Pa	0.02145	0.0561	0.0495				
C_{ven}	ml Pa	0.196	0.378	0.014				
$V_{a,p,0}$	ml	144	144	306				
$V_{a,d,0}$	ml	160	160	160				
$V_{ven,0}$	ml	4500	3100	4525				
R_{ao}	$Pa\ ms\ ml^{-1}$	3000	3000	31500				
R_{ven}	Pa ms ml⁻¹	10	10	100				
$R_{a,p}$	$Pa\ ms\ ml^{-1}$	108000	90000	45000				
$R_{a,d}$	$Pa\ ms\ ml^{-1}$	127200	84800	159000				
$C_{a,p}$	ml Pa	0.00208	0.00544	0.0048				
Time varying elastance model								
$E_{es,la}$	Pa/ml	9	7	10				
A_{la}	Ра	0.801	0.6675	4.005				
B_{la}	ml^{-1}	0.0152	0.00475	0.021				
$V_{0,la}$	ml	10	10	10				
$T_{max,la}$	ms	120	120	150				
$ au_{la}$	ms	25	25	25				
$t_{delay,la}$	ms	140	140	140				

APPENDIX B: MODEL PARAMETERS WITH DISARRAY

The model parameters calibrated to match with clinical volume waveform and blood pressure with varying degree of disarray for 2 HCM subjects are listed below. Noted, the rest of the model parameters are same as described in **Appendix A**.

Table B.1: Model parameters with disarray

Parameter	Unit	$\kappa = 0.07$	$\kappa = 0.1$	$\kappa = 0.14$	$\kappa = 0.18$	$\kappa = 0.22$		
Obstructive HCM								
T_{max}	kPa	106.8	109.25	123.5	137.75	166.25		
$V_{ven,0}$	ml	4550	4640	4660	4660	4660		
Non-obstructive HCM								
T_{max}	kPa	420	440	500	840			